Thin Film Solar Cells on Transparent Plastic Foils

by

Ehsanollah Fathi

A thesis
presented to the University of Waterloo
in fulfillment of the
thesis requirement for the degree of
Doctoral of Philosophy
in
Electrical and Computer Engineering

Waterloo, Ontario, Canada, 2011

I hereby declare that I am the sole author of this thesis. This is a true copy of the thesis, including any required final revisions, as accepted by my examiners.

I understand that my thesis may be made electronically available to the public.

Abstract

The focus of this thesis is on the optimization and fabrication of p-i-n amorphous silicon (a-Si:H) solar cells both on glass and transparent plastic substrates. These solar cells are specifically fabricated on transparent substrates to facilitate the integration of thin film batteries with these solar cells. To comply with plastic substrates, different silicon layers are optimized at the low processing temperature of 135 °C. In the first part of the optimization process, the structural, electronic, and optical properties of boron- and phosphorous-doped, hydrogenated nanocrystalline silicon (nc-Si:H) thin films deposited by plasma-enhanced chemical vapor deposition (PECVD) at the substrate temperature of 135 °C are elaborated. Additionally, in this part, the deposition of protocrystalline silicon (pc-Si) films on glass substrates are investigated. In the device integration and fabrication part of this thesis, the optimization process is continued by fabricating single junction devices with different hydrogen dilution ratios for the cell absorber layer. The optimum device performance is achieved with an absorber layer right at the transition from amorphous to microcrystalline silicon. To further improve the performance of the fabricated solar cells, amorphous silicon carbide buffer layers are introduced between the nc-Si p-layer and the undoped pc-Si absorber layer. Single junction p-p'-i-n solar cells are fabricated and characterized both on glass and plastic substrates. Our measurements show conversion efficiencies of 7.0% and 6.07% for the cells fabricated on glass and plastic substrates, respectively.

In the last part of this research, the light trapping enhancement in amorphous silicon solar cells using Distributed Bragg Reflectors (DBRs) are experimentally demonstrated. Reflectance characteristics of DBR test structures, consisting of amorphous silicon (a-Si) / amorphous silicon nitride (SiN) film stacks are analysed and compared with those of conventional ZnO/Al back reflectors. DBR optical measurements show that the average total reflectance over the wavelength region of λ= 600-800 nm is improved by 28% for DBR back structures. Accordingly, single junction amorphous silicon solar cells with DBR and Al back reflectors are fabricated both on glass and plastic substrates. Our results show that the short-circuit current density and

consequently the conversion efficiency is enhanced by 10% for the cells fabricated on textured transparent conductive oxide substrates. In addition, these DBR back structures are designed and employed to improve the efficiency of semi-transparent solar cells. In this application, the optimized DBR structures are designed to be optically transparent for the part of the visible range and highly reflective for the red and infra-red part of the spectrum. Using these DBR structures, the efficiency of the optimum semi-transparent solar cell is enhanced by 5%.

Acknowledgements

I wish to sincerely express my gratitude to:

Professor Siva Sivoththaman for his supervision and kind support during the past year of my studies;

I would like to express my gratitude to my previous supervisor, **Professor Andrei Sazonov**, for his support, advice, and encouragement during the first three years of my studies at the University of Waterloo.

Professor Dayan Ban, **Professor Vassili Karanassios**, **Professor Nazir Kherani**, and **Professor William Wong**

for accepting to review my work;

My colleagues **Dr. Yuri Vygranenko**, **Dr. Majid Gharghi**, **Dr. Mohammadreza Esmaeili-rad**, **Bahareh Sadeghimakki**, **Mohsen Mahmoudysepehr**, **Amir Goldan**, **Michael Adachi**, and **Dr. Maryam Moradi**

for precious cooperation and useful discussions;

Joseph Street, and **Richard Barber**

for their efforts in CAPDS and G2N Labs;

Dr. Shahin Jafarabadashtiani, **Dr. Saeed Fathololoumi**, **Dr. Mehdi Torbatian**, **Dr. Javid Jaffari**, **Babak Alipanahi**, **Ghasem Razavi**, **Yaser Azizi** and **Dr. Hamidreza Alemohammad**

for the unforgettable time we spent as colleagues in Waterloo;

and finally I would like to express my deepest gratitude and appreciation to my beloved parents and my brothers for their great support and encouragement.

Dedication

To my parents for their love and endless support

Contents

List of Tables

List of Figures

Chapter 1

Introduction

Presently the rise in Carbon Dioxide levels in the atmosphere is a major environmental concern, since it is one of the key factors in Global Warming. Thus in order to keep the present atmospheric CO_2 level constant, an additional 20 TW energy must be produced per year from clean and renewable energy sources such as wind, biomass, geothermal, hydro and solar respectively. Since the Earth receives 125000 TW of solar radiation every year, investment into the research, development and production of efficient but cheap large area solar cell modules can produce a significant portion of the aforementioned energy need. Having said that, the major barriers in reaching this goal is the cost of solar cell production, feedstock availability and energy payback[1].

Most of the solar cells (93.5%) are produced from silicon wafers and the cost of these wafers accounts for more than 50% of the costs at the module level [1, 2]. Currently, PV (Photovoltaics) industry consumes 50% of the world's supply of silicon feedstock. However, the larger value per area of semiconductor industry products and the ability of this industry to pay higher prices to the feedstock manufacturers, has lead to the dependence of the PV industry on the needs of the semiconductor industry. As a result, due to the shortage of the silicon feedstock in 2006-2007, its spot price has risen more than three times from \$65/kg to >\$200/kg[3, 2].

As an effective strategy to reduce solar cell prices, inexpensive substrates such as glass sheets, metal foils and plastic films have been employed by researchers. By

using these substrates and a thin layer of silicon, it is possible to significantly reduce the fabrication costs. In the context of this research, these solar cells are referred as "Thin Film Solar Cells". However, one should bear in mind the existence of other types of thin film solar cells such as Cadmium Telluride (CdTe), Copper Indium Gallium Selenide (CIGS) and organic solar cells. Due to the major obstacles like toxicity of Cadmium, limited availability of indium and instability of organic solar cells, their market share is much smaller than that of silicon. So, these thin film solar cells will not be discussed here.

As can be seen from Figure 1.1, the market share for thin film PV continues to grow rapidly, from 6.5% in 2005 to about 25% in 2010. The wafer-based silicon disruption in the growth during 2006-2007 is due to the silicon feedstock shortage; a problem which does not seem to be solved on the short term. As depicted in Figure 1.1, wafer-based silicon is still a dominant choice for PV industry with average production capacity of 5.6 GW_p compare to 1.75 GW_p of thin film technology (2010). However, since material constraints do not exist for thin film technology, investment in thin film PV is estimated to be more advantageous in the near future [2].

Unlike rigid substrates, the thickness of the flexible substrates can be significantly lower while maintaining their integrity, leading to thin and lightweight products. At the same time, these thin substrates add new functionality to thin-film electronics, i.e. the flexing and non-planar shaping. This characteristic offers new possibilities for integrating the solar cells in buildings and roofs of houses with wavy roof tiles. Furthermore, flexible substrates are compatible with Roll-to-Roll (R2R) fabrication process which can eliminate processing steps involving extra substrate handling [4].

Having said, one faces new challenges when fabricating solar cells on thin foils. These are usually not encountered during the fabrication of these devices on thick plates of glass. In the next section, advantages and disadvantages of different flexible substrates will be investigated and according to the objective of this research, the appropriate one will be introduced.

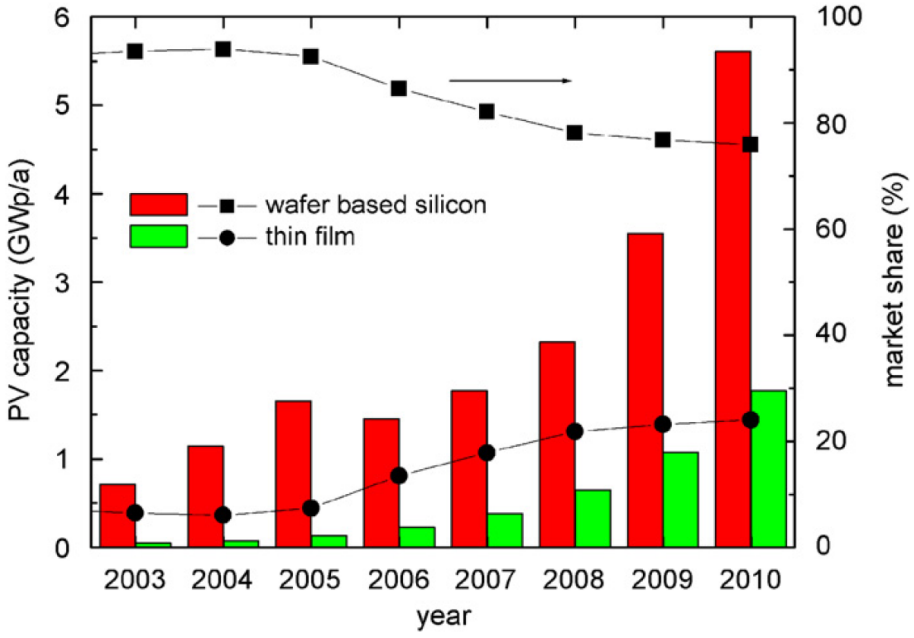

Figure 1.1: Production capacity and market share for wafer-based silicon and thin film PV technology [2].

1.1 Flexible Substrates

The ideal substrate for flexible solar cell would have to be bendable, rollable, low-cost, chemical resistant, and thermal cycling resistant. Also, it should have a very low permeability to moisture and oxygen such that it acts as a passivating layer to the fabricated device. Passivating property of these substrates enables one to simply laminate the same flexible film on the device side of the solar cell thus efficiently packaging the device at a reasonably low cost. So far, no material has emerged that demonstrates all the aforementioned properties, but the three that have come close are glass, plastic and stainless steel (SS). Table 1.1 compares different characteristics of these flexible substrates. Although the flexible glass can be a good candidate for flexible solar cell, its high fabrication cost, makes it economically unattractive to the PV industry and will not be considered here. We shall go over the advantages and disadvantages of stainless steel and plastic foils in the following subsection.

Table 1.1: Flexible substrates Comparison [5]

Property	**Stainless Steel**	**Plastics (PEN[1], PI[2])**	**Glass**
Thickness(μm)	100	100	100
Weight(g/m^2)	800	120	220
Safe Bending Radius(cm)	4	4	40
R2R Processable?	Yes	Likely*	Unlikely
Visually Transparent	No	Some	Yes
Max. Process Temp.(°C)	1000	180,300	600
TCE [3](ppm/°C)	10	16	5
Elastic Modulus(GPa)	200	5	70
Permeable O_2, H_2O	No	Yes	No
Prebake Required?	No	Yes	Maybe
Planarization Necessary?	Yes	Maybe	No
Electrical Conductivity	High	None	None
Thermal Conductivity(W/m.°C)	16	0.1-0.2	1
Deform After Device Fabrication	No	Yes	No

*Yes [6]

1.1.1 Stainless steel foils

The metal foils have superior mechanical properties and are dimensionally much more stable than plastic substrates. As a result, they are resistant to curling due to the stress in films which is an important issue with plastics. Bare stainless steel substrates have rougher surfaces than glass or plastic. These textures are formed during the metal forming process, where the rolling mill creates very rough and sharp surface profiles in the milling direction. These sharp grooves often cause device failures.

[1]polyethylene terephthalate

[2]polyimide

[3]Temperature Coefficient of Expansion

Thus, after milling they are either polished or planarized with a film. The root mean square (rms) roughness of the bare stainless steel foils is in the range of 100-500 nm. The Stainless steel foils are currently available commercially with a surface finish compatible with planarization layers at a cost comparable with plastic substrates. At present, United Solar Ovonic Corp. [7] is using R2R manufacturing technique in order to fabricate amorphous silicon solar cells on a 125 μm thick stainless steel substrate [5]. While these solar cells offer many advantages, the heavy weight of the metallic foil (in comparison with plastic substrates) and the impossibility of having monolithic series connection without an insulating layer are limiting factors for these substrate type solar cells.

1.1.2 Plastic films

While using plastic substrates offers many opportunities, it bring some particular issues too. The most important processing distinction between these substrates and the conventional glass substrates comes from their lower working temperature. Due to the low melting temperature of plastic substrates, optimization of semiconductor films are restricted to lower deposition temperates. Usually at these temperatures, the structural and electrical characteristic of silicon films are degraded compared to the ones acquired in higher temperatures ($\approx$ 300 °C). At the same time, this lower working temperature is economically beneficial as it reduces the time and energy required to manufacture the devices. Furthermore, Plastic substrates allow for a combination of both roll-to-roll production and monolithic series connection of cells in a module.

In recent years, plastic substrate solar cells have attracted great attention in both academia and industry. In addition to the conventional application of these solar cells in rollable mobile photovoltaic , plastic substrates may be adopted in fashion industry as clothing integrated photovoltaics [8] (see Figure 1.2).

Currently, several companies with different technologies are actively fabricating flexible silicon solar cells on plastics:

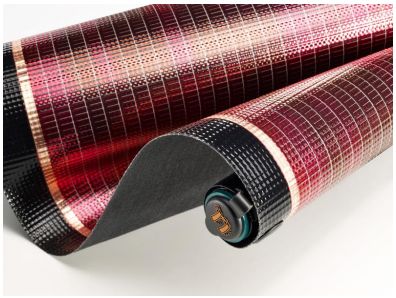

Flexcell portable modules

DIY solar-bag prototype

Winter outdoor jacket by Maier sports

Figure 1.2: Application of plastic substrate solar cells in rollable mobile photovoltaic and clothing industry.

- Fuji Electronics [9]
- United Solar Ovonic [7]
- Flexcell [10]
- Akzo Nobel [11]
- PowerFilm [12]
- Sanyo Electric [13]

Taking into account the wide application range of these solar cells, recently many academic PV groups have motivated to begin research on this topic. In many cases, the objective is to use low cost polymers such as PET and PEN as the substrate and improve the electrical efficiency and mechanical properties of the cells fabricated on these substrates. In order to acquire a deep understanding of the technology development and current issues of these solar cells, it is essential to look into the recent publications in this area.

In the following, to have a better understanding of the design and operation of an amorphous silicon solar cell, the important structural and material properties of

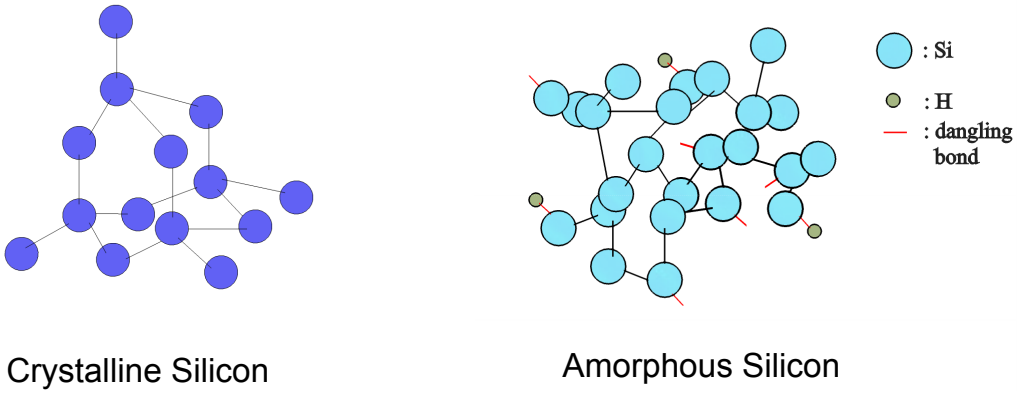

Figure 1.3: Schematic representation of the atomic structures of single crystalline and amorphous silicon.

amorphous silicon (a-Si) is described and compared to those of the single crystalline silicon (c-Si).

1.2 Material structure

1.2.1 Amorphous silicon

Crystalline silicon structure consists of fourfold coordinated silicon atoms. In this structure all bonds have the same length, and angles between each other. As it is illustrated in Figure 1.3, the symmetrical atomic arrangement in a crystalline silicon structure is lead to a so-called long-range order. In amorphous silicon lattice this structural order is not present over a long range. Deviation of the coordination number, bond lengths, and bond angles in amorphous material is lead to a locally disordered structure or a continuous random network material. While amorphous silicon lacks the long-range order, there is a similarity in atomic configuration on a local atomic scale. As a result, this material often considered as a material with the short-range order structure. The fluctuations in bonding lengths and angles between the neighboring atoms in amorphous silicon result in weak bonds where a small thermal

energy can easily break them. This process leads to the formation of a coordination defect in the atomic network. In fact, this definition of defect for amorphous silicon is different than that of crystalline lattices. In a crystalline structure any atoms that are not correctly positioned in the crystal lattice (vacancies, interstitials, and dislocations) is considered as a defect. For amorphous silicon, this definition is modified as the atoms have partially lost their order and do not have a precise location. Coordination defects in amorphous silicon are mainly silicon atoms with threefold coordinated bonds where they are covalently bonded to only three neighboring atoms. This configuration results in unpaired electrons or so-called dangling bonds.

The concentration of these dangling bonds in a pure amorphous silicon (without any atomic hydrogen) is in the order of 10^{21} cm^{-3} which make it impractical for any device fabrications. However, when amorphous silicon deposited from decomposition of Silane (SiH_4) and Hydrogen (H_2) gases, the atomic hydrogen can be incorporated in the amorphous network where they bond with most of dangling bonds. In this case, Si-H bonds are formed by which passivating the dangling bonds in amorphous silicon material. In this process, the concentration of dangling bonds are reduced to about 10^{16} cm^{-3} in the alloy of silicon and hydrogen which is usually called hydrogenated amorphous silicon (a-Si:H).

Another important difference between amorphous and single crystalline silicon is the density of states. In single crystalline silicon, due to the long-range order of the atomic structure, a well defined bandgap, E_g is defined as the energy difference between the maximum and minimum of the valence band and conduction band, respectively. In a-Si:H, bonding disorder in the material results in the spread of the valence band and conduction band states into the bandgap and form regions of localized states that are called band tails. These localized states are asymmetrical with larger band tails near the valence band edge as it shown in Figure 1.4. In addition to these band tails, coordination defects create some deep energy states between the valence band and conduction band edges. Due to the localized nature of these states, the carrier mobility in these energy regions is much smaller that that of the extended

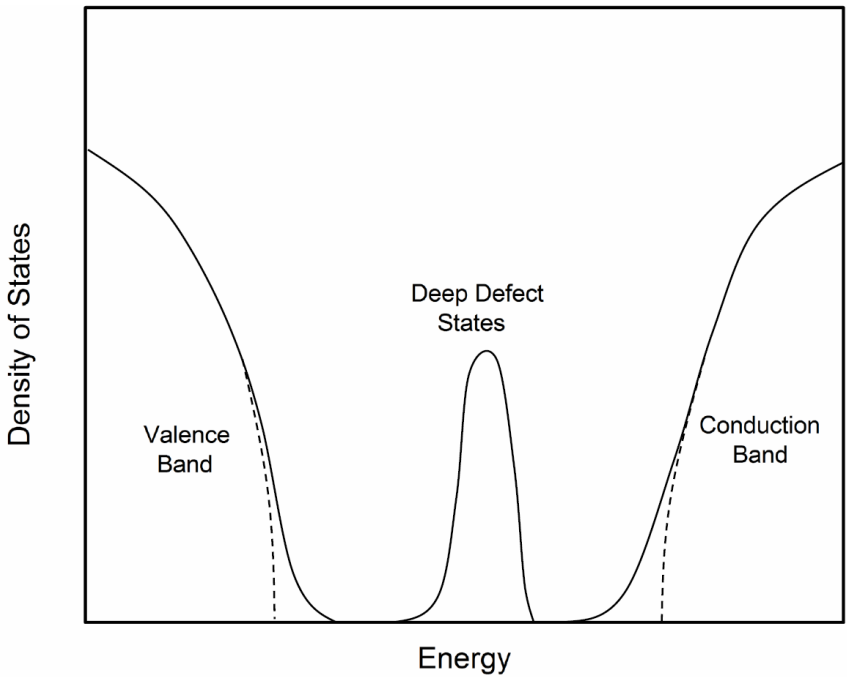

Figure 1.4: Density of states distribution of amorphous silicon material.

states beyond the valence and conduction band edges. Consequently, the threshold energy levels which characterize this mobility difference is used to define the mobility gap, E_{mob} with a typical value of 1.7 in a-Si:H.

An additional important difference between amorphous and single crystalline silicon is the limitation in the doping process. The presence of localized energy states in the bandgap restricts the amount of doping by causing the space charge build-up in these states which in turn compensates the charge of ionized doping atoms. This process results in a lower value of the open circuit voltage than what we theoretically expect from the energy band gap of amorphous silicon.

Metastability of amorphous silicon when it is exposed to the light is known as the Staebler-Wronski effect. In this process, the structural and optoelectronic properties of a-Si:H are changed as a result of higher light-induced recombination and consequently the defect density (through breaking weak Si-Si bonds). This process is reversible and can be removed by annealing the sample at higher temperatures ($\sim$ 150 °C) as it partially happens for a-Si solar cells during the summer.

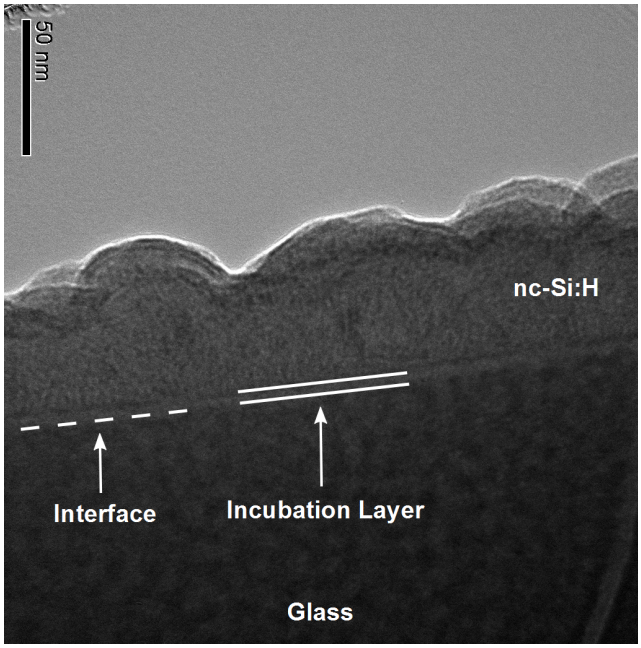

Figure 1.5: TEM photograph of 50 nm thin nc-Si layer grown on a glass substrate.

1.2.2 Microcrystalline silicon

Hydrogenated microcrystalline silicon (μc-Si:H) is a complex material similar to amorphous silicon (a-Si). The main difference between this material and a-Si:H is conglomerates nanocrystals embedded into the amorphous silicon. This conglomerates consist of nanocrystals with diameters between 10 to 20 nm. In general μc-Si:H is obtained by increasing the hydrogen content of a standard a-Si:H film deposition. This material is sometimes refer to as nanocrystalline or protocrystalline silicon (nc-Si:H / pc-Si:H). Further details on this material and its application in solar cells will be presented in the next chapter. Figure 1.5 shows a Transmission Electron Microscopy (TEM) cross section of the nc-Si:H film deposited on a glass substrate. From this figure, we can observe a thin layer of amorphous silicon exactly on top of the substrate. Further magnification of the interface at Figure 1.6 shows the amorphous structure of the incubation layer and the nanocrystalline silicon grains. The circle defines a nanocrystal which is embedded in an amorphous tissue.

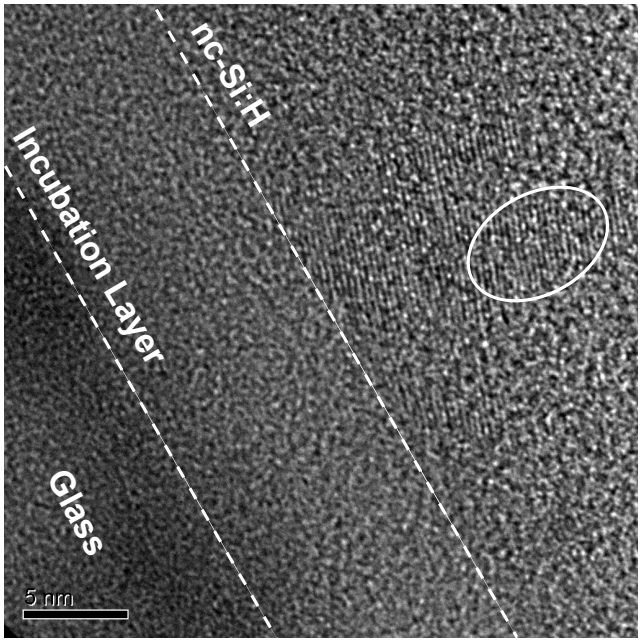

Figure 1.6: TEM photograph of the incubation layer and noncrystalline grains.

1.3 Thin film silicon solar cell structure

In principle, the solar cell consists of a junction formed between n-type and p-type semiconductors. In a-Si:H, doping the amorphous material creates a high density of defects, deteriorating the diffusion length of minority carriers. So, in an amorphous silicon p-n junction, due to the very short diffusion length of photogenerated carriers, they would all recombine in the doped layers before reaching the depletion region of the junction. Addition of an intrinsic layer between p- and n-doped layers can solve this problem. In a p-i-n (n-i-p) configuration, the intrinsic layer acts as an absorber medium and thin doped layers set up an internal electric field across this absorbing layer. As it is shown in Figure 1.7, the electron-hole pairs generated in the absorber layer encounter the internal electric field, which facilitates the separation of electrons and holes. The photogenerated carriers move towards the doped layers and are collected by the electrodes. In order to enhance the collection of holes, which are collected at the p-layer, and whose mobility is smaller than that of electrons, illumination is commonly performed through the p-doped layer [1].

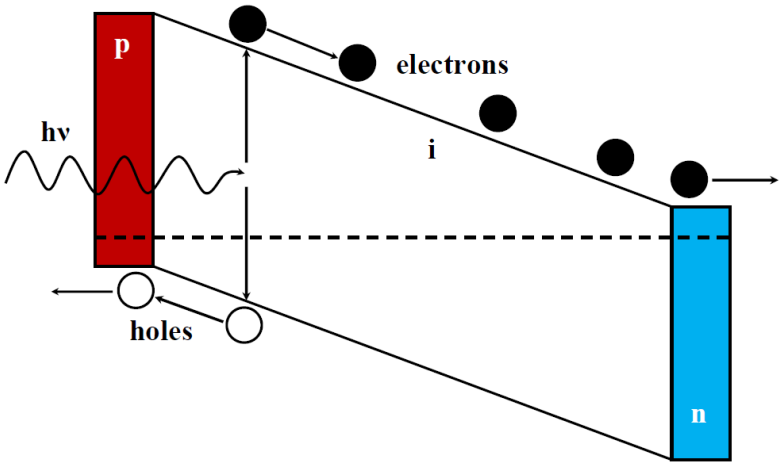

Figure 1.7: Schematic representation of a p-i-n device under illumination in short-circuit conditions.

Based on the sequence of doped and undoped silicon layer depostions, two different structures are possible in silicon thin film solar cells: superstrate structure (Figure 1.8, where a p-i-n cell is deposited onto a transparent conductive oxide (TCO), and substrate structure (Figure 1.9) in which an n-i-p sequence is grown on an opaque substrate. In superstrate configurations, both the substrate and front contact should be transparent whereas, in the n-i-p configuration substrate sits at the back side of the solar cell allowing the possibility of using the stainless steel and opaque plastic foils.

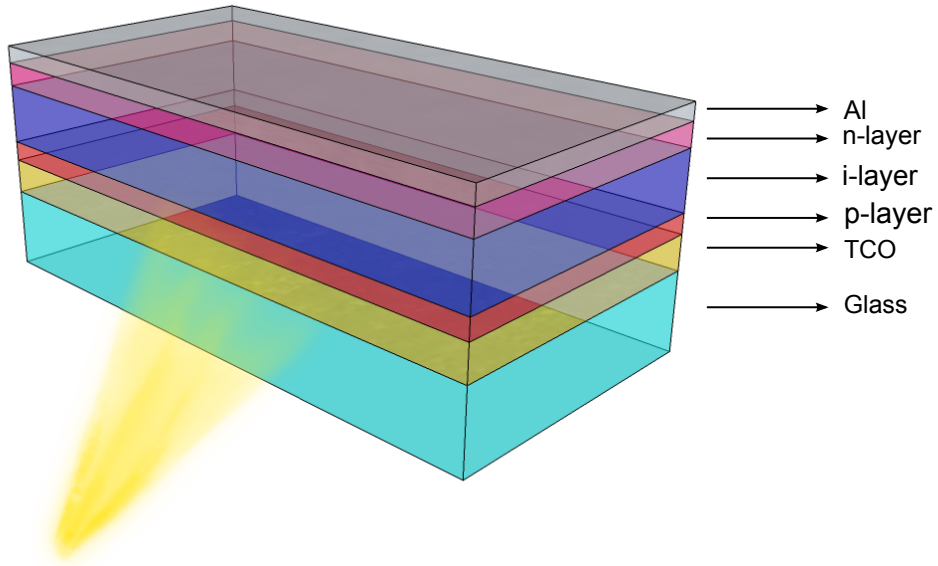

Figure 1.8: Schematic representation of the structure of a p-i-n solar cell.

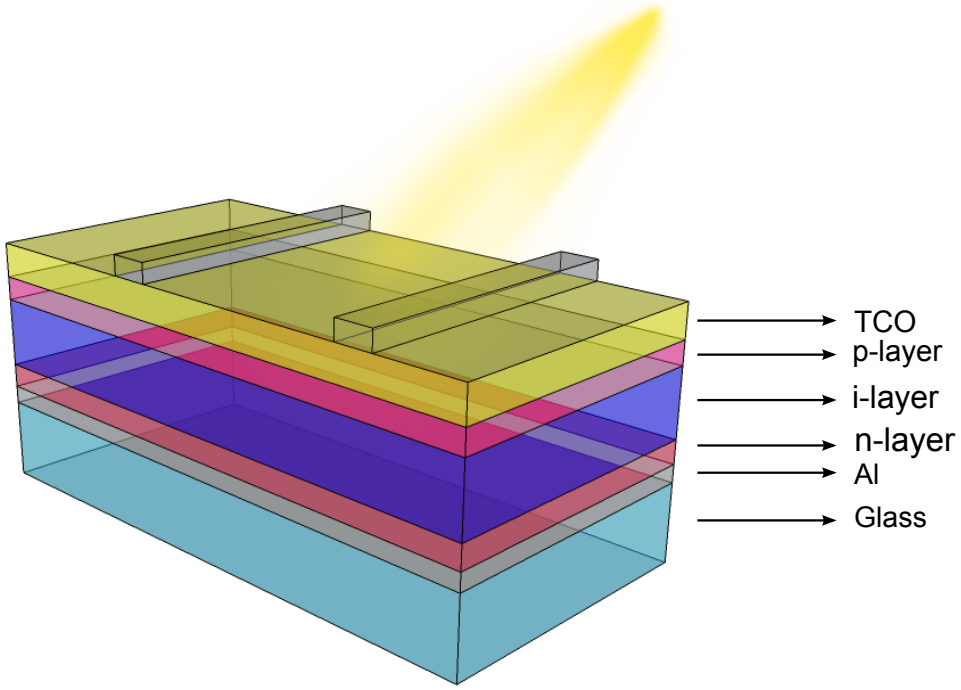

Figure 1.9: Schematic representation of the structure of an n-i-p solar cell.

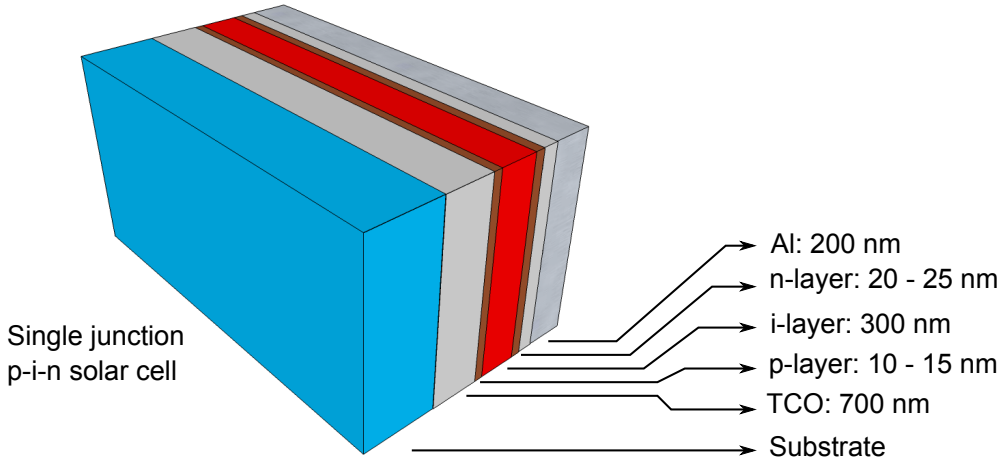

Figure 1.10: A single junction p-i-n a-Si solar cell structure.

Schematic structure of a typical p-i-n a-Si:H solar cell is shown in Figure 1.10. This single junction solar cell consists of a ∼700-900 nm thick TCO layer, ∼10-15 nm p-type layer, ∼300 nm thick undoped a-Si:H layer, ∼20-25 nm thick n-doped layer, and ∼200 nm thick Al contact. Doping levels of the n- an p-doped layers should be high enough to ensure both high electric fields and low ohmic contacts in the device. While these two characteristics can be achieved by increasing the thickness of doped layers, high defect density of these layers has a determinable effect on the incoming light. Photon absorption in doped layers leads to the photo-generated carriers which can not be collected. As a result, people try to minimize the thickness of these layers and make them as transparent as possible to the incoming photons. Here, replacing p-doped a-Si:H with hydrogenated silicon carbide (a-SiC:H), having a wide optical bandgap (∼2 eV) can significantly minimizes the absorption of photons in the device window layer. Using this wide bandgap p-layer creates a heterojunction p-i interface with band offsets between the energy bands of p-doped and intrinsic layers. In a-Si:H solar cells, this interface is of the greatest importance due to the high generation of carriers in this region. Introducing a lightly doped wide bandgap a-Si:H or a-SiC:H known as buffer layers at this interface, can effectively optimize the electric field profile and prevent back diffusion of the electrons into the p-doped layer. The intrinsic layer

serves as an absorber. The thickness and quality of this layer is crucial in acquiring high efficiencies in an a-Si solar cell. The collection of generated carriers in a single junction cell strongly depends on the magnitude of the internal electric field, and the mobility and lifetime of these carriers. In thiner intrinsic layers, photogenerated carriers experience higher electric fields and consequently better collections at the electrodes. In the other hand, by decreasing the thickness of this layer the absorption is decreased. So, the thickness of the absorber layer is a delicate design parameter in a-Si:H solar cells. According to simulation and experimental results, the optimum thickness for this layer is in the range of 250-320 nm [1].

1.4 Light Management

In amorphous silicon solar cells, the absorption length of photons in the wavelength range of 600-800 nm reaches values above $1\mu m$. However, to minimize the process time and reduce the light-induced degradation, the absorber layer thickness should be as low as possible. As a result, in a thin film of not more than a few microns, incoming long wavelength photons will not be completely absorbed in a single pass. Therefore, light trapping schemes are necessary to enhance absorption of the long wavelength photons. There are different techniques which are implemented to capture light in the absorbing layer. These techniques are typically based on the light scattering at the rough interfaces and on the employment of highly reflective back contacts [1]. In a superstrate configuration where a p-i-n structure is deposited onto a transparent conductive oxide, it is the roughness of the TCO layer (typically with root mean-square surface roughness of 50-150 nm) and/or texturing the back contact that scatters the incoming light at different angles. Furthermore, TCO layer with a rough surface at the front contact acts as an efficient antireflection coating due to the gradual change of the refractive index at the TCO/Si interface [14]. The back contact is usually a metallic layer, deposited onto a TCO interlayer. Using TCO interlayer improves the reflection from the back contact by matching the refractive indices between the n-type silicon and metal layer. Figure 1.11 shows a schematic

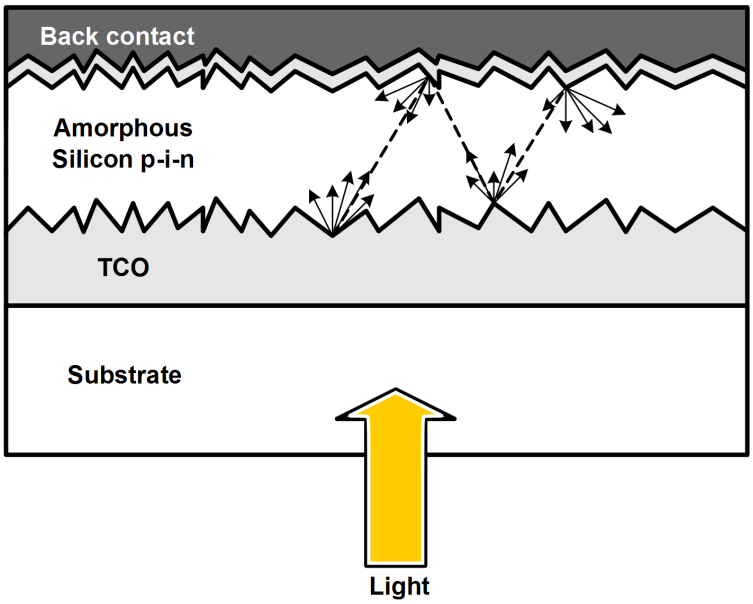

Figure 1.11: Schematic of an amorphous silicon solar cell with p-i-n configuration. The concept of light trapping is illustrated in this figure.

cross section of a silicon thin film p-i-n solar cell with rough interfaces. The concept of light trapping is illustrated by the arrows representing incoming and scattered light. The back metallic contact in a thin film amorphous silicon solar cell is either silver (Ag) or aluminum (Al) where aluminum is preferred in industry due to its lower price and better adhesion properties.

1.5 Technology overview

Fabrication of thin film solar cells on plastic substrates started in the early 1980s [15]. Table 1.2 provides an overview of the main structures and characteristics of different solar cells which improved the state-of-the-art at the time of fabrication. In the following, a summary of fabrication issues and research achievements of each paper is presented.

Researchers at Teijin Ltd., Japan were the first to report the fabrication of n-i-p a-Si:H solar cells on PI (Kapton®) substrates[15]. They achieved a low short-circuit

current density due to the surface defects of PI films. To solve this problem, M. Yano et al. [16] suggested using PET instead of PI films, as the PET substrates had a much more smoother surface than PI films. Finally, they succeeded in fabrication of a 20×60 cm^2 module with a practical efficiency of 5.5%.

Until 2002, researchers have employed amorphous silicon as the active layer in their solar cells. Generally, due to the light-induced degradation effects, the efficiency of amorphous silicon solar cells are low (5 to 7%). Microcrystalline silicon has a much milder form of light induced degradation. Moreover, due to the lower bandgap of this material compared to the amorphous silicon, it has a high capacity for absorption in the near infrared region. Mase et al. [17] employed this new material to fabricate a single junction n-i-p solar cell on Ethylene-Tetracyclododecene (E/TD) copolymer and they achieved a high efficiency of 6%. The lower absorption coefficients of microcrystalline silicon necessitates using thick absorbing layers in the order of 1μm or more. Due to the limited deposition rate of microcrystalline silicon, the intrinsic layer thickness and the deposition time are critical parameters for industry[1]. By using proper light management techniques such as substrate texturing, one can increase the effective optical path within the solar cell. Using this method, T. Takeda et al. [18] obtained an efficiency of 8.1% and a high short-circuit current of 25.8 mA/cm^2 in a single junction n-i-p structure. Later, in 2005 researchers at the University of Neuchatel in cooperation with OVD-Kinegram A.G.[4] used periodically textured silver and aluminum back-reflectors and obtained a high performance microcrystalline silicon solar cell on a PET substrate.

[4]A company, supplying advanced optically variable plastic films to protect banknotes and government documents

Table 1.2: Structure and properties of different thin film solar cells on plastic substrates

Structure	Temp. (°C)	i-layer	J_{sc} (mA/cm^2)	FF (%)	V_{oc} (mV)	Efficiency (%)	Size (cm^2)	Year	Reference
PI / SS / p-i-n / ITO	300	a-Si	10.42	62.87	898	6.36	0.09	1982	[15]
PET / Al / SS / p-i-n / ITO	N/A	a-Si	15.3	67.2	880	9	1.2	1986	[16]
PI(transparent) / ITO / p-i-n / Al	180	a-Si	8.5	62.5	823	4.3	7.4	1991	[19]
PI / Ag / ZnO / n-i-p / ITO	240	a-Si	15.1	64	906	8.7	0.25	1997	[20]
PET / Ag / ZnO / n-i-p / ITO	150	a-Si	11	51.8	889	5.0	0.25	2000	[21]
PEN / Ag / ZnO / n-i-p / ITO	150	a-Si	11	55.2	896	5.4	0.25	2000	[21]
E/TD / Ag / ZnO / n-i-p / ITO	100	μc-Si	20	N/A	430	6.0	0.05	2002	[17]
LCP / Ag / ZnO / n-i-p / ITO	180	μc-Si	22	68	462	7.2	N/A	2003	[18]
PET / Al / ZnO / n-i-p / ITO	N/A	a-Si	12.5	69.6	877	7.62	N/A	2005	[6]
PET / Ag / ZnO / n-i-p / ZnO	N/A	μc-Si	17.9	72.1	501	6.46	N/A	2005	[6]
PET / Al / ZnO / n-i-p / ZnO	N/A	a-Si/μc-Si	9.4/12.1	68.0	1330	8.3	N/A	2005	[6]
PI /Al / ZnO / n-i-p (triple) / ITO	N/A	a-Si/ a-SiGe	7.06	N/A	2097	9.86	0.25	2006	[22]
PET / ZnO / p-i-n / PET / Al	110	pc-Si	8.8	61.1	908	4.9	0.09	2006	[23]
PC / SiO_x / Al / n-i-p / ZnO	160	μc-Si	13.46	44.9	381	2.3	1.0	2006	[24]
PC / SiOx / ZnO / p-i-n / Ag	160	a-Si	10.26	56	852	4.9	1.0	2006	[24]

According to the Bailat et al. [6], by using nano-textured PET substrates, they fabricated amorphous and microcrystalline n-i-p solar cells with stable efficiencies of 7.62% and 6.46%, respectively. Moreover, using these textured substrates, amorphous/microcrystalline tandem solar cells were fabricated by the same research group. The authors managed to increase the efficiency of these solar cells from 8.3% to 9% by further optimizing the absorber layer. Currently, Flexcell (VHF-Technology) [10] is producing these solar cells with a wide range of power ratings. Recently, A. Vijh et al. [22] have extended the idea of tandem solar cells on plastics and fabricated a triple junction a-Si/a-SiGe/a-SiGe solar cell on PI films and achieved a high efficiency of 9.86%. While triple junction a-Si/a-SiGe/a-SiGe offers high performance characteristics, two main issues are encountered with a-SiGe: difficulty in making device grade a-SiGe intrinsic layer and the relatively high cost of germane (GeH_2) source gas. These obstacles have opened up new opportunities for microcrystalline silicon as an alternative layer for multijunction solar cells [1].

Referring to the table 1.2, the substrate thermal specifications determine the maximum processing temperature. In some applications with substrate thicknesses in the range of 10-50 nm, due to the mechanical issues, we need to further reduce the processing temperature. For example, in clothing integrated photovoltaics, the processing temperature should be as low as 100-130 °C to retain mechanical stability of the substrate [8]. At these temperatures, protocrystalline silicon presents superior optoelectronic properties compared to amorphous or microcrystalline silicon. Protocrystalline silicon (pc-Si) refers to the material exactly at the transition of amorphous to microcrystalline phase. In this material, a few isolated silicon nanocrystalls are embedded in an amorphous network [23]. Using this material, Y. Ishikawa et al. [23] optimized a p-i-n silicon solar cell on PET substrates and attained a stable efficiency of 4.9%. Even though they were successful to present a relatively high efficiency in a low temperature of 110 °C, the solar cell's short-circuit current was quite low compared to the sate-of-the-art solar cells on plastics. In this case, by using proper light management schemes, one can generate short-circuit current densities as high as amorphous and microcrystalline silicon solar cells.

1.6 Objective of This Research

A quick review of the table 1.2 reveals that, most of the research groups have used the substrate configuration. Although the opacity of some plastics like PI does not offer any other option, the potential transparency of PET and PEN should be considered in some special applications. Recently, G. Dennler et al. [25] have proved the feasibility of polymer solar cells connected to polymer-Li batteries. On the other hand, According to M. B. Schubert and J. H. Werner [8], there is a huge market opportunity for the integrated photovoltaics. In these applications, the ability to integrate PV cells with rechargeable thin film batteries would revolutionize the portable industry. In order to make such an integrated rechargeable solar cell, one should note that the only configuration which meets both mechanical and structural requirements is a superstrate configuration. As, the batteries' lamination should be either on top of the solar cell layers or on the other side of the substrate. Taking into account the mechanical issues associated with flexible substrates, laminating the batteries to the other side of the solar cell would not be a suitable choice. As a result, one is limited to superstrate or p-i-n based configurations. The aspiration of this doctoral research originates from the necessity to optimize these kinds of flexible solar cells. Based on this request, the objectives of current research proposal are:

- Doped and undoped silicon layer optimization at the low substrate temperature of 135 °C for applications in a-Si based solar cells.
- Single junction p-i-n device optimization at the low substrate temperature of 135 °C.
- Fabrication of single junction p-i-n solar cells both on glass and transparent plastic substrates.
- Employing light management schemes to enhance the overall efficiency of the fabricated solar cells.

1.7 Structure of This Thesis

Chapter 1

This chapter intends to provide an overview of the thin film silicon photovoltaic and provide knowledge about the material and structural properties of the a-Si based solar cells. In this chapter we also present a brief overview of these devices fabricated on plastic substrates.

Chapter 2

This section addresses material properties, deposition techniques, and characterization setups which have been used in this research.

Chapter 3

For doped silicon layer optimization, as a first step we explore the influence of low substrate temperature of 135 °C on a previously optimized undoped nanocrystalline silicon layer deposited at the substrate temperature of 300 °C. This material with crystalline grains at the early stage of the film deposition is a promising base material for doped silicon films. Then, hydrogen diluted phosphine or trimethylboron (TMB) gases are added to the deposition process of this undoped nc-Si:H film in order to obtain n- or p-doped nc-Si:H, respectively. The evolution of structural and electronic properties of n- and p-doped hydrogenated silicon films is investigated by gradually varying the phosphine-to-silane and the TMB-to-silane flow ratios. Undoped amorphous silicon films are deposited by varying silane-to-hydrogen ratios while keeping other deposition parameters constant. Here, photosensitivity σ_{photo} / σ_{dark} is considered as the quality factor for the undoped silicon layers. It is important to note that at this stage all the film optimizations are carried out on the glass substrates. Employing these optimized films, single junction p-i-n solar cells are fabricated both on glass and PEN substrates.

Chapter 4

As it is explained in Chapter 2, using protocrystalline silicon as the absorber

layer in a-Si based solar cells results in superior device characteristics over pure amorphous or microcrystalline silicon counterparts. Taking into account the sensitivity of this phase transition to the nature of the substrate, the undoped layer should be optimized within the solar cell structure. At this stage, the absorber layer of solar cells are deposited by varying hydrogen dilution ratio while keeping the RF power and the layer thickness constant for all cell fabrications. For n- and p-doped hydrogenated silicon films, we have initially used our optimized process conditions acquired in the first stage. To further improve the quality of the p-i-n silicon structure, we have also investigated the effect of using different doped and undoped amorphous silicon carbide films as the device window and buffer layers, respectively. Unlike the nanocrystalline characteristic of the p-doped layers deposited on glass substrates, further measurements show that the films grown directly on ZnO:Al (with the same deposition conditions) are almost amorphous. This technological issue can be resolved by controlling the initial development of crystalline nuclei. Here, we have proposed using a seed layer to promote the crystallinity of the p-doped silicon window layer. By employing the p-doped nc-Si:H as a window layer combined with differen p-doped a-SiC ('p) and undoped a-SiC (δ) buffer layers, a-Si:H-based p-p'-δ-i-n solar cells are fabricated and characterized.

Chapter 5

We propose using Distributed Bragg Reflectors (DBRs) as the highly reflective back structures in p-i-n solar cells. In this part, reflectance characteristic of DBR test structures, consisting of amorphous silicon (a-Si) / amorphous silicon nitride (SiN) film stacks are analyzed and compared with that of conventional ZnO/Al back reflectors. Accordingly, single junction amorphous silicon solar cells with DBR and Al back reflectors are fabricated both on glass and plastic substrates. Following this idea, we have proposed using DBR structures to enhance the efficiency of semi-transparent a-Si solar cells. These solar cells have a huge market opportunity for building-integrated applications. These DBR

structures are designed to be semi-transparent for a part of the visible range and highly reflective for the red and infrared red section of the light spectrum. For an optimum DBR structure, we investigate the absorption characteristic of a-Si:H film and different SiN:H films with various nitrogen contents. Films with the highest refractive index contrast and lowest visible range absorption are selected for the DBR fabrication. DBR structures with various periodicity are investigated in terms of transparency in the part of the visible range and reflectivity in the red and near infra-red part of the spectrum. Using the optimum DBR structure, we have fabricated a semi-transparent single junction amorphous silicon solar cell on glass substrate. Additionally, in order to study the color range and transparency of the fabricated structures, transmittance measurements are used to simulate and calculate the color filtering effect of these solar cells.

Chapter 6

Finally, this section summarizes the results and contributions of this research, and provides suggestions for further studies on a-Si based solar cells on transparent plastic substrates.

Chapter 2

Materials and Methods

2.1 Introduction

This chapter briefly presents the material properties, deposition techniques, and characterization setups used throughout this work. This chapter starts by introducing the substrate selection criteria and the possible plastic candidates that we can employ to fabricate flexible thin film silicon solar cells. Among these plastic substrates, PEN plastic from DuPont Teijin films company is selected as the cell substrate. To comply with the low thermal budget of this plastic substrate, all the thin films should be optimized and deposited at a temperature not exceeding 150 °C. Based on this criteria the main deposition method is plasma enhanced chemical vapor deposition (PECVD) which is used for the deposition of silicon layers. The front contact is a transparent conductive oxide such as ITO or ZnO, either deposited by low temperature sputtering or comes as the optimized glass coating (Asahi U-type glasses). The back contact is usually made by sputtering Aluminum at room temperature. Structuring of the cells is achieved by using a shadow mask for the back contact and dry etching of the silicon with SF_6+O_2 gas mixture.

In this chapter, protocrystalline silicon (pc-Si:H) is introduced as the most suitable absorber layer for the single junction thin film silicon solar cells. This material is formed right at the threshold between amorphous and mixed amorphous-

microcrystalline films. In addition, doped nanocrystalline silicon is introduced and suggested as the the best material choice for the cell doped layers.

Finally, solar cell test fixture and different film and cell characterization techniques such as Raman and optical spectroscopy, external quantum efficiency, current voltage measurements (I-V), and Transmission electron microscopy (TEM) are briefly explained.

2.2 Substrate selection criteria

In order to select a suitable plastic substrate, one should take into account the following properties [21, 26]:

1. *Thermal stability:* plastic films suffer from variable and undesirable dimensional changes at and over the glass transition temperature (Tg). Therefore, a plastic with a higher Tg is more desirable.

2. *Mechanical stability:* the substrate coefficient of thermal expansion should be as close as possible to that of the TCO and silicon layers. According to its definition, Coefficient of Thermal Expansion[1] (CTE) describes the fractional increase of length per unit rise in temperature [ppm/°K]. A mismatch between CTE of different layers will lead to mechanical issues such as bending, rolling and even peeling off the deposited films. Table 2.1 shows thermal expansion coefficient of some solar cell-related materials.

Table 2.1: TCE of different solar cell related materials

property	c-Si	μc-Si	a-Si	ZnO	SS	Glass
CTE(ppm/°K)	1.5-4	1	3	3.2-6	10-18	0.56-9.2

[1]Temperature Coefficient of Expansion (TCE) in some sources.

3. *Surface smoothness:* The roughness of the substrate should be as low as possible to prevent shunting problems in the solar cell.

4. *Transparency:* according to this research proposal, the plastic substrates need to offer glass–like transparency.

5. *Barrier properties:* the barrier property of a film is usually defined by water vapor transmission and oxygen transmission rates. By definition, Water Vapor/Oxygen Transmission Rate (WVTR/OTR) is the steady state rate at which moisture/oxygen permeates through a film at specified conditions of temperature and relative humidity over a given period of time. The international unit for WVTR and OTR are [g/m^2/day] and [mL/m^2/day] respectively. The inherent barrier properties of optical-grade plastic films are typically of the order of 1 gr/m^2/day for WVTR and 3 mL/m^2/day for oxygen transmission rate. These values are still far from those of glass sheets (on the order of 10^{-11} g/m^2/day) and therefore, plastic substrates should be laminated with special barrier layers.

6. *Price and availability:* price and availability of plastics are important factors in industrial levels. However, these two factors are not determinant in the framework of a laboratory research.

In this research we have studied several different plastics as the possible candidates for our solar cell substrate. According to the thesis objective, the first two important criteria that we should consider are *Transparency* and *Thermal stability*. Table 2.2 compares these two characteristics for different types of plastics.

Taking into account the relative high working temperature and transparency of PEN and PET plastics, they have been initially selected as the potential cell substrates in this research. However, later on, due to the higher processing temperature of PEN plastics and to avoid any possible contamination concerns, PEN plastics have been chosen as the substrate for flexible solar cells. Table 2.3 compares the characteristics of two specific PEN and PET products from DuPont Teijin films company that have been optimized for photovoltaics applications.

Table 2.2: Transparency and Thermal characteristics of certain plastic substrates

Name	T_{max} (°C)	Transparency
Polycarbonate (PC)	115-130	Transparent
Polyethylene therephtalate (PET)	150	Transparent
Polyethylene naphtalate (PEN)	180-220	Transparent
Polyimide (PI)	250-300	Opaque
Polyetherimide (PEI)	170-200	Opaque

Table 2.3: Properties of high performance PEN and PET films [5, 27]

Property	PEN (Teonex®Q65)	PET (Melinex®ST506)
Upper Temp. for processing (°C)	180-220	150
Glass transition temperature (°C)	120	78
Surface roughness Ra (nm)	0.8	0.8
H_2O Permeability (gr/m^2/day)	1.2	4.1
CTE (ppm/°C)	18-20	20-25
Optical transmittance spectra	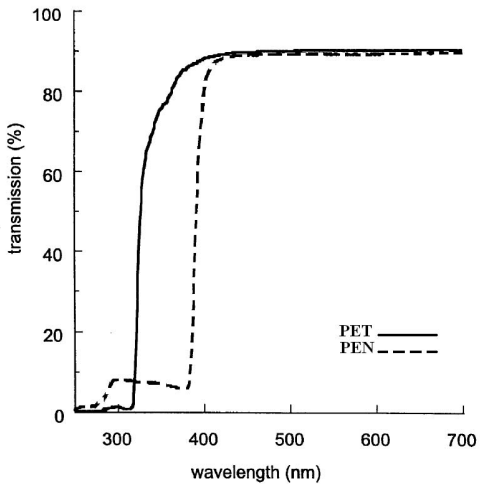	

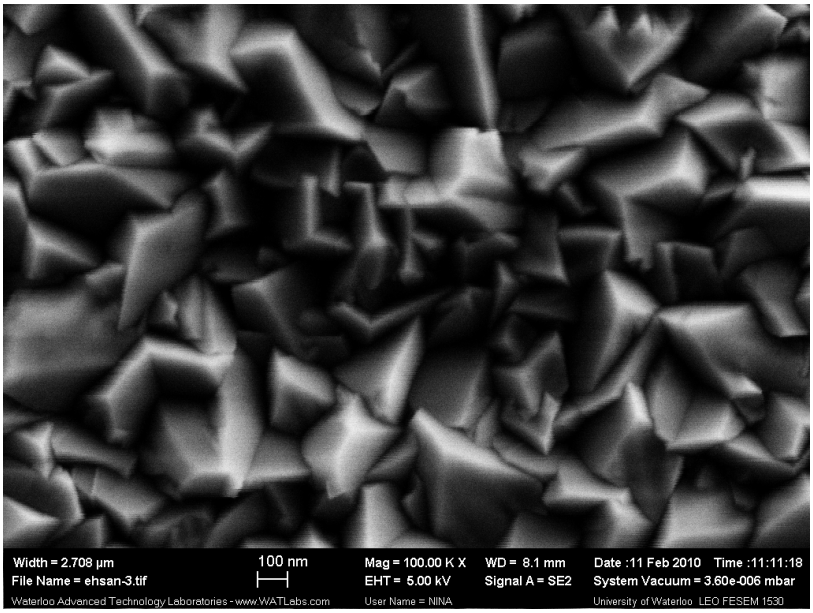

Figure 2.1: Scanning electron microscopy picture of the surface textured Asahi-U type substrate.

2.3 Reference cell substrates

In this research, most of the film and cell optimizations have been done using Corning glass (Eagle 2000) substrates. In some cases we have also used commercial Asahi-U type glasses either for the reference cell fabrication or for applications where the front contact roughness is crucial for the cell structure optimization. Usually, Asahi-U type or so-called U type SnO_2 film (deposited by Asahi Company in Japan) serves as a reference substrate in the field of thin film silicon solar cells. These substrates by providing optimized front TCO contact in terms of surface roughness and electrical conductivity, allow researchers to independently optimize other layers of a thin film solar cell. Figure 2.1 is a Scanning Electron Microscopy (SEM) image of the surface of these substrates.

2.4 Transparent Conductive Oxide

Indium Tin Oxide and Al-doped Zinc Oxide are the most common used TCO layers in thin film silicon solar cells. The low temperature budget of plastic substrates necessitates the use of ZnO:Al layers. ZnO films have a wide range of other applications than TCO layer in solar cells. More specifically, in display industry, there is a huge effort to deposit high quality ZnO films on transparent flexible substrates [28]. TCO layers can be prepared by several deposition techniques such as Magnetron Sputtering, Low Pressure CVD and Atmospheric Pressure CVD.

2.5 Texturing TCO substrates

As it was explained in the light management section, in the case of thin film solar cells we need to patten the surface of the front TCO layer to maximize the optical length of the device. The surface texture of ZnO can be obtained naturally during the growth (LP-CVD ZnO) or by post deposition chemical etching with 0.5% HCl aqueous dilution for a time varying from 4-30 seconds. Plastic substrates with low temperature resistance and low glass transition temperatures suggest a different approach. In this case, we can directly texturize the plastic substrates either by transferring a controlled roughness to the plastic or randomly texturing the substrate using a Reactive Ion Etching machine.

2.6 p-i-n Silicon Layers

2.6.1 Intrinsic Silicon Layer

Defect analysis reveals that the pure a-Si structure has a large concentration of about 10^{21} defects per cm^3. Introducing hydrogen in atomic network of this material passivates dangling bonds and reduces defect density to 10^{15}-10^{16} cm^{-3}. Hydrogen atoms can be introduced by hydrogen dilution or increasing the plasma power or frequency

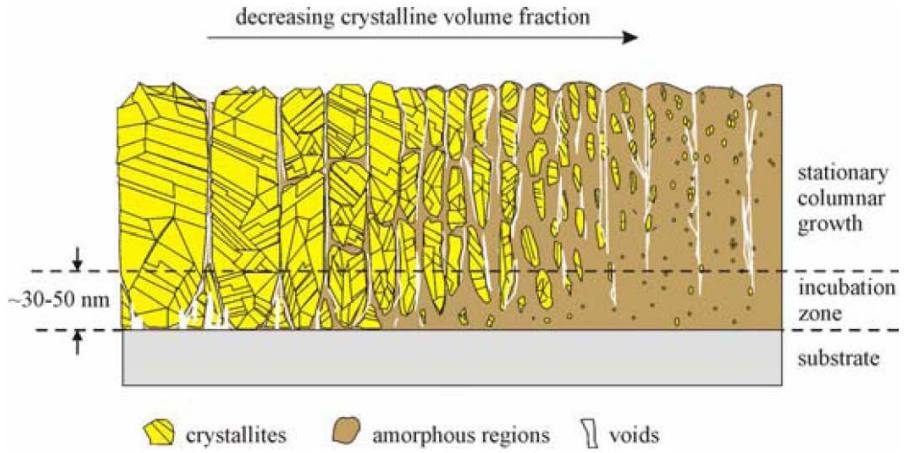

Figure 2.2: Schematic diagram represents different microstructure possibilities of deposited silicon [29].

in a PECVD deposition system. Having said that hydrogenated amorphous silicon absorber layers prepared with hydrogen dilution of silane gas result in better performance compare to the conventional undiluted counterparts. In low temperature regimes (<300 °C), hydrogen dilution ratio which is defined as R = H_2/SiH_4 plays a critical role in tunning silicon microstructure. As it can be seen from Figure 2.2, by changing the hydrogen dilution and keeping other parameters constant, a range of different microstructures from amorphous to highly microcrystalline can be achieved. However, taking into account the film thickness, crystallization process goes through different phases. Crystallization process along the vertical cross section of Figure 2.2 can be described as follows: typically, the growth is initiated by forming an amorphous incubation layer at the interface of the film and substrate. In some applications like Thin Film Transistors (TFT), this layer has a detrimental effect. Following this incubation layer, a mixed phase of amorphous tissue and nanocrystals appears on the growing surface. As the film becomes thicker, the crystal fraction is increased and saturated after a specific thickness [29]. Crystallinity of the intrinsic layer is one of the key parameters to manipulate the open–circuit voltage values in μc-Si solar cells. It has been shown that by increasing the hydrogen dilution, the material band-gap is widened and defect density reduced. However, further increasing of the hydrogen dilution after a specific value results in deterioration of the open-circuit voltage. Ac-

cording to [30] there is a correlation between hydrogen dilution, film thickness and inclusion of microcrystallites in the deposited film. It means that there is a threshold between the amorphous and mixed amorphous-microcrystalline films. Koch et al. was the first to exploit this condition and named this phase as protocrystalline silicon for the films deposited at the maximum possible R value that can be sustained for adequate film growth without crossing the above mentioned threshold. Figure 2.3 is a deposition phase diagram where the solid and dashed lines identify the amorphous to mixed and mixed to microcrystalline phases, respectively. As it can be seen from this figure, if a protocrystalline film were to continue accumulating, the amorphous to mixed phase transition would eventually occur. In this figure, the transitions are defined by *in situ* real time spectroscopic ellipsometry studies. In these method, changing the surface roughness is used as the phase transition criteria [30]. In the case of solar cells, it would be more convenient to use open-circuit voltage measurements (for a given i-layer thickness) to define amorphous to mixed phase transition [31]. It should be noted that the phase transition is very sensitive to the nature of the substrate. Therefore, it is expected that a microcrystalline doped layer would result in a mixed amorphous-microcrystalline i-layer in a solar cell that is designed with a protocrystalline absorber layer [30]. In addition to the hydrogen dilution, the phase transition is very sensitive to the condition and geometry of the plasma chamber. So, in this research we need to obtain the threshold dilution ratio according to the available plasma system.

2.6.2 Doped Silicon Layer

During film deposition, the type and magnitude of silicon films can be manipulated by introducing phosphine (PH_3) for p-doped or diborane (B_2H_6) / TMB for n-doped silicon films. In an a-Si based solar cell, these layers induce an internal electric field across the i-layer. While dangling bonds in i-layer can act as donors and acceptors for the electron-hole pairs, a strong electric field can effectively improve the collection of these charge carriers. On the other hand, in order to reduce the internal resistance of

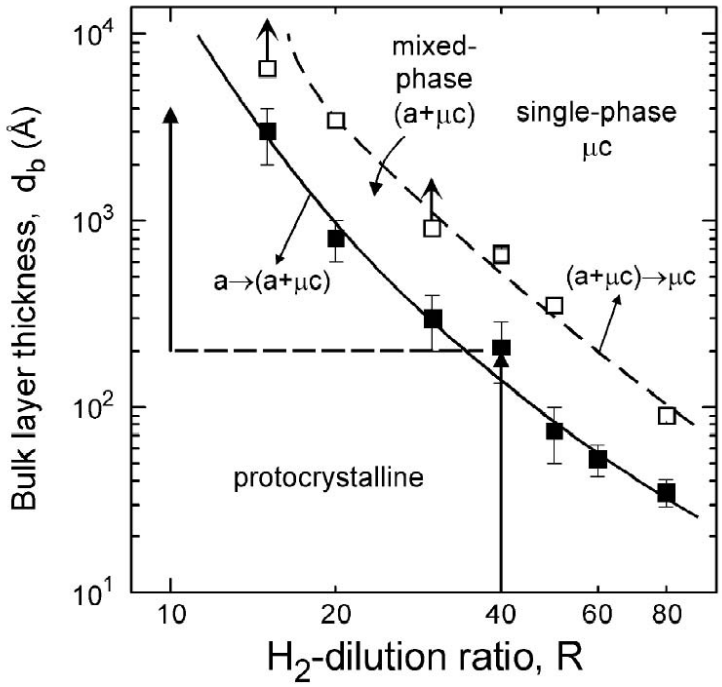

Figure 2.3: Deposition phase diagram for Si film growth on amorphous substrate at 200 °C [30].

solar cells, these doped layers should be highly conductive. In crystalline silicon, high dopings result in high conductive layers. As it can be seen from Figure 2.4, in a thin p-type microcrystalline layer obtaining highly doped conductive layers is extremely difficult. In this material, high crystallinity corresponds to high conductivity. As a result, Figure 2.4 implies that there is a difficulty of crystalline nucleation for heavily doped microcrystalline p-doped layers. According to [32], low temperature deposition of p-doped layers is effective to improve the crystallinity. Figure 2.5 shows the deposition temperature dependence of the crystallinity for boron doped microcrystalline films. As we can see in this figure, the optimum temperature for a high crystalline p-doped layer is in the range of 140-180 °C which is close to our plastics upper temperature limit. In solar cells, p-doped layer acts as a window layer. So, the optical characteristic of this layer in the short-wavelength region is of great importance. To minimize the short-wavelength absorption losses in this layer, a film with thin thickness and wide optical bandgap properties is chosen [23].

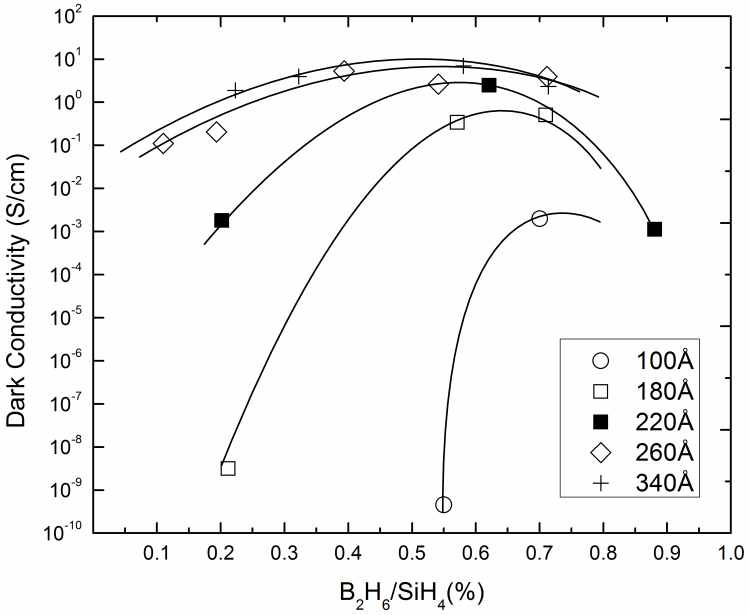

Figure 2.4: Dark conductivity versus diborane percentage for different thicknesses after [32].

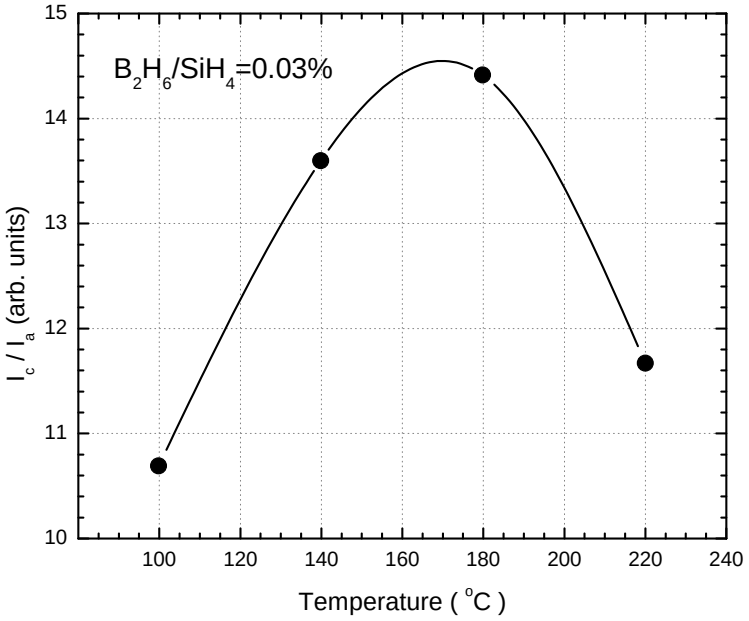

Figure 2.5: Deposition temperature dependency of the Raman crystallinity after [32].

On the other hand, optical band gap of microcrystalline silicon decreases by increasing the crystallinity of the underlying p-doped layer. As a result, one should pay special attention to the trade-offs existed in designing an optimum p-doped window layer.

2.7 Back Reflectors

In amorphous silicon based solar cells, the thickness of the intrinsic layer is limited to $300-400$ nm, imposed by the low diffusion length of carriers in a-Si material [1]. The employment of such a thin absorber layer, results in low absorption efficiencies for Red and near-IR photons ($\lambda > 600$ nm). One widely used solution to overcome this problem is to introduce light trapping schemes. These schemes are typically based on the light scattering at the rough interfaces, and the employment of highly reflective back contacts. The back metallic contact is either silver (Ag) or aluminium (Al); where aluminium is preferred due to its lower price and higher availability. However, within the wavelength range of 600-800 nm, aluminium has a reduced reflectivity due to its interband absorption at $\lambda \approx 800$ nm [33]. Recently photonic crystals and plasmonic back reflectors have garnered attention as highly-effective back structures for thin film silicon solar cells.[34, 35, 36, 37, 38] Although two- or three-dimensional back structures seem promising for efficient light trapping, one-dimensional photonic crystals known as Distributed Bragg Reflectors (DBRs) are more compatible with large area production technologies. DBR structures consist of repeating sequence of layers of two optical materials with different refractive indices. The thickness of each layer is determined as the one-quarter of the wavelength for which the DBR is designed. In this research we have designed DBR structures for application as the back reflector in a-Si solar cells. The optimized DBR structures are fabricated and their optical properties are investigated and compared to those of conventional Al back reflectors. The DBR structures considered in this work consist of stacks of a-Si/SiN for maximum reflectance in the wavelength range of 600-800 nm.

2.8 Thin Film Deposition Techniques

2.8.1 Silicon film deposition

This section addresses different thin film silicon deposition techniques which are usually employed by researchers and industry to fabricate amorphous-based thin film solar cells.

Radio Frequency Plasma Enhanced Chemical Vapor Deposition (RF-PECVD):

This method is the most commonly used deposition technique both in laboratory and industry scales. In RF-PECVD, silicon layers are deposited as a result of silicon bearing gas decompositions and surface reactions. The gas dissociation is accomplished by collisions between the gas molecules (usually SiH_4), and accelerated secondary electrons in the plasma. The reactive particles of dissociated gas molecules, known as radicals, undergo different surface reactions, and finally form the silicon layers. In RF-PECVD the excitation frequency of plasma is 13.56 MHz. Utilizing this technique, one can deposit device quality silicon layers at substrate temperatures as low as 100 °C. The only issue with RF-PECVD is its low deposition rate in the range of 1-2 Å/s [1].

Very High Frequency PECVD (VHF-PECVD):

In order to improve the deposition rates of RF-PECVD technique, in 1987, researchers at the University of Neuchatel introduced the VHF-PECVD deposition method. In this method, the plasma is excited in a higher frequency between 30MHz and 300MHz. By increasing the excitation frequency, both the sheath thickness and the RF voltage at the electrode are reduced. Consequently, it improves the coupling of RF power into the bulk plasma. The increased RF power, enhances silane molecules dissociation and the flux of radicals and ions onto the substrate. On the other hand, the reduced voltage drop across the plasma sheath leads to a softer ion bombardment and a better

material structure. This VHF technique can offer high quality microcrystalline films with deposition rates in the range of 1-3 nm/s [1]. However, the nonuniformity of the voltage distribution on the conventional VHF electrodes makes it almost impossible to obtain uniform large-area (in the range of 1 m^2) films. This voltage nonuniformity occurs due to the formation of standing waves on the electrodes with dimensions comparable to $\lambda/4$; where the λ is the excitation frequency [39]. Recently, researchers at the Mitsubishi Heavy Industries have developed a so-called ladder shaped electrode for large area plasma CVD to replace the conventional parallel plate type electrodes [40]. Using 60MHz frequency, they have succeeded in depositing uniform amorphous silicon films with the deposition rate of 1.7 nm/s on 1.4 m $\times$ 1.1 m glass substrates. Currently, Flexcell company [10] employs VHF-PECVD technique to deposit its solar cells layers.

Hot Wire (HW):

In Hot Wire deposition technique, the energy for dissociation of gas molecules is provided by a hot filament with temperature of 1600-2000 °C. Compared to PECVD, it seems that, without detrimental effect of surface bombardment, this method would result in higher quality microcrystalline films. However, it has been proved that some low energy ion bombardments can be beneficial in terms of film microstructure. Technical issues such as overheating of the growing film by thermal radiation of filament, the necessity of regular replacement of filament and poor uniformity in the large area films, have limited the application of this method to research and development purposes [1].

While HW-CVD and HF-PECVD methods offer high deposition rates, RF-PECVD is still the most attractive deposition method for solar cell industry. As mentioned above, the other two methods have not reached enough maturity to be popular in industry. All thin films and solar cells investigated in this thesis are fabricated using a conventional multichamber (13.56 MHz) plasma enhanced vapor deposition (PECVD) system. This system consists of separate PECVD chambers for dielectric, undoped

and doped film deposition, and a load-lock for handling the substrate. A robotic arm transfers substrates between different chambers without breaking the vacuum.

2.8.2 TCO deposition

Sputtering

In the sputtering technique, the target is bombarded by high-energy ions of an inert gas (usually Ar); thereby target particles are dislodged and deposited on the substrate. The physical nature of this process allows a wide range of materials to be used as a target. In addition, applying a magnetic field structure to the plasma, deflects and confines secondary electrons near the target. As a result, the probability of the impact ionization is increased significantly. In a so called magnetron plasma sputtering system, the high density of ions in the plasma bulk is lead to an increase of ion bombardment and consequently a higher deposition rate. The capability of depositing TCO and metallic films at substantially low temperatures (as low as 50 °C) makes sputtering process the best option for plastic substrates. However, in the case of plastic substrates, the process power should be carefully adjusted to prevent overheating of the substrate during sputtering.

Chemical Vapor Deposition (CVD)

In a CVD process, the substrate is exposed to one or more thermally created precursor. Due to the reaction or decomposition of these precursors, the desired film is deposited on the substrate. According to the operating pressure, there are different kinds of CVD processes. Although CVD deposition systems are much more simple and cost effective than sputtering tools, usually the optical and electrical properties of the films deposited by these systems strongly depend on the processing temperature. For instance, to deposit device grade ZnO films in Atmospheric Pressure Chemical Vapor Deposition (APCVD) and Low Pressure Chemical Vapor Deposition (LPCVD)

systems one requires at least 400 °C and >150 °C processing temperatures, respectively [1, 41].

2.9 Characterization techniques

2.9.1 Film thickness measurement

For film thickness measurements, samples are patterned using photolithography to make an array of steps. Then, a Dektak 8 Stylus profilometer has been used to mechanically scan these step patterns and measure the films thickness in different areas across the sample. Reported film thicknesses and deposition rates are the average values of these measurements.

2.9.2 Film conductivity and sheet resistance

For photo- and dark-conductivity measurements (σ_{ph} and σ_d), 18-mm long and 1-mm apart coplanar aluminum contacts are deposited through a shadow mask using Edwards E306A RF sputtering system. The conductivities are then retrieved from the slope of the film I-V characteristics of the deposited films. The I-V characteristics are measured with a ramp rate of 1 V/s by a Keithley 4200 semiconductor characterization system connected to a Cascade 11000 probe station. For photo-conductivity measurements, a 10 W lamp is used to illuminate the substrate during the I-V measurements. The intensity of this light is kept constant during all the photo-conductivity measurements. For conductive films (Al and TCO), sheet resistance is measured using a non-contact resistivity measurement machine.

2.9.3 Raman spectroscopy measurement

Raman spectroscopy is employed to estimate the crystalline fraction (X_c) of the films deposited on glass. Raman spectra are measured in the backscattering configuration

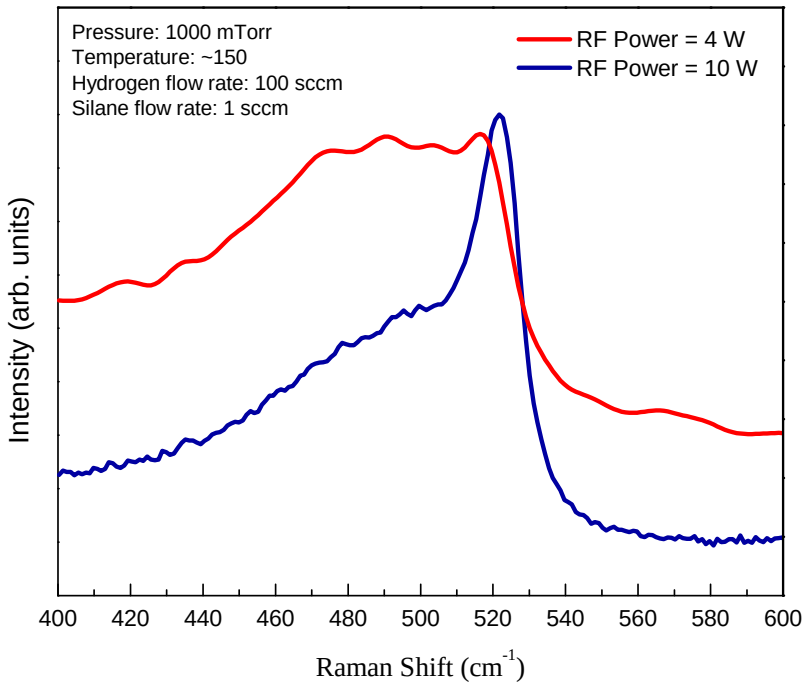

Figure 2.6: Raman spectra of deposited films with plasma power of 4 W and 10 W.

using a Renishaw micro-Raman spectrometer with a 488 nm excitation laser line. Figure 2.6 shows the Raman spectra and the deposition parameters for two different samples.

In this figure the peaks at 520cm^{-1} and 480^{-1} corresponds to the crystalline grain and amorphous tissue, respectively. Usually, the Raman spectrum is fitted with two Gaussian peaks at the above mentioned Raman shifts. The Raman crystallinity is then evaluated from the following relationship:

$$X_c = \frac{I_c}{I_a + 0.8 \times I_c} \tag{2.1}$$

In this relationship X_c is the film crystallinity, and I_c and I_a are Raman intensities at 520 cm^{-1} and 480 cm^{-1} respectively. Figure 2.7 shows the decomposition of the Raman spectra of the second sample.

As it can been seen from Figure 2.7 the resultant Gaussian curve is not fitted to the experimental Raman spectrum. Therefore, the Raman spectra of the film is

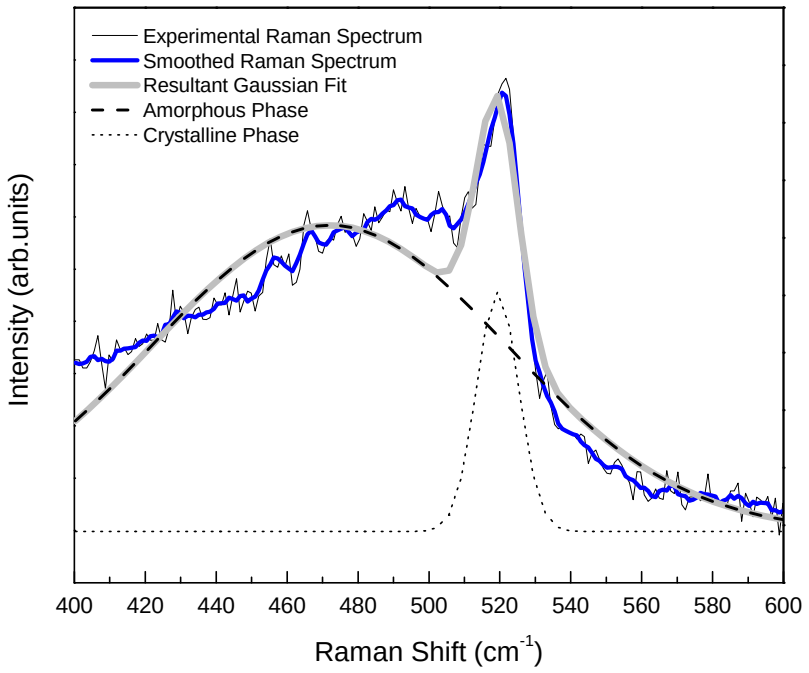

Figure 2.7: Raman spectrum decomposition into Gaussian peaks at 480 cm^{-1} and 520 cm^{-1}.

deconvoluted with three peaks as depicted in Figure 2.8. In this figure, along with the peaks at 452 cm^{-1} and 521 cm^{-1} the third peak shows a tail toward a wavenumber around 500 cm^{-1}. According to [42] the position and shape of the peaks can be affected by different parameters such as sample temperature, stress in the sample, and size of the crystallites. So, the peaks at 452 cm^{-1} and 521 cm^{-1} should represent the amorphous and crystalline phases. The third peak at 500 cm^{-1}, in the literature, has been attributed to crystallites of diameters lower than 10 nm, a silicon phase that could result from twins, or the defective part of the crystalline phase [42].

2.9.4 Optical measurement

Usually the optical constants (refractive index and extinction coefficient) and film thickness are determined from the transmission spectrum of thick ($\geq$ 100 nm) layers using the well-known envelop method [43]. However, the optical model of uniform media may not be valid for thick polymorphous films because of the structural non-

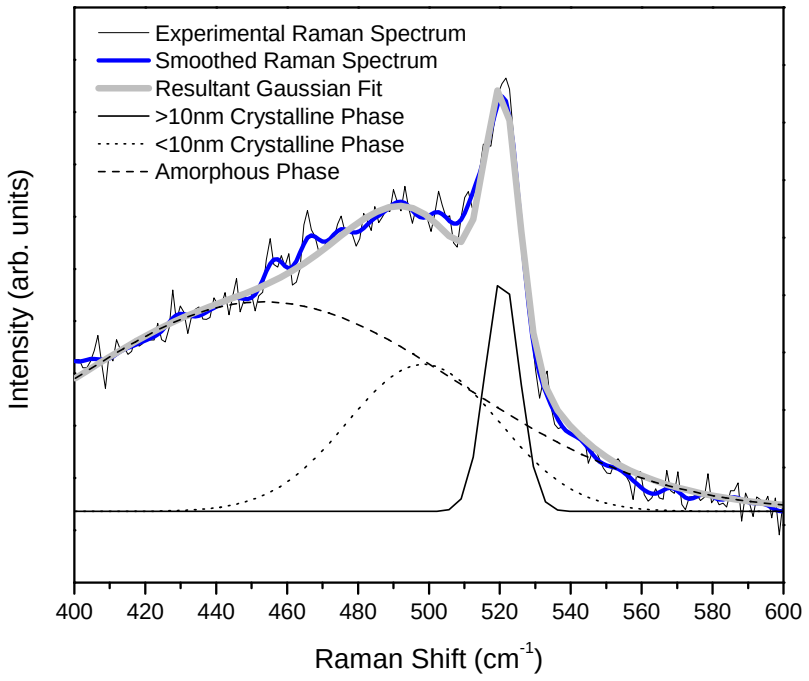

Figure 2.8: Deconvolution of the Raman spectrum into three peaks.

uniformity in the direction of growth. In this study, the layers are so thin that there are no interference fringes in the optical spectra. Here, we use a numerical method for determining the complex refractive index $(n - ik)$ from reflectance and transmittance of supported thin films. In this research, the refractive indices of the amorphous silicon and amorphous silicon nitride films used in the DBR back reflector structures are extracted using PUMA software [44].

The spectrometer is used for transmission (T), reflection, diffuse transmission (DT), or diffuse reflection (DR) measurements for the wavelength range 300 nm to 2500 nm. The UV/VIS/NIR spectrometer used is a Perkin Elmer lambda 1050 with 150 mm InGaAs integrating sphere. The T and R of layers deposited on glass substrate are measured with light impinging from the layer side. From this, the absorption (A) is calculated from A = 1-T-R.

2.9.5 Cross sectional analysis

The cross-section of the layers is also analyzed by transmission electron microscope (TEM). The preparation for TEM is done by focus ion beam (FIB) or tripod technique at Canadian Centre for Electron Microscopy (CCEM) McMaster University.

2.9.6 Solar cell measurements

The fabricated cell structures are composed of substrate / nc-Si p-layer / a-Si / nc-Si n-layer/ Back reflector. Sputtered Al (200 nm) or ZnO (600 nm) films defined different cells with areas ranging from 0.0078 to 1 cm^2 on the substrate using a shadow mask shown in Figure 2.10.

To make electrical connection to the front TCO electrode, the p-i-n layers are etched using a Reactive Ion Etching (RIE) machine. A squared glass wafer is used to cover the sputtered aluminum contacts and the surrounding silicon film. After etching the p-i-n structure, the front TCO contact is appeared on the areas exposed to the RIE. Etching process is optimized to keep the underlying TCO layer intact.

In cases where the DBR stacks have covered the back contact layer (here a TCO layer instead of Aluminum), another shadow mask is used to create via holes through DBR structures for measuring probes. Front TCO contact is accessible after p-i-n layer etching as explained above.

As it is mentioned in the light management section, for solar cells with metallic back reflectors, a TCO interlayer with a thickness of 80-100 nm is inserted between n-doped layer and the back electrode. In this research, TCO interlayer is directly deposited on the n-doped nanocrystalline silicon layer and then the Aluminum contacts are sputtered through the shadow mask. In this process sequence the TCO interlayer connects all the back electrodes on the wafer. In order to isolate individual cells from each other, this layer should be removed from areas between the metallic electrodes. This etching process is carried out by dipping the whole sample into a 10% diluted HCl solution for a very short period of time. Here, the Aluminum contacts act as a

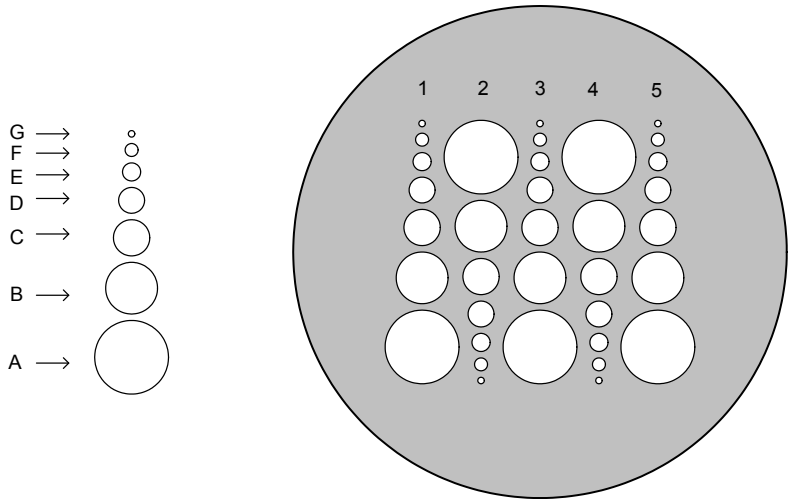

	R (cm)	A (cm^2)
A	0.57	1
B	0.4	0.5
C	0.28	0.25
D	0.2	0.125
E	0.14	0.0615
F	0.1	0.0314
G	0.05	0.0078

Figure 2.9: Shadow mask used to fabricated cells with different areas on a 3 inch wafer.

protecting mask for the underlying TCO/p-i-n/TCO structure. The etching process should be carefully optimized to avoid unintentional TCO or Al etchings.

In order to facilitate the measurement process, a custom Cell Readout Bord (CRB) has been designed and fabricated. This board consists of a Polyvinyl chloride (PVC) fixture, housing a 3"wafer. Each individual cell on the wafer is selected by manual electric switches that connect the cell electrodes to a low impedance SMA[2] connector. Here, the electrical connections are made through miniature spring contact probes

[2]SubMiniature version A

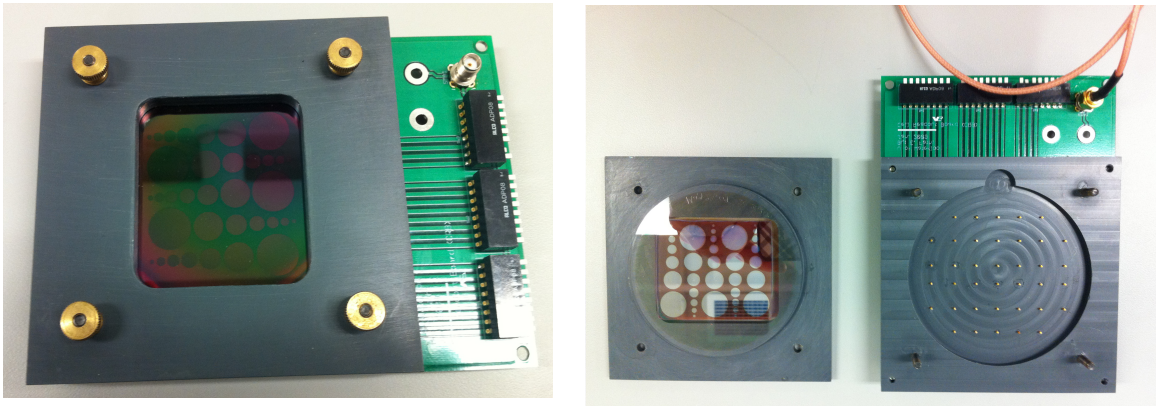

Figure 2.10: Cell Readout Board that is used for cell measurements.

inserted at the bottom of the loading part. Figure 2.10 shows the different parts of the readout board.

The external quantum efficiency (EQE) is the ratio of the number of electrons collected at the device electrodes to the number of photons hitting the cell for every light wavelength impinging on the front side of the solar cell. So, (1-EQE) gives the portion of photons which are lost by reflection from the cell surface, absorbed in non-active layers (doped layers, TCO, metal) or recombined in the absorber layers. In this thesis all the EQE measurements are done using a PVM[3] solar cell spectral response system. The measured quantity of this instrument is the ratio of the cell current $I_{cell}(\lambda)$ to the beam power. This ratio is converted to units of quantum efficiency by using the following equation:

$$QE(\lambda) = 100\% \times \frac{hc}{e} \times \frac{1}{\lambda} \times \frac{I_{cell}(\lambda)}{R(\lambda)} \tag{2.2}$$

where h is Plancks constant, c is the speed of light, e is the electron charge, $I_{cell}(\lambda)$ is the current of the calibrated reference photo-detector and $R(\lambda)$ is the known spectral response of the reference detector. The short circuit current (I_{sc}) can be calculated from the EQE measurement $QE(\lambda)$ and weighted with the AM 1.5 solar flux $\phi(\lambda)$ integrated over the wavelength range of 400-800 nm:

$$J_{sc} = q \int_{\lambda=400}^{800} QE(\lambda)\phi(\lambda)d\lambda \tag{2.3}$$

[3]PV Measurement Inc.

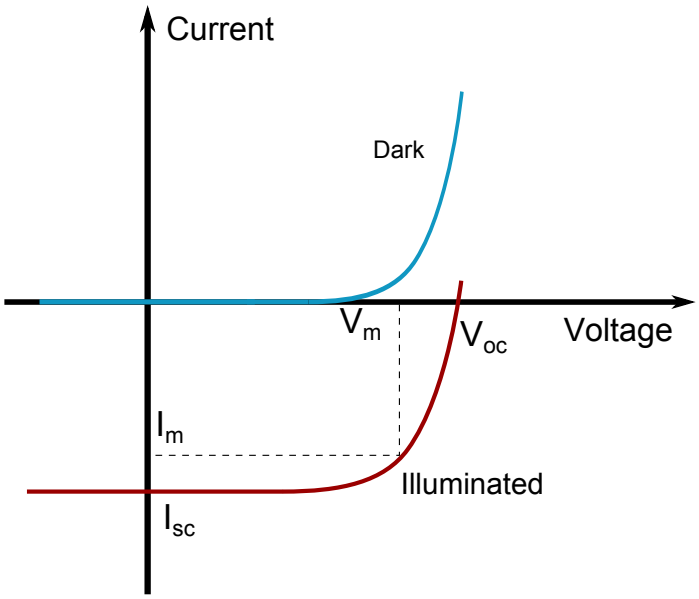

Figure 2.11: Dark and illuminated I-V measurements of a typical solar cell.

Open circuit voltages and fill factors of the solar cells are obtained from current-voltage (I-V) measurements performed at 25 °C with a standard solar simulator and a SCDS model I-V data acquisition system. The I-V curve shows the measured current for different applied voltages under the standard AM 1.5 illumination. As it is shown in Figure 2.11 the maximum output power of the solar cell is given at V_m and I_m. Using this curve, the following characteristics are defined: short circuit current (I_{sc}), open circuit voltage (V_{oc}) and the fill factor (FF). Consequently conversion efficiency of the cell is defined as:

$$FF = \frac{V_{max} \times I_{max}}{V_{oc} \times I_{sc}} \tag{2.4}$$

$$\eta = \frac{V_{max} \times I_{max}}{incident - power} = \frac{I_{oc} \times V_{oc} \times FF}{100[mW/cm^2]} \tag{2.5}$$

The accurate surface area of the laboratory test cells is not often well defined and consequently the estimation of the current densities from the I-V measurements is difficult. On the other hand, the spectrum provided by a solar simulator does not exactly represent AM1.5. So, the short-circuit current density is calculated from the EQE measurement as described above.

In addition to the illuminated I-V measurements, dark characteristic of a typical

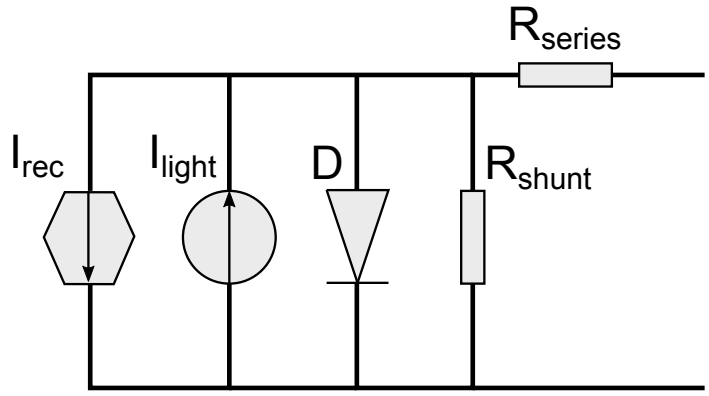

Figure 2.12: Equivalent circuit for a typical solar cell.

solar cell is shown in Figure 2.11. This curve is identical to the I-V characteristic of a two-terminal diode. For an ideal solar cell we can regard the output current as the sum of the current through the p-n junction in the dark and the current from a photogenerated current source in parallel with the diode. For a practical device, we need to extend this simple model by three additional elements (Figure 2.12). The resistance R_p in parallel with the diode and current source represents the shunts that occur in a real solar cell across the electrodes. The series resistance, R_s, accounts for all voltage drops between the transport resistance of the device and its connections to the load. Finally, the recombination current source, I_{rec}, models the recombination events in the intrinsic layer and its value depends on the current and voltage across the ideal diode.

Chapter 3

Optimization of Individual Thin Films: Results and Discussion

3.1 Introduction

In this chapter, we investigate the optimization of the core silicon materials in a-Si based solar cells, i.e. doped nanocrystalline silicon and undoped amorphous silicon layers, at a low substrate temperature of 135 °C. All layers are deposited and optimized on corning glass substrates. For doped silicon layer optimization, we start with a previously optimized undoped nanocrystalline silicon layer. This material which is deposited at the substrate temperature of 300 °C shows high crsyftalline fraction of about 60% for a thickness of 15 nm. In this chapter we study the crystallinity of this material at the low deposition temperatures. The goal at this part, is to explore the formation of nanocrystalline grains at the early stage of the film growth. Based on the results of this study, a very high hydrogen dilution ($\frac{[H_2]}{[SiH_4]}$)[1] and a low plasma power density as the PECVD process parameters, result in the thinnest possible nc-Si layers which is required for the silicon tissue of the doped layers in an efficient silicon solar cell. By adding hydrogen diluted phosphine or trimethylboron (TMB) gases to the deposition process of this undoped nc-Si:H film, n- or p-doped films

[1]Note that the notation $\frac{[H_2]}{[SiH_4]}$, denotes flow rate ratios.

are obtained, respectively. The evolution of the structural and electronic properties of these doped films are investigated by gradually varying the phosphine-to-silane and the TMB-to-silane flow ratios. Undoped amorphous silicon films are deposited by varying silane-to-hydrogen ratios while keeping other deposition parameters constant. Here, photosensitivity σ_{photo} / σ_{dark} is considered as the quality factor for the undoped silicon layers.

3.2 Undoped nanocrystalline silicon

M. R. Esmaeili-Rad et al.[45] have recently reported on the deposition of high quality nanocrystalline films.The enhanced crystallinity and electrical quality of this film is attributed to the formation of crystalline grains at the early stage of the film growth. Taking into account this promising result, we have develop nc-Si n- and p-doped layers for applications in thin film solar cells. However, using the plastic substrates necessitates a lower deposition temperature. As a result, we expect to obtain a lower crystallinity by using the same deposition parameters. Figure 3.1 shows the Raman spectra of undoped nc-Si:H films deposited at 135 °C with thicknesses of 40 nm and 15 nm. The RF power density, pressure, and hydrogen dilution ratio, are fixed at 9 mW/cm^2, 900 mTorr, and 100, respectively. This figure shows that as the film becomes thinner, the peak at 520 cm^{-1}, characteristic of crystalline Si phase, decreases. However, even at 15 nm, the film shows higher crystalline peak at 520 cm^{-1} compare to the peak due to the amorphous phase at 480 cm^{-1}. This result is in agreement with the results presented in [45] for the films deposited at 300 °C. Accordingly, even at the substrate temperature of 135 °C, nanocrystalline grains can be formed at the early stages of film growth.

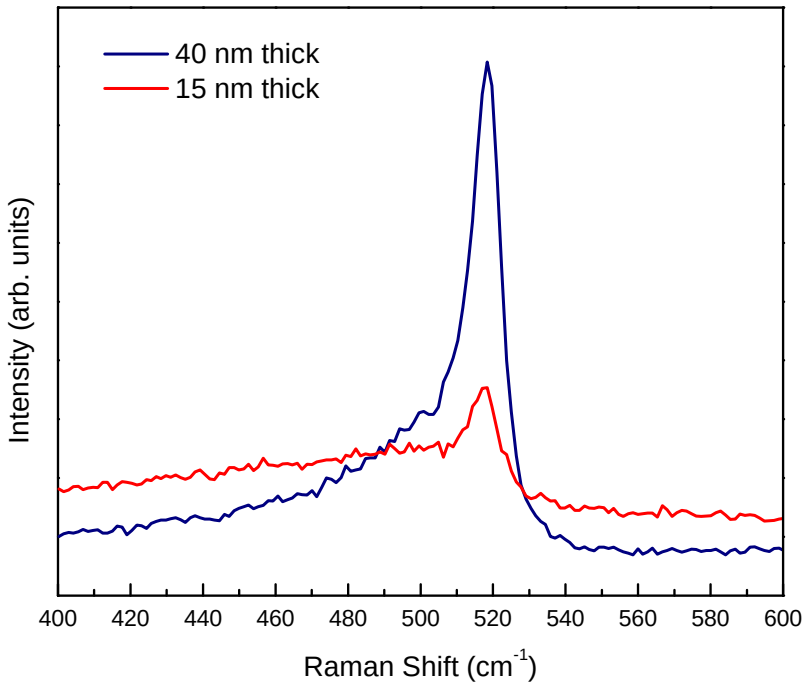

Figure 3.1: Raman spectra of undoped nc-Si:H films with 40 nm and 15 nm thickness deposited at 135 °C substrate temperature.

3.3 p-doped nanocrystalline silicon

For p-doped films, the trimethylboron(B(CH3)3) (TMB), diluted in hydrogen to concentration of 1%, is used as the doping gas. The first film series (doping series) are deposited at different TMB-to-SiH_4 flow ratios in the range of 0.2%-1.5%, but keeping the film thickness at about 60 nm. The second film series (thickness series) are deposited at [TMB]/[SiH_4]=1%, but the film thicknesses are varied from 14 to 100 nm. The RF power density, pressure, and hydrogen dilution ratio, R=[H_2]/[SiH_4], are fixed at 9 mW/cm^2, 900 mTorr, and 100, respectively.

Figures 3.2 and 3.3 show the Raman spectra of doping and thickness film series, respectively. The Raman spectra show a broad shoulder associated with the amorphous phase, and a symmetric band centered at about 517 cm^{-1}, originating from the nanocrystalline phase in the film. A good curve fit is achieved with four Gaussian peaks centered at 440, 480, 507-511, and 514-517 cm^{-1}, corresponding to the

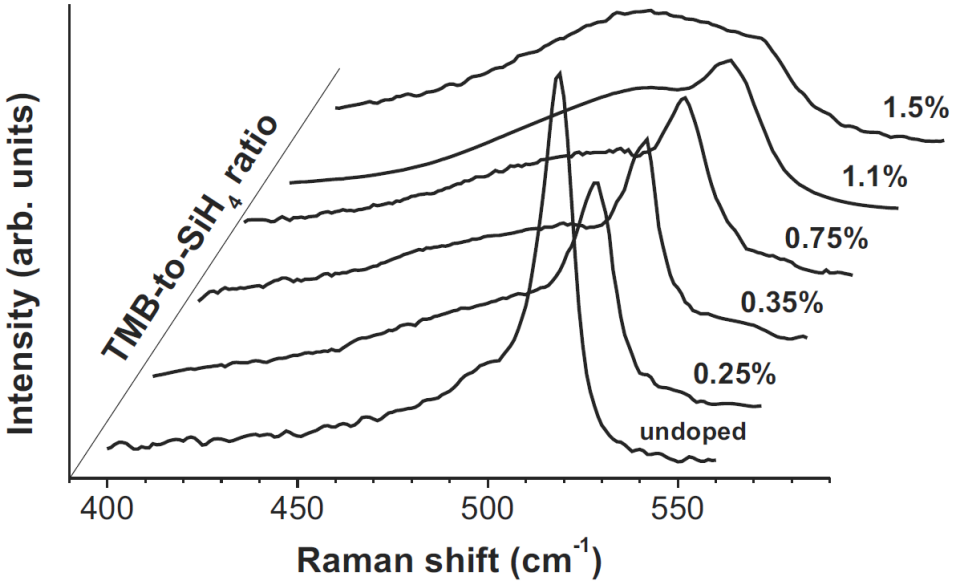

Figure 3.2: Raman spectra of nc-Si:H films of doping samples.

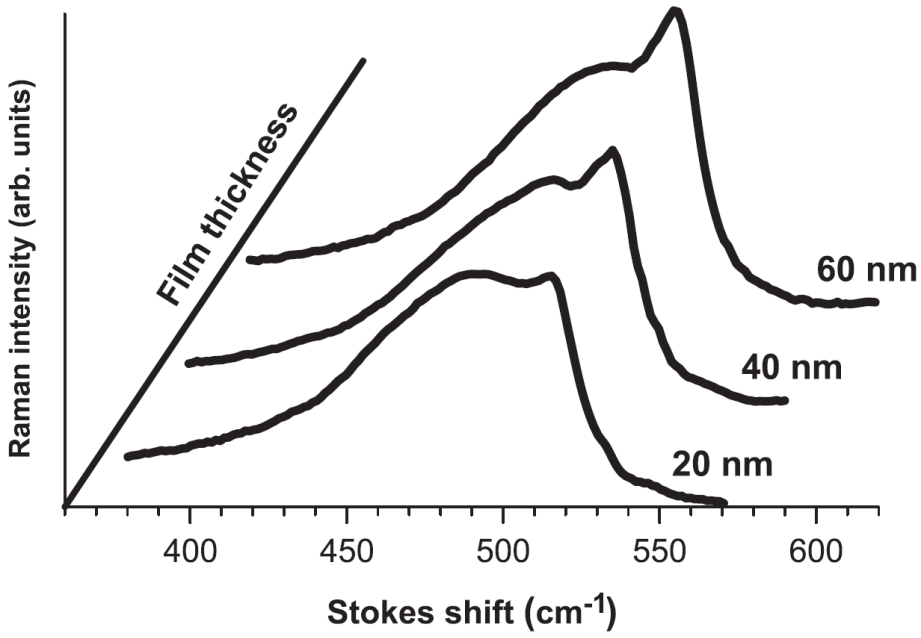

Figure 3.3: Raman spectra of nc-Si:H films of thickness samples.

longitudinal optical (LO) and transverse optical (TO) phonon modes of the amorphous fraction and optical vibrational modes of Si nanocrystals, respectively. The crystalline volume fraction, X_c, was determined using Equation 2.1. With increasing doping ratio the evaluated crystalline volume fraction decreases from 61% to 35% indicating suppression of crystalline growth (see Figure 3.2). A similar result has been reported for diborane (B_2H_6) doped nc-Si:H films deposited by PECVD [46]. For the thickness film series, the crystalline volume fraction increases from 40% to 51% in the thickness range of 20-60 nm(see Figure 3.3).

Figure 3.4 shows X_c and conductivity values as a function of the TMB-to-SiH_4 flow ratios. It is seen that increased boron doping drastically suppresses the crystalline growth. Note that in the doping range from 0.35% to 1%, X_c decreases slowly, from 46% down to 42%. In this process window, the dark conductivity reaches a pick value of 0.074 S/cm at $X_c \approx 1\%$. Conductivity decrease at higher doping ratios correlates with decreasing X_c , i.e., it is apparently related to the amorphization of the film structure. Similar dependence has been reported for TMB doped nc-Si:H films deposited by HWCVD [47].

Figure 3.5 shows a variation of dark conductivity for the thickness series. It is seen that the thin films (< 25 nm) exhibit low conductivity, comparable to that of doped amorphous silicon. For thicker films, the conductivity increases by 2-3 orders of magnitude in the thickness range of 40-80 nm and then, tends to saturate. For a 100 nm thick film, the conductivity reaches 0.2 S/cm. A similar conductivity dependence has been reported for undoped and phosphine-doped nc-Si:H films deposited by PECVD [48]. In Ref. [48], the observed abrupt change in conductivity is explained in terms of percolation theory by destruction of a percolation cluster composed of nanocrystallites as the layer thickness becomes comparable to the size of a crystallite.

To evaluate the absorption loss in the p-layer of the p-i-n cells, optical measurements are performed on the 22 nm thick films deposited on the bare glass substrate and on the glass substrate with ZnO:Al coating. Figure 3.6 and 3.7 show the transmission (T), reflection(R), and absorption (A=1-T-R) spectra of these samples. The

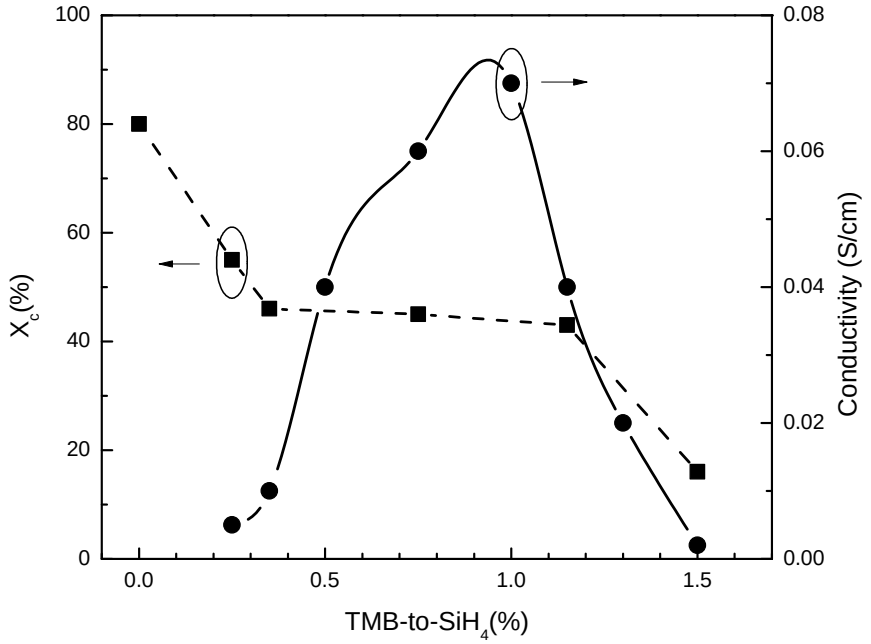

Figure 3.4: Crystallinity and conductivity of 60 nm thick nc-Si:H films as a function of the TMB-to-SiH_4 flow ratio.

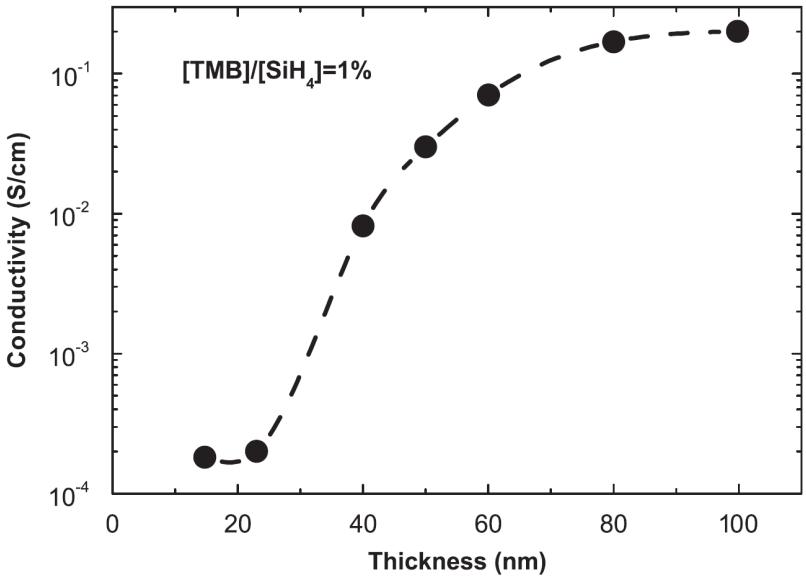

Figure 3.5: Variation of conductivity with thickness of nc-Si:H films deposited at the TMB-to-SiH_4 flow ratio of 1%.

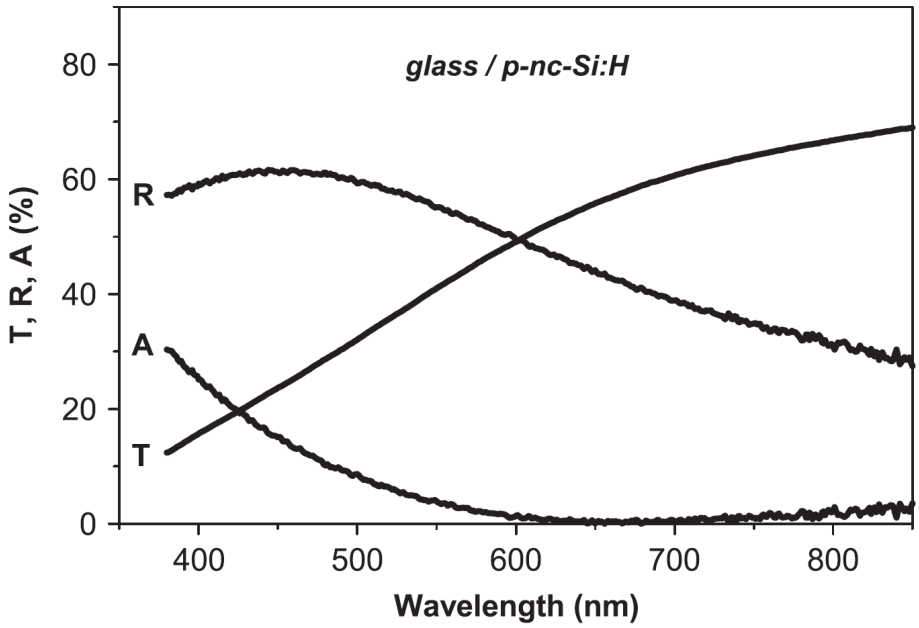

Figure 3.6: Transmission, reflection, and absorption spectra of thin (22nm) nc-Si:H film on glass substrate.

transmittance / reflectance curves of the film grown on glass are comparable to the spectra of thin (∼20 nm) nanocrystalline silicon films deposited by VHF-PECVD reported elsewhere [49]. The second sample is more transparent because the ZnO:Al coating reduces reflectance down to ∼20%. The absorption spectra of the samples look similar, yielding the absorption loss of 25% at a wavelength of 400 nm. The film transparency is better than that for a-Si:H films of the same thickness, which is consistent with the deduced Raman crystallinity. Besides, the size of silicon crystallites is believed to be small, and optical gap widening can also be substantial due to the quantum size effects [50].

Usually the optical constants (refractive index and extinction coefficient) and film thickness are determined from the transmission spectra of thick (≥100 nm) layers using the well-known envelop method [43]. However, the optical model of uniform media may not be valid for thick polymorphous films because of the structural non-uniformity in the direction of growth. In this study, the layers are so thin that there are no interference fringes in the optical spectra. We use a numerical method for

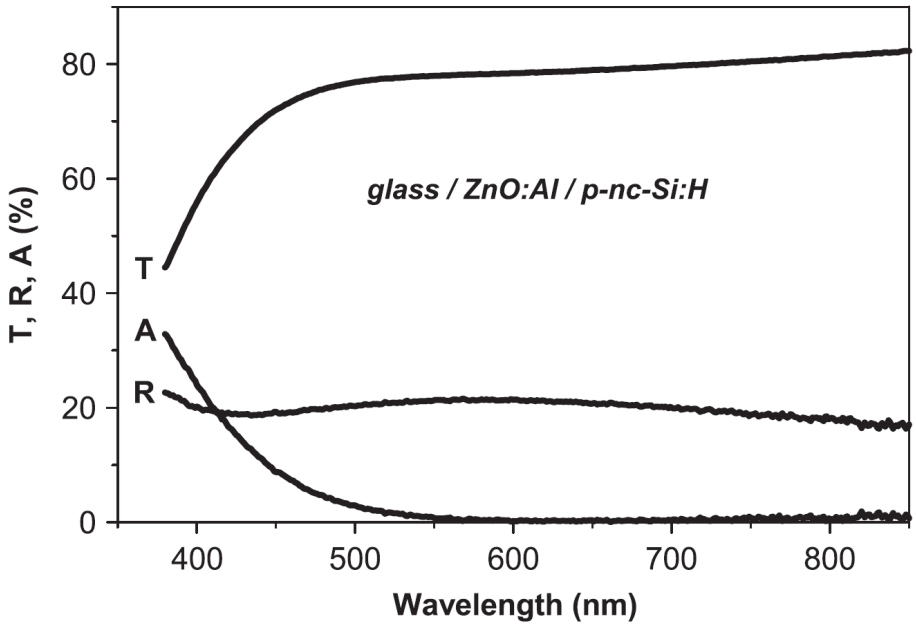

Figure 3.7: Transmission, reflection, and absorption spectra of thin (22nm) nc-Si:H film on glass with ZnO:Al coating.

determining the complex refractive index (n-ik) from reflectance and transmittance of supported thin films [51].

To evaluate the film uniformity, the optical measurements are performed for the films grown under the same deposition conditions but with different thicknesses. Figure 3.8 shows the spectral dependencies of refractive index and extinction coefficient for nc-Si films deposited at [TMB] / [SiH_4] = 1%. The dependencies for undoped nc-Si:H and p-doped a-Si:H are also shown for comparison. The deduced optical thicknesses of doped nc-Si:H layers are 19 nm and 53 nm, and that for the undoped layer is 38 nm. Depending on the film crystallinity, the extinction coefficients of nc-Si:H in the visible region are a factor of 2-3 lower than those for a-Si:H. Spectral dependence n(λ) in the long-wavelength region can be accurately represented with the function [52]:

$$n(\lambda) = n_\infty + \frac{a}{\lambda^\gamma} \tag{3.1}$$

where a is a constant, γ is the function parameter typically between 2 and 5, and n_∞ is the refractive index when $\lambda \rightarrow$ infinity.

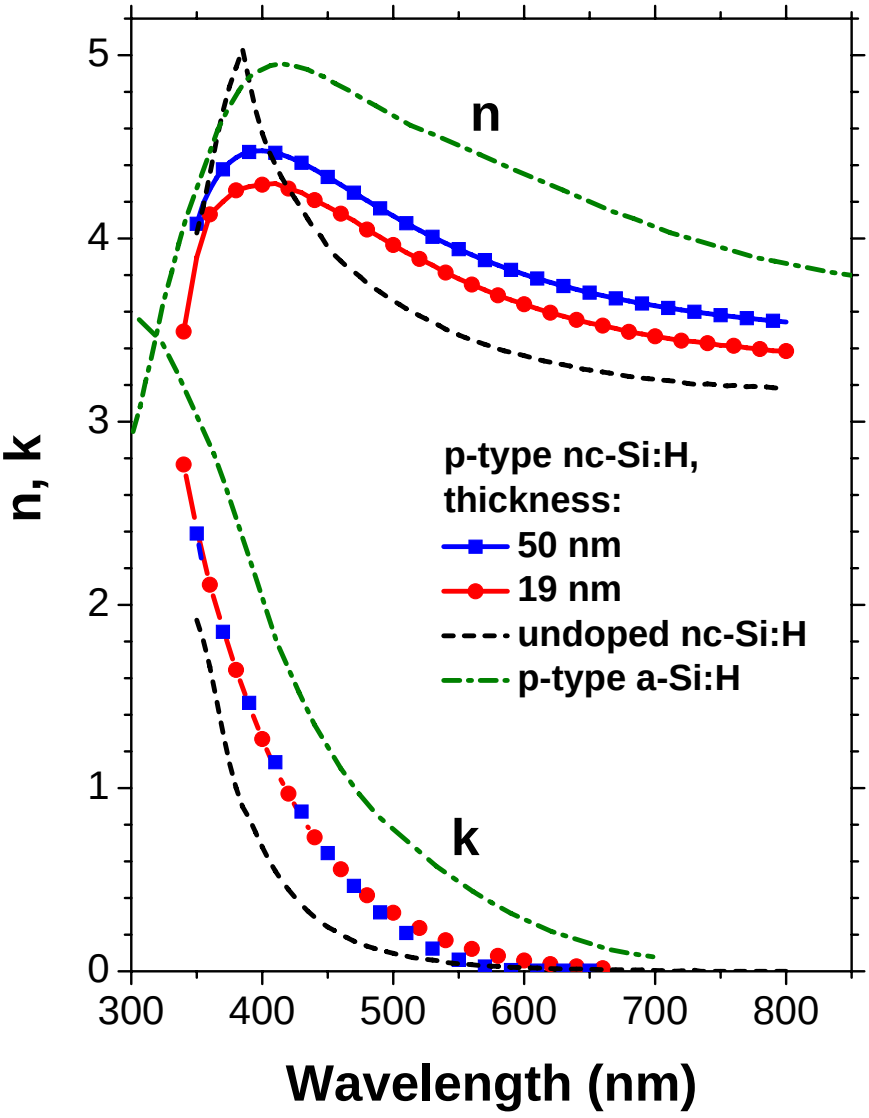

Figure 3.8: Refractive index and extinction coefficient as a function of wavelength obtained from the transmission and reflection spectra of the B-doped and undoped nc-Si:H, and a-SiC:H films.

The function parameters, determined through a fitting procedure for all nc-Si:H sam-

Table 3.1: Overview of the deposition conditions for single layers

Sample	d(nm)	$X_C(\%)$	n_∞	a	γ	$p_v(\%)$
Undoped	38	81	3.09	0.034	4.08	16.5
Doped	19	39	3.23	0.069	3.47	16.4
Doped	50	45	3.35	0.076	3.38	11.1

ples, are shown in Table 3.1. We note that for the highly crystalline (X_c = 81%) undoped nc-Si:H film the value n_∞ of 3.09 is smaller than that (n_c= 3.42) of crystalline Si. Here n_∞ is a measure of the density of the material [53], and therefore, the observed discrepancy indicates the presence of voids in the film. To further analyze the optical data, we consider nc-Si:H as a triphasic material (amorphous + crystalline + voids). According to Bruggemans effective media approximation, the following equation is valid for a film composed of three constituents of volume fractions p_c (crystalline Si), p_a (a-Si:H) and p_v (voids filled with air) [54]:

$$p_a \frac{n_a^2 - n_\infty^2}{n_a^2 + 2n_\infty^2} + p_c \frac{n_c^2 - n_\infty^2}{n_c^+ 2n_\infty^2} + p_v \frac{1 - n_\infty^2}{1 + 2n_\infty^2} = 0 \tag{3.2}$$

while $p_c + p_a + p_v = 1$ and $X_c = p_c/(p_c + p_a)$. The volume fractions are calculated by considering $n_a = 3.8$ (void-free a-Si:H) [55], $n_c = 3.42$ [54], and deduced X_c values from the Raman spectra. The deduced p_v values for all nc-Si:H films are reported in Table 3.1. For the undoped material, the degree of porosity is consistent with that reported in the literature for PECVD nc-Si:H grown at similar deposition conditions [54]. For the doped samples, the thinner layer is less denser than the thicker one due to the more intensive formation of voids at the initial stage of the film growth.

3.4 n-doped nanocrystalline silicon

For n-doped films, Phosphine (PH_3) gas diluted in hydrogen to concentration of 1%, is used as the doping gas. A set of films with different PH_3-to-SiH_4 flow ratios in the range of 0.5%-2% are deposited while keeping the film thicknesses at about

40 nm. Figure 3.9 shows the crystallinity and dark conductivity of the n-doped films deposited on glass substrates. The crystallinities are extracted from Raman measurements similar to those of p-doped series. These measurements show that the n-doped films undergo a gradual phase transition from nanocrystalline to amorphous for [PH_3] / [SiH_4] above 1.3%. As Figure 3.4 shows, similar behavior is observed in Raman spectra of the p-doped films with different TMB-to-silane ratios. Figure 3.9 also shows the dark conductivity of nc-Si:H films as a function of [PH_3] / [SiH_4] flow ratio. The film conductivity increases with increasing doping ratio, reaches a value of $\sim$ 0.5 S/cm at about 0.75%, and then gradually decreases down to 0.025 S/cm at 2%. The conductivity reduction is related to an amorphization of the film structure observed in the series of Raman spectra. Comparing the maximum conductivities obtained for n- and p-doped samples, we observe that, the dark conductivity of the n-doped film is about one order of magnitude higher than that of the p-doped layer. This higher conductivity in n-doped material is attributed to the lower activation energy E_A of $\sim$25.5 meV for the phosphorus doped material compared to $\sim$45 meV for the boron doped material [56]. Activation energy is a good approximation of the position of the Fermi level in amorphous and microcrystalline silicon films and it is measured from [1]:

$$\sigma_d(T) = \sigma_0 \exp -E_A/kT \tag{3.3}$$

where σ_0 is a conductivity factor, T the temperature and k Boltzmann's constant.

3.5 undoped protocrystalline silicon

As it is mentioned before, the phase transition from a-Si:H to μc-Si:H identifies the optimum absorber layer structure. The formation of this high quality absorber layer relies strongly on the analysis of the effect of the hydrogen-to-silane flow rates ratios ([H_2] / [SiH_4]) on the optoelectronic properties of these layers. Measuring dark and photo conductivities is a standard way to obtain information about the quality of this material for applications in photovoltaics. Photosensitivity defined as the ratio

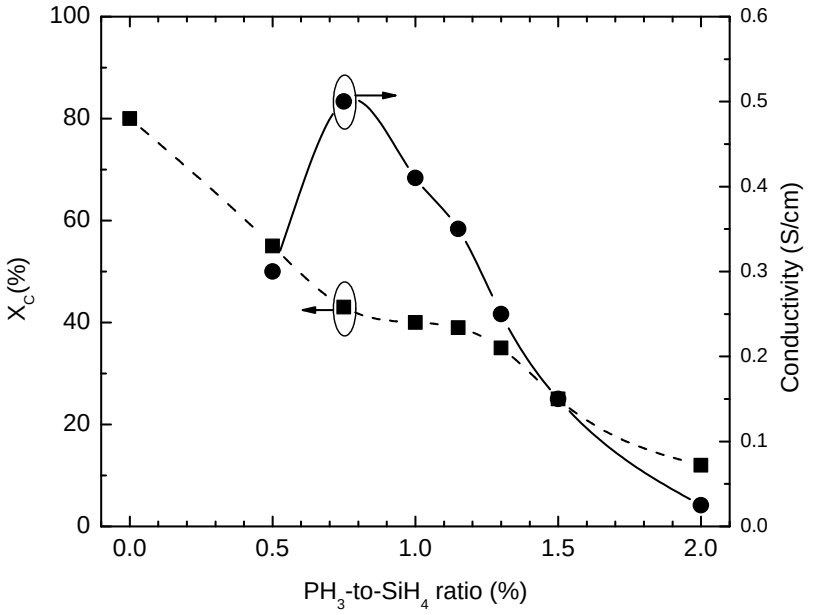

Figure 3.9: Crystallinity and conductivity of 40 nm thick nc-Si:H films as a function of PH_3-to-SiH_4 flow ratio.

of the photo conductivity to dark conductivity is a parameter that can be used to approximate a-Si:H to μc-Si:H phase transition [23].

In order to find the optimum i-layer for our solar cells, undoped silicon films are deposited by varying hydrogen-to-silane ratios from 3 to 5 while kipping the RF power density and deposition pressure constant at 9 mW/cm^2 and 900 mTorr for all depositions. To eliminate the effect of the film thickness on the material structure, all layers are deposited with the same thickness of 300 nm. Photoconductivity is determined by illuminating samples with the standard AM 1.5 light spectrum.

Figure 3.10 shows the photosensitivity σ_{photo} / σ_{dark} of the undoped films as a function of the hydrogen-to-silane ratio. One can see that the photosensitivity reaches a maximum of 1.5×10^6 at the hydrogen-to-silane ratio of 4.54. This point indicates the amorphous-to-microcrystalline phase transition. The obtained photosensitivity value is comparable with the state-of-the-art absorber layer requirement ($> 10^5$) [1]. In general, the value of hydrogen-to-silane ratio is very sensitive to the special geometry and conditions of the plasma chamber so, it slightly changes for different

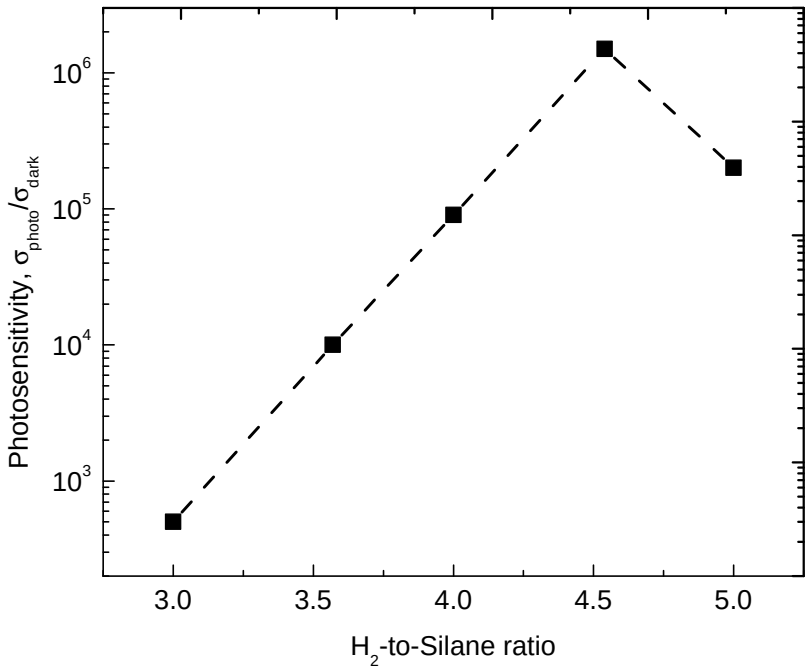

Figure 3.10: Photosensitivity of undoped a-Si:H films versus the hydrogen-to-silane ratios.

plasma systems.

3.6 p-i-n solar cells on glass and PEN

Using optimized doped and undoped silicon layers, single junction p-i-n solar cells are fabricated on Corning Eagle 2000 and Teonex PEN substrates. Table 3.2 summarizes the details of the deposition conditions. The fabricated cells consists of Corning Eagle 2000 glass (or PEN) substrate / sputtered-ZnO (700 nm) / nc-Si p-layer (25 nm) / a-Si:H (340 nm) / nc-Si n-layer (30 nm) / Al. 200 nm thick sputtered Al films are defined different cells with areas of 0.5 and 1 cm^2 on 3" round substrates. Figure 3.11 shows the photograph of fabricated cells on a PEN substrate.

Figure 3.12 shows the current-voltage characteristics of the fabricated pin cells both on PEN and glass substrates. p-i-n silicon layers are deposited on 700 nm thick ZnO:Al layers and there is no light trapping or antireflection coating applied

Table 3.2: Deposition conditions for cell fabrications. The plasma power density P, deposition partial pressure p, and substrate temperature T_{sub} are kept constant while R=[H_2] / [SiH_4], R_{PH_3}=[PH_3] / [SiH_4] and R_{TMB}=[TMB] / [SiH_4] gas ratios vary.

Layer	T_{sub} (° C)	p (mTorr)	P (mW/cm^2)	R	R_{TMB} (%)	R_{PH_3} (%)
i-layer	135	900	9	4.54	-	-
p-layer	135	900	9	100	1	-
n-layer	135	900	9	133.3	-	0.75

to the fabricated cells. The fabricated solar cells on glass and PEN substrates show short-circuit current densities of 9.84 and 8.40 mA/cm^2, open-circuit voltages of 774 and 773 mV, fill factors of 61.73% and 61.50%, and efficiencies of 4.7% and 3.99%, respectively. The achieved device performance is lower than that of the state-of-the-art a-Si:H p-i-n solar cells. This lower performance is believed to be due to the recombination losses at the heterojunction p-i interface. While V_{oc} and FF of both cells are identical, the higher short circuit current density of the cell fabricated on glass results in a higher efficiency of 4.7% compared to that of the cell fabricated on PEN (3.99%).

Figure 3.13 shows the transmittance spectra of the employed PEN and glass substrates. One can see that both substrates have almost the same transmittance for the wavelengths above 400 nm. Most of the photons with wavelengths below 400 nm are either absorbed in ZnO or p-doped nc-Si layer. As a result, the intensity of the light that reaches the intrinsic layer is the same for PEN and glass substrates. Therefore, the lower short circuit current density of the cells fabricated on PEN substrate are attributed to the reduced absorption and/or transport properties of the undoped layer.

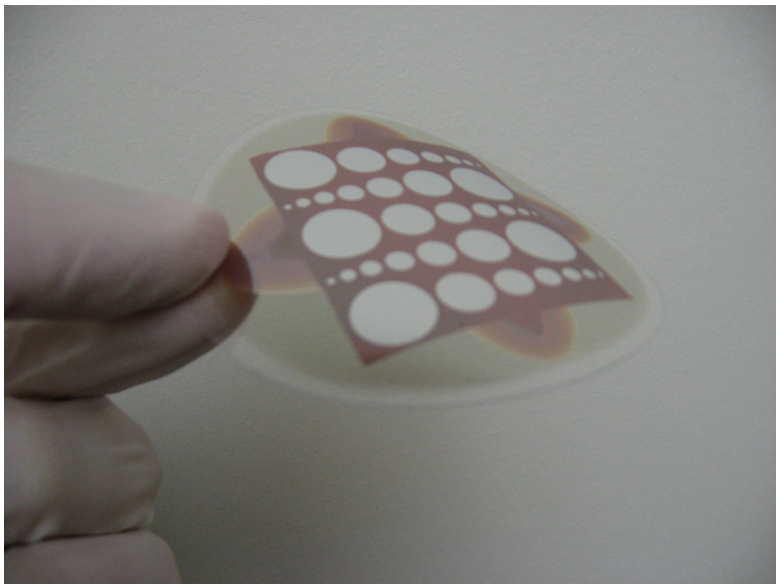

Figure 3.11: Photograph of the fabricated cells on a PEN substrate.

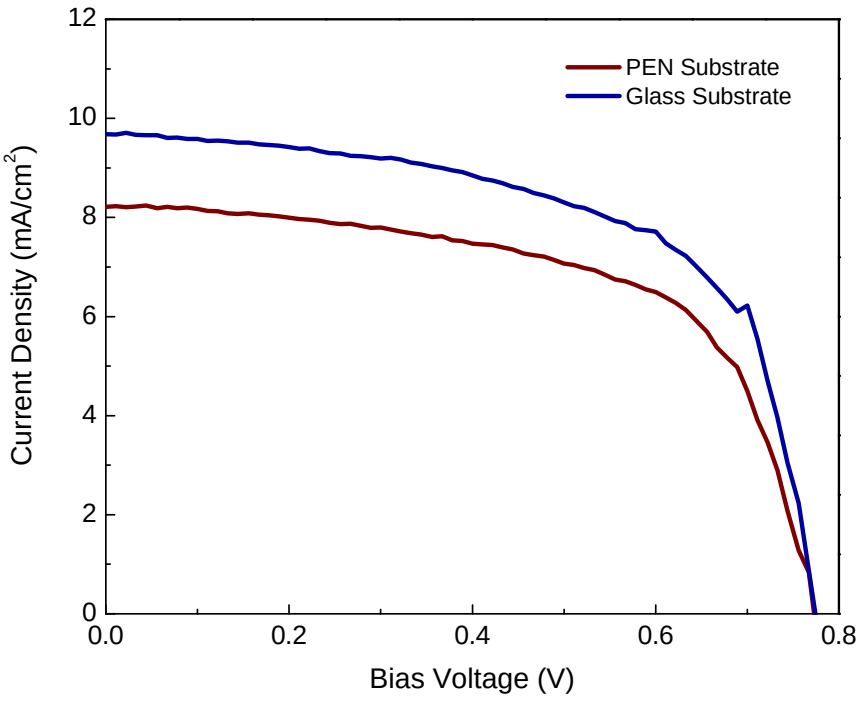

Figure 3.12: Current-voltage characteristics of p-i-n single junction cells under 1.5 AM illumination fabricated on glass and PEN substrates.

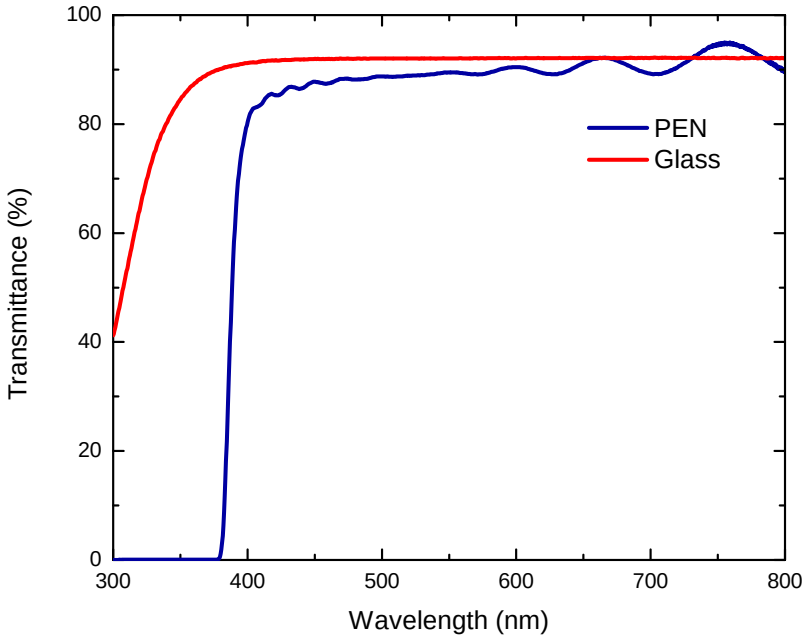

Figure 3.13: Optical transmittance spectra of bare PEN and glass substrates in the wavelength range of 300-800 nm.

3.7 Summary

In this chapter, we studied the optimization of doped and undoped silicon layers of a-Si based solar cells at a low substrate temperature of 135 °C. Individual layers are deposited on bare glass substrates and optimized based on their applications in thin film silicon solar cells.

For p-doped layers, the influence of boron doping and layer thickness on the structural and electronic properties of nc-Si:H films grown by PECVD has been systematically studied. The film crystallinity and conductivity are found to be tailored by controlling the TMB-to-SiH_4 ratio. For 60 nm thick films, the conductivity of 0.07 S/cm is achieved at a doping ratio of 1%. It is also found that conductivity of the thin (25 nm) film was limited by a charge carrier transport through an a-Si:H network, while in the thicker layers, the observed conductivity enhancement is ascribed to the formation of a percolation cluster composed of Si nanocrystallites.

n-doped films are obtained by adding PH_3 gas to the PECVD process of undoped

nanocrystalline deposition. Similar to the p-doped films, crystallinity and conductivity of n-doped films are controlled by the PH_3-to-SiH_4 flow ratios. For 40 nm thick films, the conductivity of 0.5 S/cm was achieved at a doping ratio of 0.75%. This conductivity is about one order of magnitude higher that that of optimized p-dope films. This higher conductivity is attributed to the lower activation energy of the phosphorous doped films.

Undoped silicon films for applications as the solar cell's i-layer are studied in terms of their photosensitivities. We observe that by varying the hydrogen content of the deposited films, the photosensitivity is changed by about four orders of magnitude with a peak at the hydrogen dilution of 4.54. This hydrogen dilution results in a film right at the amorphous to microcrystalline phase transition with favorable properties as the absorber layer of thin film silicon solar cells.

The optimized process conditions are used to fabricate solar cells on glass and PEN substrates. The efficiencies of 4.7% and 3.99% are achieved for glass and PEN substrates, respectively. The lower efficiency of the cells fabricated on the PEN substrate is attributed to the reduced absorption and/or transport properties of the undoped layers.

Chapter 4

Layer Integration and Device Fabrication: Results and Discussion

4.1 Introduction

In the previous chapter, individual silicon layers of a p-i-n structure were deposited and optimized on bare glass substrates. In a complete solar cell structure, these layers are deposited on materials with different structural properties than glass substrates. In this chapter, we re-evaluate our optimization procedure for these layers when they are integrated in complete single junction solar cells. This chapter starts by studying the effect of hydrogen dilution ratio of the i-layer on the overall performance of single junction solar cells. As it was mentioned before, the optimum material structure for the undoped absorber layer is the material right at the amorphous to microcrystalline phase transition. This phase transition is very sensitive to the nature of the underlying material. In our proposed p-i-n structure, the absorber layer is deposited on p-doped layers with nanocrystalline structures [1]. So, it is essential to

[1] At this point, we assume that depositing this nanocrystalline p-doped layer on front ZnO:Al layer would result in the same film structure as the one deposited on bare glass substrates.

re-examine the quality of these undoped layers when they are in the complete p-i-n structure. In this chapter, single junction solar cells with the same i-layer thickness but varying hydrogen dilution ratios from 2 to 40 are fabricated on 0.5 mm thick 3" Corning Eagle 2000 glass wafers. The structure of these solar cells consist of Corning Eagle 2000 glass substrate / sputtered-ZnO (700 nm) / nc-Si p-layer (25 nm) / a-Si:H (300 nm) / nc-Si n-layer (30 nm) / Al. Sputtered Al films of approximately 200 nm thick defined different cells with areas of 0.5 and 1 cm^2 on the substrates. Process pressure of 900 mTorr, RF power density of 9 mW/cm^2 and the substrate temperature of 135 °C are maintained throughout every film deposition. n- and p-doped layers are deposited using the optimized process conditions presented in Chapter 3. Reported cell characteristics (V_{oc}, J_{sc}, FF and efficiency) are average values of 10 different cells with areas of 0.5 and 1 cm^2, all fabricated on a single substrate. This set of devices show lower efficiency values compared to the cell efficiencies reported in Chapter 3. This lower efficiencies are finally attributed to the unfavorable chamber conditions in the specific period of time when these experiments were performed. After cleaning and treating the deposition chambers, efficiency values, as high as the ones reported in the previous chapter were achieved. In this part of the research, the relative values of cell characteristics are analyzed and the absolute values are not used from any conclusions.

In this chapter, we also investigate the structural properties of p-doped nanocrystalline films (developed in Chapter 3) when they are deposited on ZnO:Al layers. We use Raman spectroscopy measurements to study the crystallinity of these layers.

Finally, to improve the performance of our solar cells we introduce amorphous silicon carbide buffer layers between the nc-Si:H p-layer and the undoped protocrystalline absorber layer. This a-SiC:H buffer layer effectively increases the electric field in the i-layer close to the p/i interface by which the separation of the photogenerated carriers at this point is enhanced. This enhancement considerably increases the open-circuit voltage of the fabricated cells.

Schematic structures of different fabricated cells are presented in Figure 4.1.

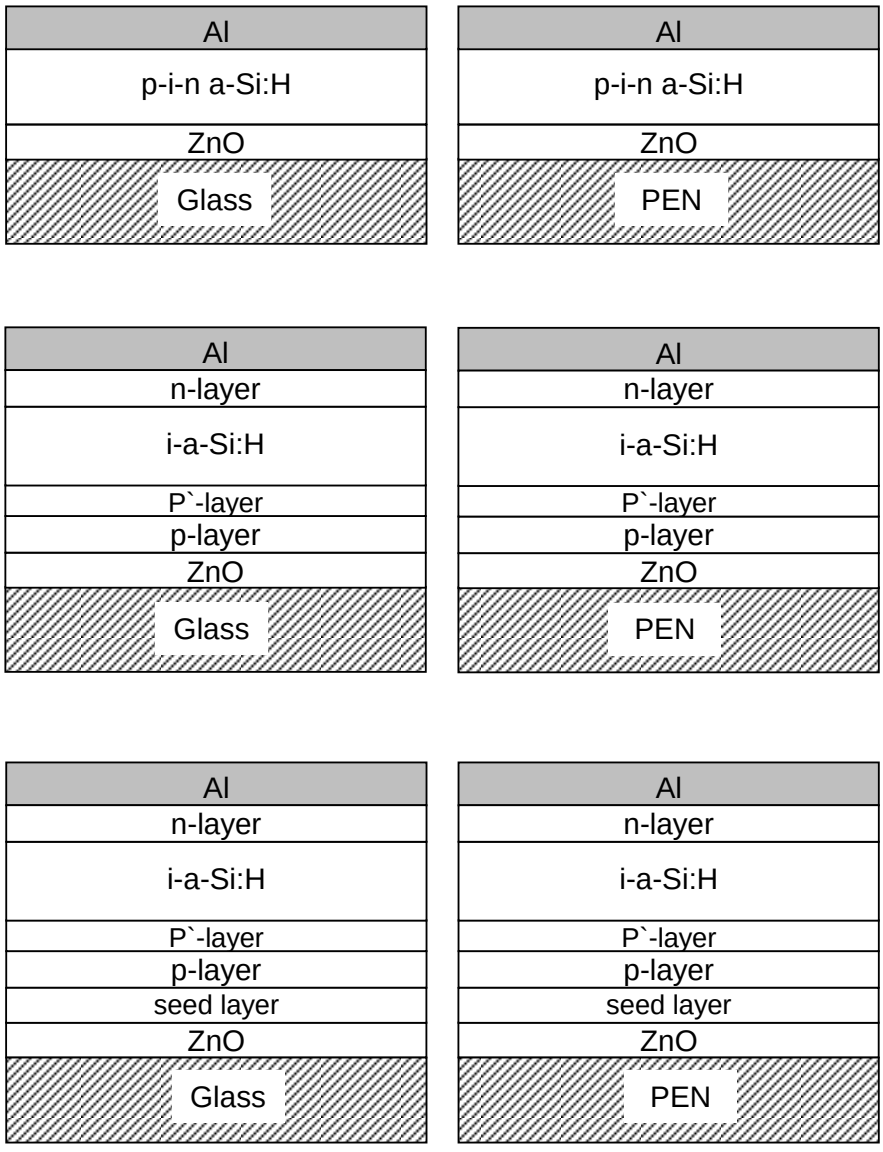

Figure 4.1: Schematic structures of different solar cells fabricated in this chapter.

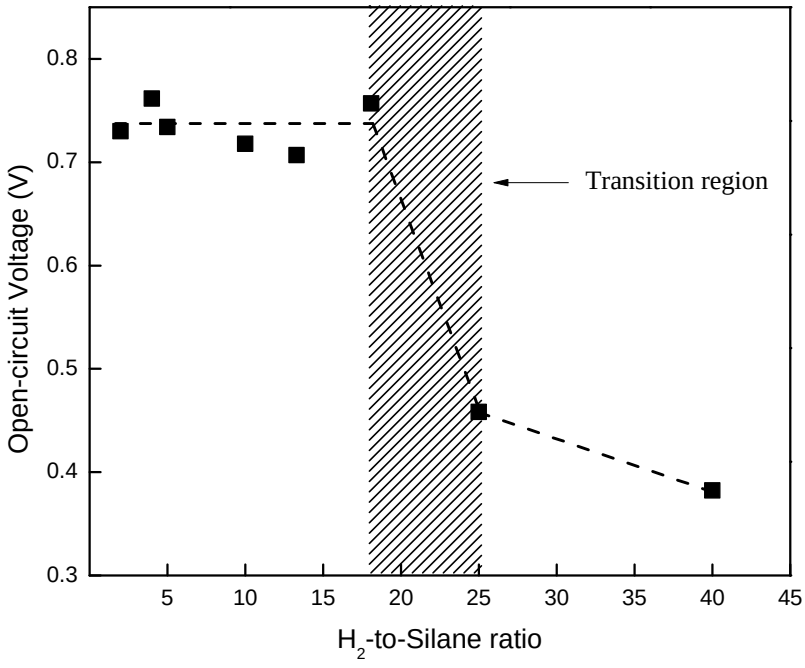

Figure 4.2: Open-circuit voltage of p-i-n solar cells as a function of the hydrogen dilution ratio of i-layer.

4.2 Integrated i-layer optimization

Figure 4.2 shows the open-circuit voltage of the solar cells as a function of i-layer hydrogen dilution ratio. This figure shows that for hydrogen dilution ratios less than 20 the open-circuit voltage does not change widely and shows an average value of 0.75 V. However, as the hydrogen dilution ratio increases beyond 20, the open-circuit voltage abruptly drops to 0.45 V. By further increasing the hydrogen dilution ratio, V_{oc} gradually continues its declining. The sudden drop of open-circuit voltage can only be explained by the energy band gap alteration of i-layer in the p-i-n structure. As it has been shown by [57], at a certain hydrogen dilution ratio the material undergoes a phase change from amorphous to microcrystalline. In a microcrystalline material, the microstructure consists of nanocrystals embedded in an amorphous tissue. These nanocrystals are separated by amorphous silicon, grain boundaries and/or cracks. As we increase the hydrogen dilution ratio these nanocrystals grow to elongated nanocrystals, separated by cracks. At this stage material has a high density

of grain boundaries that act as recombination centers . Gradual deterioration of the open circuit voltage for hydrogen dilution ratios above 20 results from the recombination losses at these poorly passivated grain boundaries [58]. In addition, as the nanocrystals start to grow, nonuniformity of the material structure increases compared to the structure with isolated nanocrystals embedded inside the amorphous silicon. Consequently, the built-in electric field is not spread uniformly throughout i-layer which causes a decrease in open circuit voltage [58], [1].

Figure 4.3 shows the short circuit current density of the fabricated solar cells as a function of i-layer hydrogen dilution ratio. As it can be seen from this figure, short circuit current density decreases for the hydrogen dilution ratios above 10 and then going up again for ratios above 25. As mentioned before, by increasing the hydrogen dilution ratio, the material becomes more microcrystalline. As a result, due to the higher recombination losses at the grain boundaries, the current density decreases. In this case, the optical absorption characteristic of the material changes as the film structure undergoes this phase shift. It has been shown that the absorption coefficient of the microcrystalline film is much higher than that of amorphous silicon for wavelengths above 730 nm [1]. Consequently, we expect that due to the increasing photon absorption in the red and infrared section of the spectrum, the current density increases for i-layers with high crystallinity. Here, this happens for the hydrogen dilution ratios above 25. Figure 4.4 represents the external quantum efficiencies of three solar cells with different i-layer hydrogen dilution ratios measured under the short circuit condition. Clearly, we can see that as the hydrogen dilution ratio increases and the film becomes more crystalline, the photon absorption increases for the wavelengths above 700 nm. As a result, the short circuit current density preserves its high values as the hydrogen dilution ratio increases.

Figure 4.5 shows the distribution of the fill factors of the solar cells as a function of hydrogen dilution ratios. The measured fill factors ranges from 53 to 58 for the cells with different hydrogen dilution ratios. The measured FFs do not show any specific trend as the hydrogen dilution ratio increases. We believe that, this nearly constant

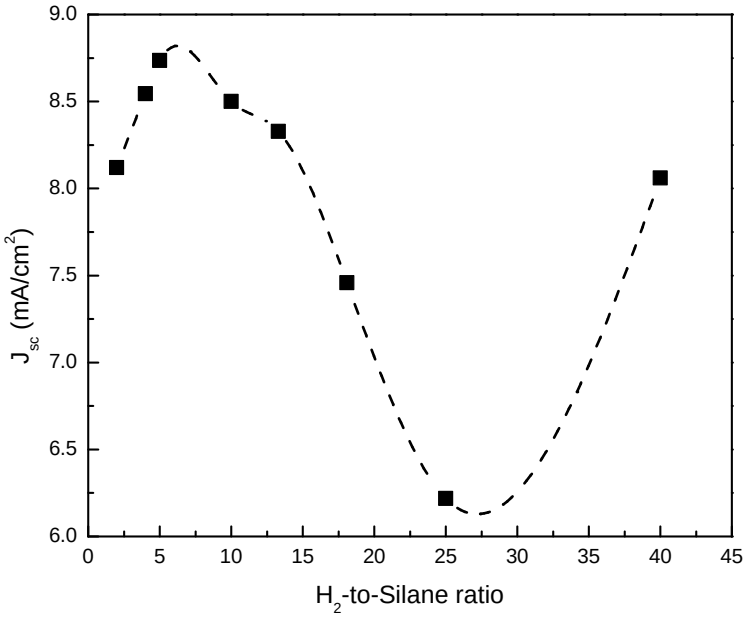

Figure 4.3: Short-circuit current of p-i-n solar cells as a function of the hydrogen dilution ratio of i-layer.

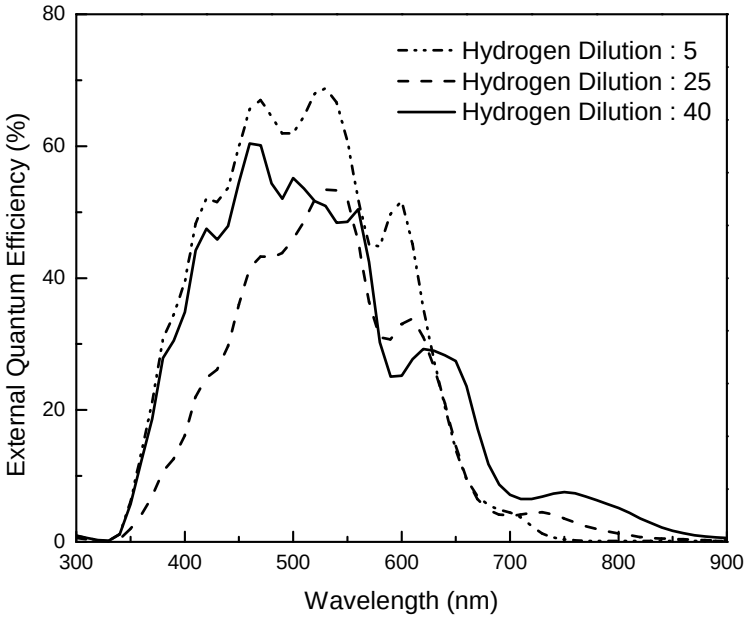

Figure 4.4: External quantum efficiency of the cells with different hydrogen dilution ratios. This EQE measurement has been done under the short-circuit condition.

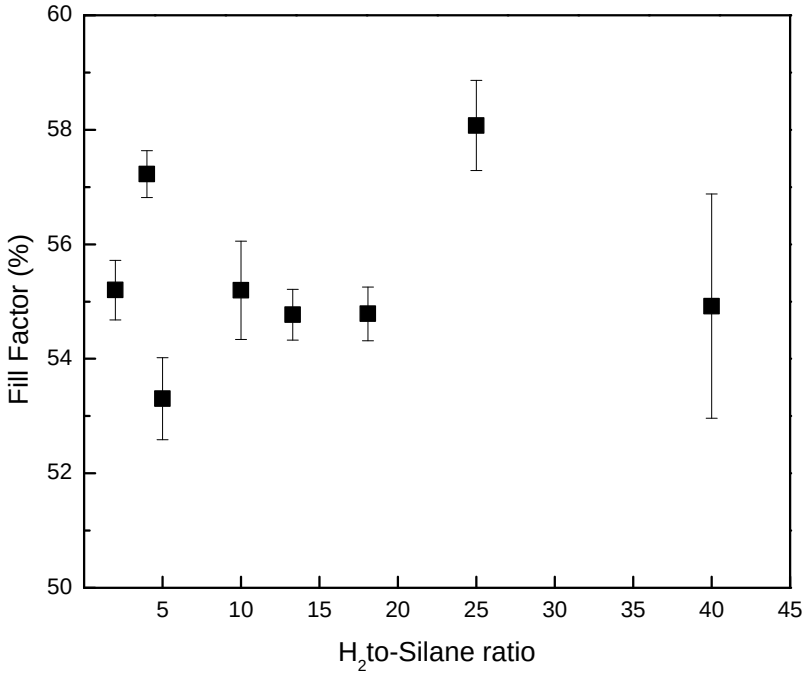

Figure 4.5: Fill factor of the fabricated cells as a function of i-layer hydrogen dilution ratio.

FF values are the consequence of using the same deposition conditions for the p- and n-doped layers. In this case, the shunt and series resistance (and so the FF) values of the fabricated cells do not change significantly as we vary the deposition conditions of the i-layer. The efficiency of the fabricated cells as a function of i-layer hydrogen dilution is shown in Figure 4.6. As we expect from V_{oc} and J_{sc} measurements, the combination of the highest short circuit current density and the highest open circuit voltage is obtained near i-layer phase transition from amorphous to microcrystalline. The dependence of the efficiency on the hydrogen dilution, clearly proves that the optimized protocrystalline silicon material offers the best undoped absorber layer properties for p-i-n cells at the low deposition temperatures.

As it is mentioned in the introduction section of this chapter, along with the hydrogen dilution ratio, substrates can also play critical roles in tunning the i-layer microstructure. According to [23], nanocrystalline p-doped layers facilitate the nucleation of microcrystals in the growing films. Referring to the Figure 4.6, the highest

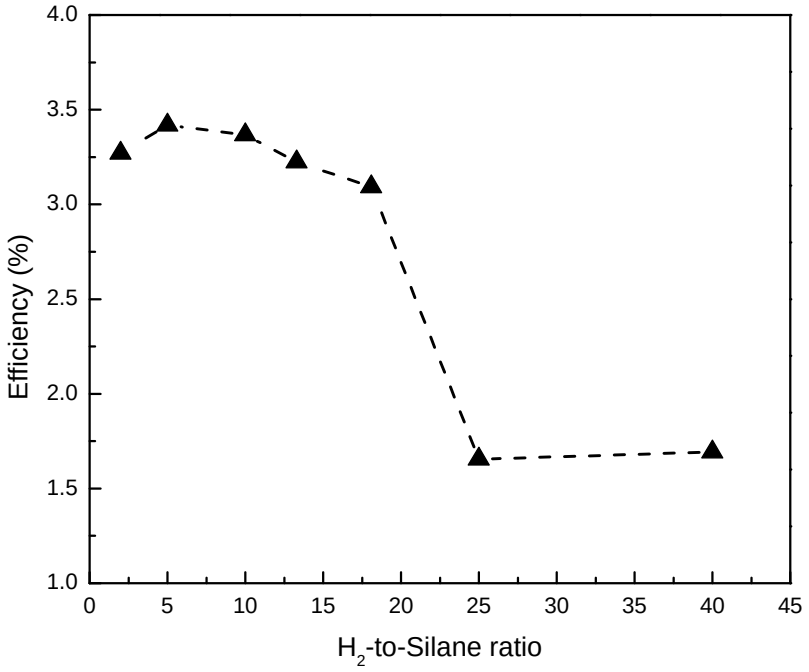

Figure 4.6: Efficiency of the fabricated cells as a function of i-layer hydrogen dilution ratio.

conversion efficiency is achieved for the cell with i-layer hydrogen dilution ratio around 5. This hydrogen dilution ratio is the same as the one obtained for the undoped layers, deposited and optimized on the glass substrates (see Chapter 3). This similarity questions the validity of the crystalline structure of our p-doped layers deposited on the front Al-doped ZnO. In the next section, we investigate the structure of our optimized p-doped layer when it is deposited on the Al-doped ZnO films.

4.3 Integrated doped layers optimization

4.3.1 Nanocrystalline p-dope layer on ZnO:Al coated glass

In the previous section, our measurements suggested that the p-doped layer deposited on ZnO:Al coated glass has amorphous structure thereby invalidate our initial assumption of the nanocrystallinity of these p-doped layers. To examine this point, we

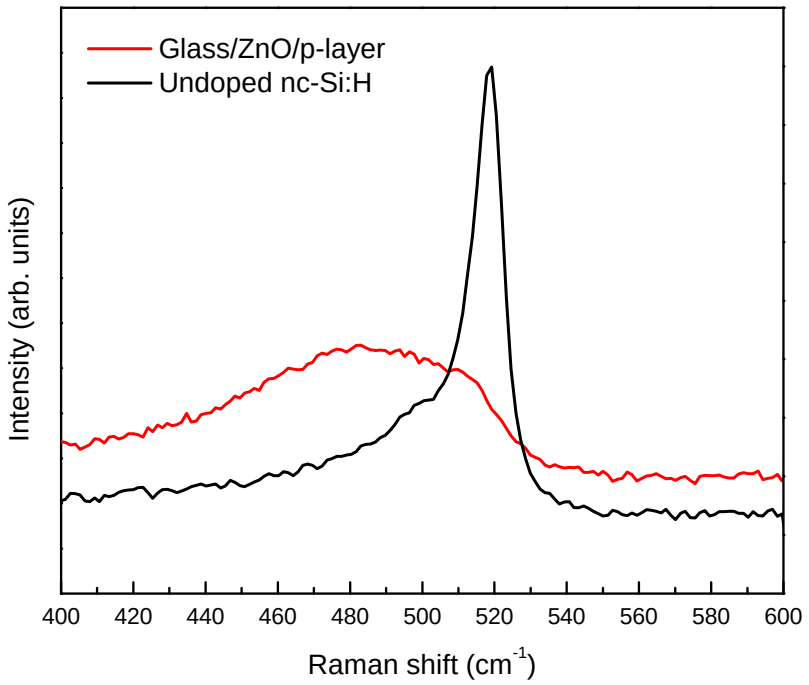

Figure 4.7: Raman spectrum of thin (∼20 nm) p-doped a-Si:H deposited on glass with the ZnO:Al coating and a nc-Si:H film for comparison.

deposit a thin (∼20 nm) layer of p-doped silicon layer on a ZnO:Al coated glass substrate and we use Raman spectroscopy to evaluate the structure of this film. Figure 4.7 shows the Raman spectra of this film and a nc-Si:H for comparison. This figure clearly confirms the amorphous structure of the p-doped layer deposited on ZnO:Al coated glass. This technological issue can be resolved by controlling the initial development of crystalline nuclei. Vetterl et. al have proposed seed-layer preparation technique, which is based on the slow decrease of hydrogen-dilution during the deposition process [59]. We have developed an alternative method to avoid changing the gas flow during the deposition. A 3-5 nm thick seed layer is prepared using a SiH_4 + H_2 + PH_3 gas mixture at the deposition conditions reported for n-type nc-Si:H. PH_3 is used here to promote the formation of crystalline nuclei. Raman spectrum of the glass/ZnO:Al/seed-layer/p+ nc-Si:H structure is shown in Figure 4.8. A deduced X_c value of 45.4% is similar to that for the films grown on glass substrates under the same deposition conditions.

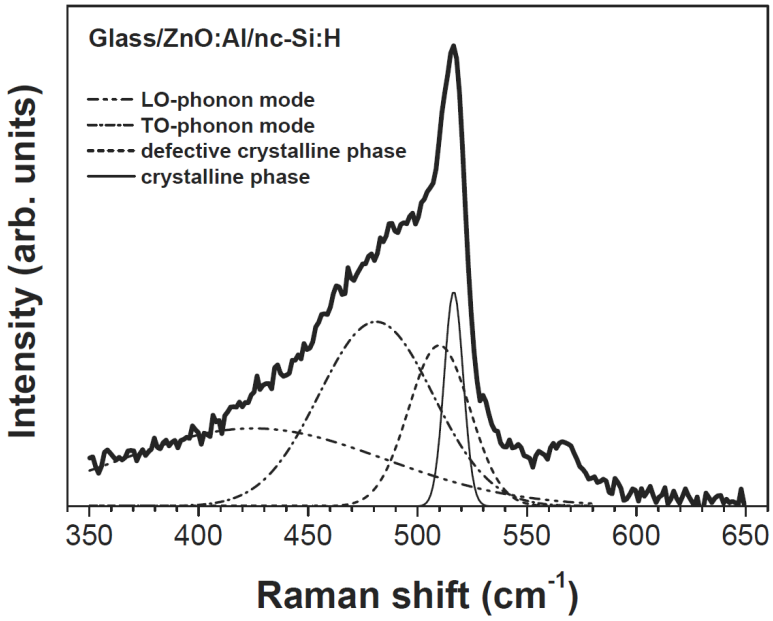

Figure 4.8: Raman spectrum of a thin (∼20 nm) nc-Si:H film deposited on glass with the ZnO:Al coating.

4.3.2 Amorphous silicon carbide buffer layers

According to the previous results on a-Si:H p-i-n photodiodes (developed in G2N Laboratory) with p+ nc-Si:H window layers, low leakage current and enhanced sensitivity in the UV/blue range have been achieved by incorporating a lightly doped a SiC:H buffer (p'-layer) between the p- and i-layers [60]. The role of the buffer layer is also crucial for solar cells. Rath et al. have reported that the p-i-n cells with a nc-Si:H/a-Si:H p-i interface exhibit a poor device performance, moreover, I-V characteristics under illumination have an S-type behavior [61]. This issue can be attributed to the band offsets at the heterojunction p-i interface. Computer simulations point out that in the p-p'-i-n structure, a wide band gap a-SiC:H p'-layer effectively blocks electron back diffusion from the a-Si:H i-layer to the nc-Si:H p-layer with a narrower gap [62]. The band gap of this p'-layer is a subject of optimization.

Three cells are fabricated by the following deposition sequence. First, a ∼700 nm thick transparent conducting film is sputtered in Ar plasma on a 0.5 mm thick

Corning Eagle 2000 glass substrate using a 2 wt. % Al_2O_3 doped ZnO target. The process is carried out at a pressure of 5 mTorr, RF power of 100 W, and a substrate temperature of about 135 °C. Then, a p-nc-Si:H (15 nm) / p'-a-SiC:H (8 nm) / i-a-Si:H (300nm) / n-nc-Si:H (30 nm) film stack is deposited. Finally, a ∼200 nm thick Al film is sputtered through a shadow mask to form the top electrodes with the area of 0.5 and 1 cm^2. nc-Si:H p-layer is deposited at [TMB] / [SiH_4] = 0.5%. The p-type a-SiC:H is deposited using a SiH_4 + H_2 + CH_4 + TMB gas mixture with a hydrogen dilution ratio of 5, and [TMB] / [SiH_4] = 1%. To optimize the band gap of p'-layer, the CH_4-to-SiH_4 flow ratios are 0.7 and 1 (referred below to Sample #1 and #2, respectively). The process pressure and RF power are 600 mTorr and 22 mW/cm^2, respectively. Undoped a-Si:H is deposited using a SiH_4+H_2 gas mixture at a hydrogen dilution ratio of 5. The n-doped nc-Si:H material is deposited using a 1:100:0.015 mixture of SiH_4 / H_2 / PH_3. The process pressure and RF power are 900 mTorr and 9 mW/cm^2, respectively. A p-i-n cell (Sample #3) with a 20 nm thick a-SiC:H p-layer is prepared using the same experimental conditions for the i- and n-layers. The p-layer is deposited at [CH_4] / [SiH_4] = 0.7 keeping other parameters at the same values as those reported above. Figure 4.9 shows the typical current-voltage characteristics of our cells under AM1.5 illumination. Samples #1 and #2 are p-p'-i-n structures, where the optical gaps (E_{04}) of a-SiC:H p'-layers are 2.07 and 2.18 eV, respectively. Sample #3 is a p-i-n cell with an a- SiC:H p-layer (E_{04} = 2.07 eV). Device parameters are reported in Table 4.1. Sample #1 shows the best conversion efficiency (η) of 7% due to the increased short circuit current density (I_{sc}) and high fill factor (FF). Sample #2 with a wider band gap of the p'-layer shows the highest open circuit voltage (V_{oc}) of 0.901 V but the values of both I_{sc} and FF are slightly lower than those in Sample #1. Sample #3 shows the lowest conversion efficiency because the lightly doped p-layer limits the fill factor.

Figure 4.10 shows the external quantum efficiency spectra measured under short-circuit conditions without background illumination. The curves look similar and the peak values of the curves vary from 77 to 82% in the narrow spectral interval of 520-540 nm. Sample #1 exhibits a collection efficiency enhancement in the short-

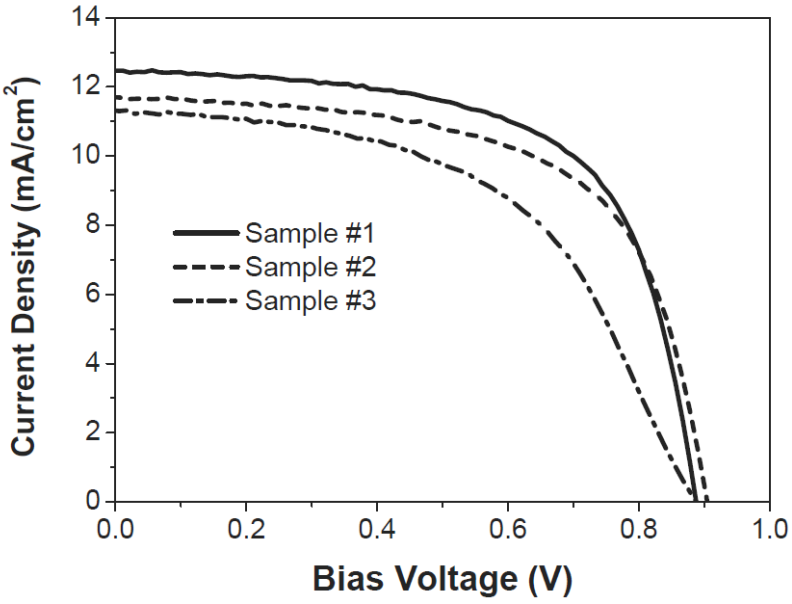

Figure 4.9: Current-voltage characteristics of a-Si:H solar cells under 1.5 AM illumination.

Table 4.1: Optical bandgap of a-SiC:H (E_{04}) and AM1.5 output parameters of solar cells.

CH_4-to-SiH_4	E_{04} (eV)	V_{oc} (V)	I_{sc} (mA)	FF (%)	η(%)
0.7	2.07	0.8875	12.469	63.26	7.00
1	2.18	0.9010	11.690	62.00	6.56
0.7	2.07	0.8876	11.315	52.53	5.28

wavelength range indicating the good quality of the p-p'-i interface. Using the same fabrication parameters (including preheating times), single junction p-i-n solar cells fabricated on a PEN substrate. Table 4.2 presents the average output characteristics of these solar cells.

Table 4.2: AM1.5 output characteristics of the fabricated devices on the PEN substrate.

Substrate	V_{oc} (V)	I_{sc} (mA)	FF (%)	η(%)
PEN	0.879	11.325	61.00	6.07

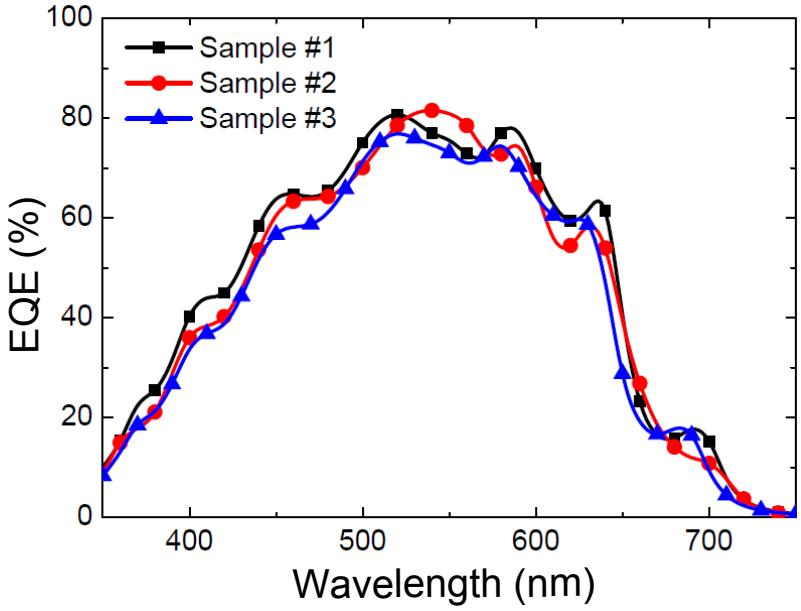

Figure 4.10: External quantum efficiency spectra of a-Si:H solar cells.

4.4 Summary

The influence of the hydrogen dilution of the absorber layer on the output characteristics of a p-i-n solar cell has been systematically studied. For hydrogen dilution ratios above ∼18, the undoped silicon layer structure undergoes a phase transition from amorphous / protocrystalline to microcrystalline. Process conditions near this phase transition result in devices with highest conversion efficiencies [63], [58]. As it is shown by [64], the principle reason for obtaining high values of open-circuit voltage near the a-Si to μc-Si transition is the passivating effect of the amorphous tissue on the grain boundaries and internal surfaces. The short-circuit current density of solar cells strongly depends on the collection of photogenerated charge carriers. So,

as we expect the same trend is observed for the short-circuit current density of solar cells. While in our solar cells, the underlying film for the i-layer is supposed to be nanocrystalline, the optimum hydrogen dilution ratio is the same as the one acquired for i-layer optimization on glass substrates. This is in contradiction with the growth mechanisms of protocrystalline films with the tendency to nucleate faster on substrates with nanocrystalline structures.

To investigate the true structural nature of the p-doped films, they are deposited on ZnO:Al coated glass substrates and Raman spectroscopy is used to deduce the crystallinity of these films. The measurements shows that this film has a very small crystalline fraction and it is almost amorphous. To solve this problem a thin ($\sim$ 3-5 nm) phosphine-doped silicon film is deposited on the ZnO:Al layer. This interlayer facilitates the nucleation process in the subsequent p-doped layer deposition. Raman spectroscopy measurements of this film stack shows a crystallinity of 45.4%.

To improve the open-circuit voltage of p-i-n solar cells, we employs wide bandgap SiC:H films as the buffer layer between the p-doped nc-Si:H and protocrystalline absorber layer. Two samples with p-p'-i-n structure and different optical band gap (2.07 and 2.18) buffer layers are fabricated and characterized. The highest conversion efficiency of 7% is achieved for the cell with an optimized optical gap ($E_{04} = 2.07$ eV) of the a-SiC:H p'-layer.

Chapter 5

Implementation of Light Management: Results and Discussion

5.1 Introduction

Currently, the light management is the most important research area in the field of a-Si based solar cells [1]. At present there are different schemes which are implemented inside the solar cells to capture light in the absorbing layer, and are typically based on the scattering of light at rough interfaces and employment of highly reflective back structures. In this research, we focus on integrating highly reflective back structures in our solar cells to enhance the long wavelength response of the fabricated cells.

In p-i-n a-Si solar cells, the back metallic contact is either silver (Ag) or aluminium (Al); where aluminium is preferred due to its lower price and higher availability. However, within the wavelength range of 600-800 nm, aluminium has a reduced reflectivity due to its interband absorption at $\lambda \approx 800$ nm [33]. Recently photonic crystals and plasmonic back reflectors have garnered attention as highly-effective back structures for thin film silicon solar cells.[34, 35, 36, 37, 38] Although two- or three-dimensional back structures seem promising for efficient light trapping, one-dimensional photonic

crystals known as Distributed Bragg Reflectors (DBRs) are more compatible with large area production technologies. DBR structures also known as 1-D Photonic Crystals (PCs) consist of alternating sequence of layers of two optical materials with different refractive indices (n_1, n_2). The optical thickness of each layer (D_1, D_2) is determined as the one-quarter of the wavelength (λ_0) for which the DBR is designed [65]:

$$D_1 = n_1 d_1 = \lambda_0/4$$

$$D_2 = n_2 d_2 = \lambda_0/4$$

In a DBR structure by increasing the number of periods and/or the refractive index contrast between the two materials, a high reflectance can be achieved for a limited bandwidth around λ_0. In a mid-gap amorphous silicon (a-Si:H) solar cell, most of the incoming photons with wavelengths below 600 are absorbed in the silicon layer and they never reach to the back reflector. However, Red and near-IR photons ($\lambda > 600$ nm) with absorption lengths above 1μm are very difficult to be absorbed in a typical intrinsic layer thickness of 250-300 nm.

In the first part of this chapter we have designed DBR structures for applications as the back reflectors in a-Si solar cells. The optimized DBR structures are fabricated and their optical properties are investigated and compared to those of conventional Al back reflectors. Finally, we experimentally demonstrate the efficiency enhancement of rigid and flexible a-Si solar cells employing DBR back reflectors. All the thin films and solar cells investigated here are fabricated using a conventional multichamber (13.56 MHz) plasma-enhanced vapour deposition (PECVD) system at the substrate temperature of 135 °C. Such a low deposition temperature allows the application of the developed technology to plastic substrates.

Second part of this chapter is dedicated to the application of these DBR structures in the building integrated solar cells. Recently, the market opportunity for semi-transparent thin film solar cells has been rapidly emerged due to the application of these solar cells in building industry [66][67][68]. In these applications, solar panels are employed as the building components, generating electricity and allowing partial

penetration of the daylight into the building. Furthermore, they can recycle part of the building consumed energy by absorbing the interior illuminating lights. Using transparent electrodes results in poor conversion efficiencies (around 3%) in these solar cells [67]. To improve the efficiency, we propose using highly reflective DBRs as the coating back structures in these solar cells. As explained before, without a back reflector, amorphous silicon solar cells are partially transparent for the wavelengths above 600 nm. On the other hand, according to the International Commission on Illumination (CIE, 1978), the human eye sensitivity drops to values as low as 0.2 for the wavelengths above 640 nm [69]. So, for a semi-transparent solar cell, feeding any of these photons back toward the absorber layer has a small effect on the observer perception. In this research, we have investigated two different DBR structures; one consists of hydrogenated amorphous silicon / amorphous silicon nitride (a-Si:H/a-SiN:H) stacks, and the other of a-SiN:H layers with high and low Nitrogen content. In order to study the optical properties of these DBR structures, they are separately designed and fabricated on the glass substrates. Comparing transmittance, reflectance, and absorbance spectra of these test structures helps to define the optimum DBR back reflector for applications in the semi-transparent solar cells. Using the optimum DBR structure, we have fabricated semi-transparent single junction amorphous silicon solar cells on Glass substrates.

5.2 DBR Back Reflectors

The DBR structures considered in this work consist of stacks of a-Si / SiN for maximum reflectance in the wavelength range of $\lambda = 600 - 800$ nm. The refractive indices of the a-Si and SiN layers are extracted using PUMA software[44](based on the measured transmission spectra of single layer films on quartz substrates) and are found to be 3.18 and 1.70, respectively (at $\lambda = 700$ nm). Thus, the thicknesses of the a-Si and SiN layers are determined 55 nm and 103 nm, respectively. The DBR structures are then designed and simulated using a MATLAB code that calculates the reflectivity based on the transfer matrix method; ignoring loss and dispersion for simplicity.

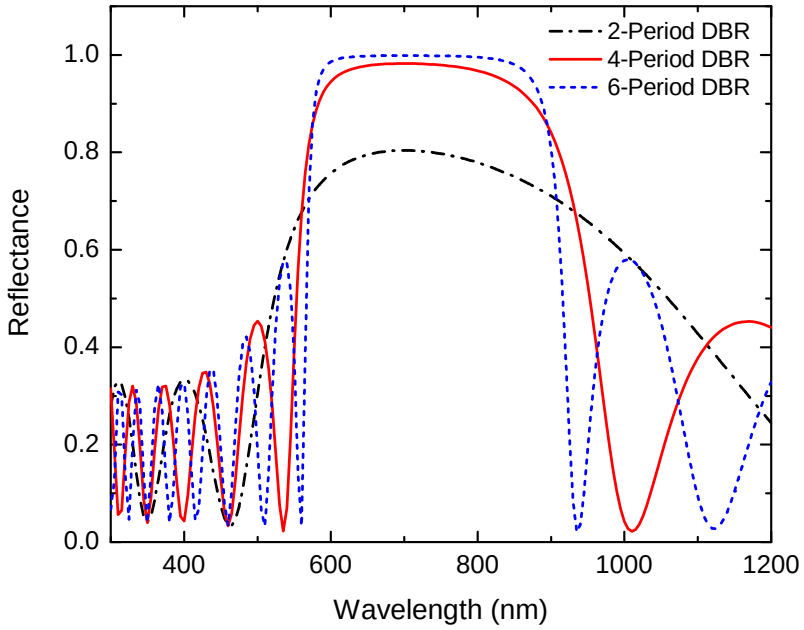

Figure 5.1: Simulated reflectance spectra of two-, four-, and six-period a-Si / SiN DBR structures.

Figure 5.1 shows the simulated reflectance spectra of DBR structures consisting of two-, four-, and six-period of a-Si / SiN stacks with layer thicknesses of 55/103.

As the number of periods increases from two to six, we observe more evident wavelength selectivity and a higher reflectance in the desired wavelength range. However, to reduce the number of fabrication steps, four-period DBR structures with a sufficiently high reflectance of 98% are used in the following experiments. Measured and simulated reflectance of the four-period DBR structure and the measured reflectance of a sputtered Al film are presented in Figure 5.2.

While the Al reflectance gradually decreases from $\sim$ 93% at λ = 500 nm to $\sim$ 87% at $\lambda = 850$ nm, the DBR structure exhibits a wavelength-selective reflectance of $\sim$ 98% for wavelength range of $\lambda = 600 - 800$ nm. Low reflectivity of the DBR structure for wavelengths below 600 nm does not affect the cell performance as the photons with these wavelengths have already been absorbed in 300 nm a-Si absorber layer. As Figure 5.2 shows, using the same values for refractive indices and adjusting a-Si / SiN thicknesses to 51 / 101 result in a reasonable fit for the simulated spectra.

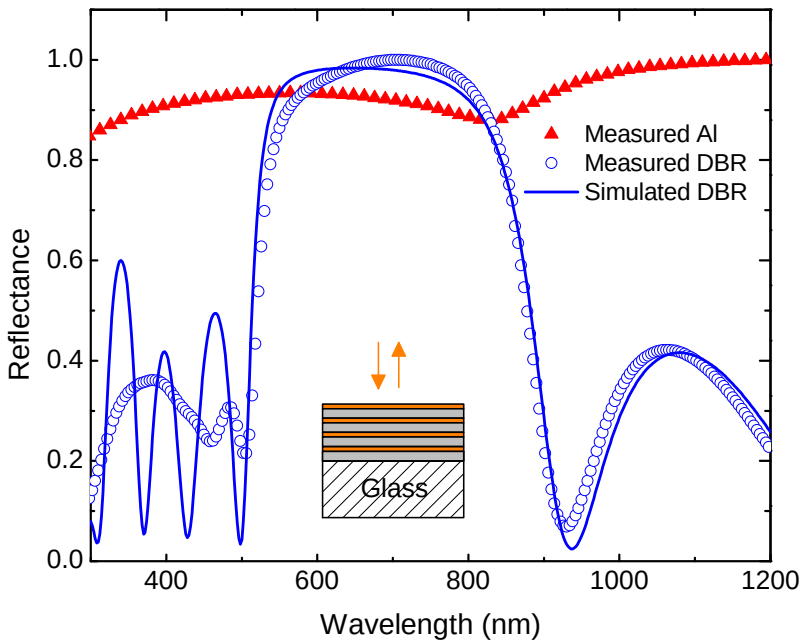

Figure 5.2: Reflectance spectra of Al and a four period a-Si / SiN DBR structure.

This thickness error is due to the process variation and quite tolerable as it does not cause a major drift in DBR reflectance spectra. While the results of Figure 5.2 prove the superior reflectance of the DBR compared to aluminum back-reflector, it must be noted that none of the two structures are appropriate for direct application to a working solar cell. In cells with the DBR back structures, a transparent conductive oxide layer is required to provide the electrical connection to the bottom layer of the device. Thus, we introduce a 600 nm zinc oxide (ZnO) layer to ensure a low sheet resistance for the back electrode. On the other hand, for solar cells with Al back reflectors, a TCO interlayer is inserted to serve as a diffusion barrier and index-matching layer and typically has a thickness of 80-100 nm. To investigate the spectral effect of TCO interlayers, 80 and 600 nm ZnO films are deposited on the Al and DBR structure, respectively. As Figure 5.3 demonstrates, inserting 600 nm TCO layer only leads to the typical spectral interference fringes which are expected from the simulation results. Nonetheless, the average reflectance of Al/ZnO in the wavelength region of $\lambda = 600 - 800$ nm decreases from 91% to 71%.

To investigate the effect of the DBR back reflectors on the performance of a-

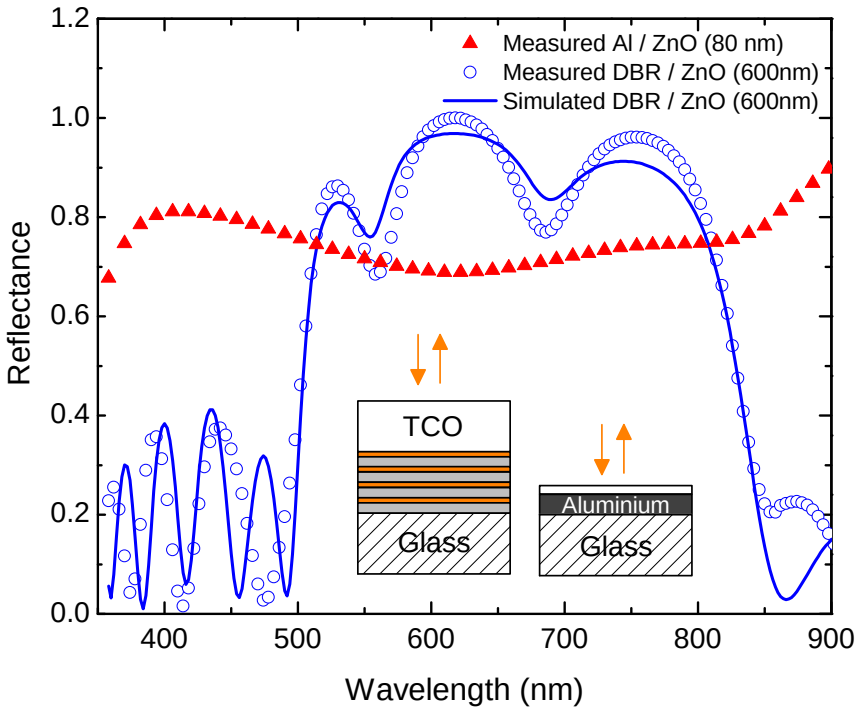

Figure 5.3: Reflectance spectra of the Al / ZnO (80nm) and DBR / ZnO (600 nm) structures.

Si solar cells, single junction solar cells with identical p-i-n structures but different back reflectors are fabricated both on in-house ZnO-coated polyethylene naphthalate (PEN) and Asahi U-type glass substrates. The fabricated cell structures composed of substrate / nano-crystalline (nc) Si p-layer (25 nm) / a-Si (300 nm) / nc-Si n-layer (30 nm) / Back reflector. Cells with 0.5 and 1.0 cm^2 areas are defined by sputtering Al or ZnO (600 nm) contacts through a shadow mask. The external quantum efficiency (EQE) measurements are performed under short-circuit conditions over the wavelength range of $\lambda = 300 - 800$ nm and the $J - V$ characteristics of the solar cells are obtained with a solar simulator under one sun illumination (AM1.5, 100 mW/cm^2). Figure 5.4 illustrates the cross sectional Transmission Electron Microscopy (TEM) image of the cell with DBR back structure fabricated on a glass substrate. The DBR over ZnO interlayer demonstrates a very uniform layer stack of a-Si and SiN with smooth interfaces between the layers. The DBR becomes wavy as a result of the substrate roughness.

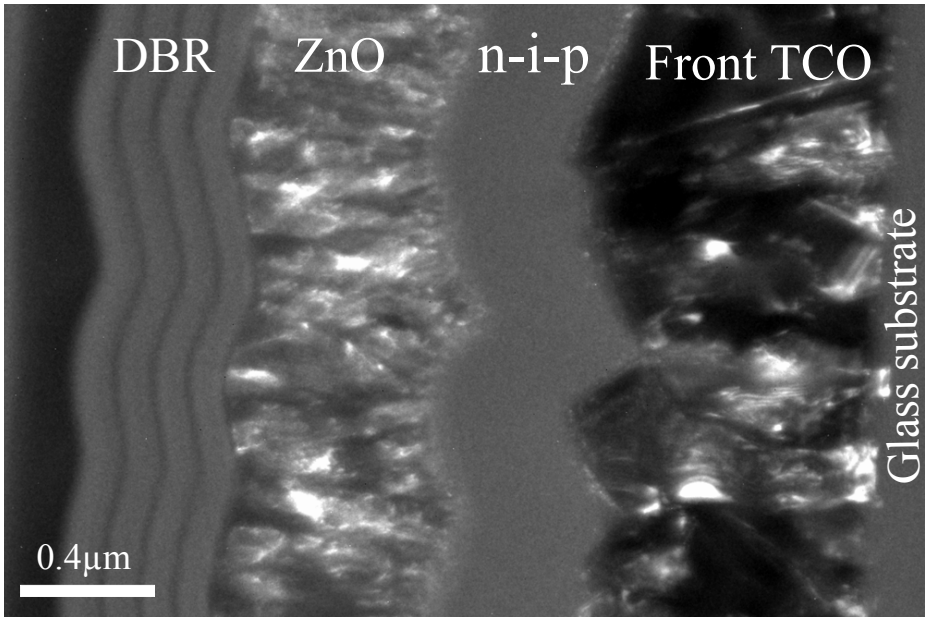

Figure 5.4: TEM micrograph of the cell on glass with DBR back reflector.

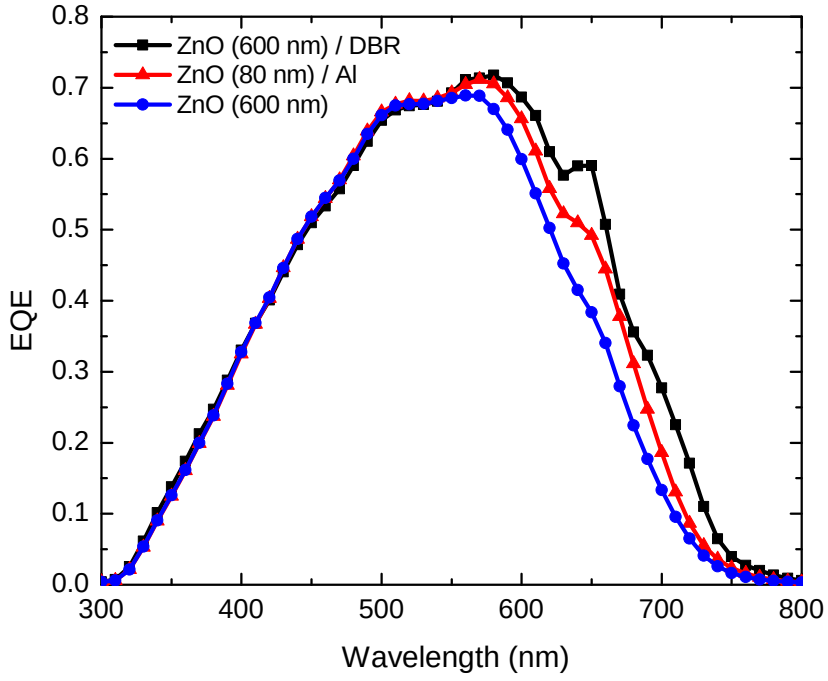

Figure 5.5: External quantum efficiencies of the cells with different back reflectors, fabricated on glass substrates.

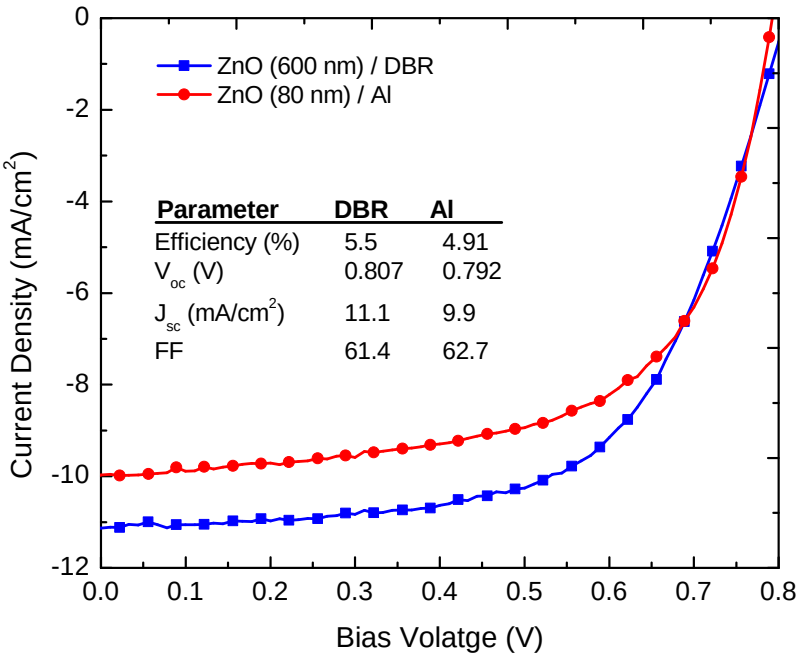

Figure 5.6: The illuminated J-V characteristics of the cells with DBR / ZnO and Al / ZnO back reflectors.

Figure 5.5 shows the EQEs of the cells with different back reflectors and one with no back reflector. While the EQE spectra are identical for short-wavelengths ($\lambda = 300 - 550$ nm), the cell with DBR back reflector reveals the highest EQE in the longer wavelengths exceeding 550 nm, corresponding to enhanced absorption of photons in this region. As a result, the photo-current of the cell with DBR back reflector is expected to increase compared to that with Al back reflector.

The $J - V$ characteristics of the cells with Al and DBR back structures are presented in Figure 5.6 which shows 10% increase in J_{sc} as expected from EQE. Moreover, the open circuit voltage and fill factor values are nearly identical for the two devices. Yet, the cell with DBR back structure shows a slightly larger slope close to the open circuit point (and in the forward bias region) as a result of more resistive back electrode.

Figure 5.7 shows the EQE spectra of the cells fabricated on PEN substrates. Similar to glass substrates, the DBR back reflector improves the photon absorption

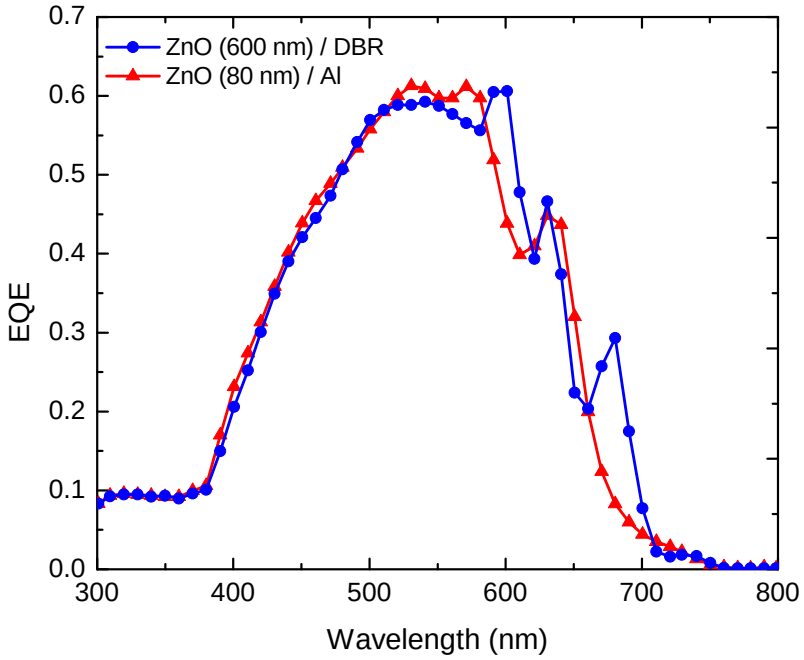

Figure 5.7: External quantum efficiencies of the cells with different back reflectors, fabricated on PEN substrates.

in the wavelength region of $\lambda > 600$ nm. However, the absorption enhancement is only 5% and is not as strong as the one achieved for Asahi U-type glass substrates. This relatively less pronounced enhancement is attributed to the smoothness of the front ZnO layer on the PEN substrate compared to the textured TCO on the Asahi glass. This result reveals the significance of having a rough TCO surface for superior enhancement by the DBRs.

5.3 DBRs for Semi-Transparent Solar Cells

5.3.1 Semi-transparent solar cell optimization

For building integrated applications, solar cells should be semi-transparent for a part of the visible range and highly reflective for the red and infrared red section of the light spectrum. In these solar cells the partial transparency of the device can be controlled

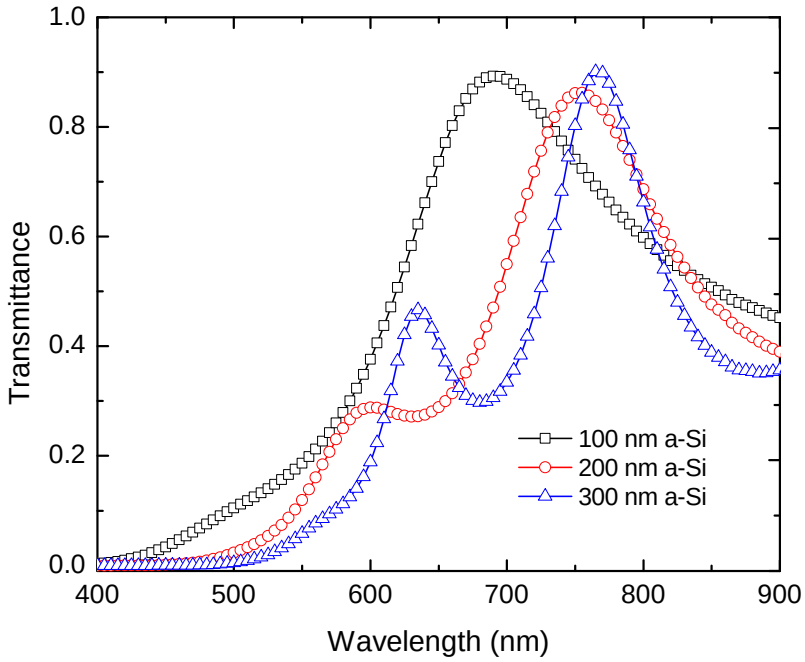

Figure 5.8: Transmittance spectra of 100, 200, and 300 nm thick amorphous silicon films on glass substrates.

by the thickness of the undoped layer. However, as the undoped layer thickness decreases, the cell efficiency drops to unacceptable values (below 2%). So, there is an optimum undoped layer thickness that satisfies both maximum transparency and efficiency at the same time. In the following analyses, we define the wavelength range of 380-580 nm as the range for which the cells should be transparent and we denote this range as T-range. Photons with the wavelength range of 580-800 nm are considered as the one should be reflected back and ultimately absorbed in the cells. This range is called R-range.

Figure 5.8 depicts the transmittance spectra of 100, 200, and 300 nm thick a-Si:H films deposited on glass substrates. For these layers, the optimum i-layer deposition parameters are used. As this figure shows, the maximum transparencies in the T-range are 28%, 25%, and 11.2% for 100, 200, and 300 nm thick i-layers, respectively. As the wavelength increases, these absorber layers become more transparent with the average transparencies of 79%, 50%, and 43% in the red part of the spectrum (620-750

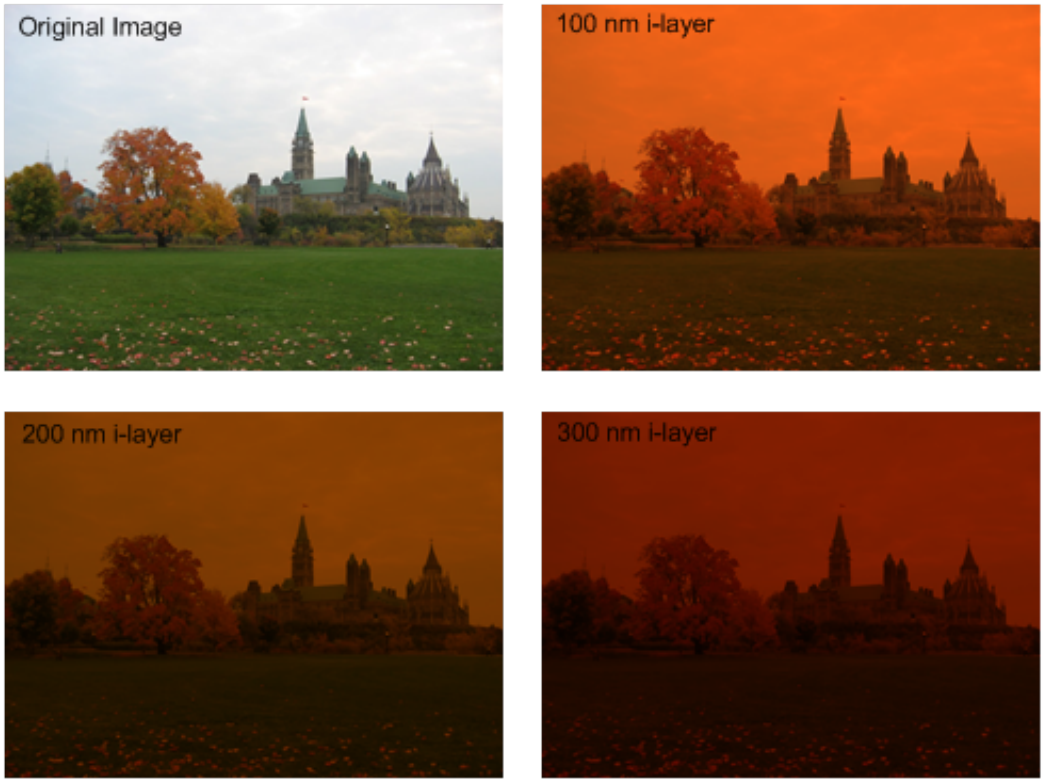

Figure 5.9: Calculated color filtering effect of 100, 200 and, 300 nm thick amorphous silicon films on a sample image.

nm). To have a better understanding of the effect of the undoped layer thickness on the transparency of the fabricated cells, we have calculated the color filtering effect of these films using a MATLAB code. In this simulation, the measured transmission spectra is converted to RGB values using a color-matching function based on 1964 CIE 10-degree observer [69]. These converted RGB values are then used as color filters for a sample picture. Figure 5.9 shows the results of this simulation on a sample picture.

To investigate the effect of the absorber layer thickness on the output characteristic of the semi-transparent solar cells, single junction devices with 100, 200, and 300 nm thick i-layers are fabricated on Asahi ITO-coated glass substrates. The structure of these solar cells consists of substrate / nc-Si p-layer (25 nm) / a-Si i-layer / nc-Si n-layer (30 nm) / ZnO:Al (600 nm). Doped and undoped layers are deposited using

the previously optimized processes parameters achieved in Chapter 3.

Figure 5.10 shows the transmission spectra of these solar cells measured from the film side. While the T-range transmission spectra of the fabricated cells are almost identical to that of the single i-layers (see Figure 5.8), the R-range transparencies decreases to the average values of 42%, 32%, and 27% for these solar cells. The lower R-range average transparencies in this case are attributed to the better long-wavelength photon trapping of these cells due to the optimum surface roughness of the Asahi ITO-coated glass substrates. The conversion efficiencies and T-range cumulative transmittance of the semi-transparent cells with 100, 200, and 300 nm thick absorber layers are presented in the Figure 5.11. This figure clearly shows the trade-off between the visible-range transparency and the efficiency of the semi-transparent solar cells. As the thickness of the absorber layer decreases from 300 nm to 100 nm, the efficiency of the fabricated cells drops by $\sim$28%. The EQE measurements of these solar cells (Figure 5.12), demonstrate that, the poor absorption of photons with the wavelengths above 450 nm accounts for the low efficiency values of thin i-layer devices. Our measurements reveals an optimum i-layer thickness of around 200 nm and the conversion efficiency of $\sim$4.5% for the fabricated solar cells. X. Zhang et. al. [67] reported the same optimum i-layer thickness and a conversion efficiency of 3% for the semi-transparent cells fabricated on a large area, series connected plastic panel.

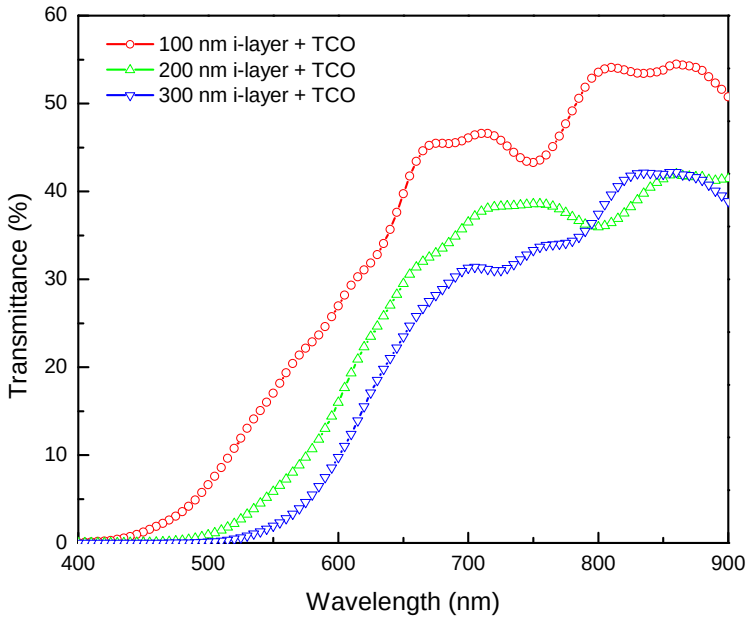

Figure 5.10: Transmittance spectra of the semi-transparent cells with 100, 200, and 300 nm thick absorber layers.

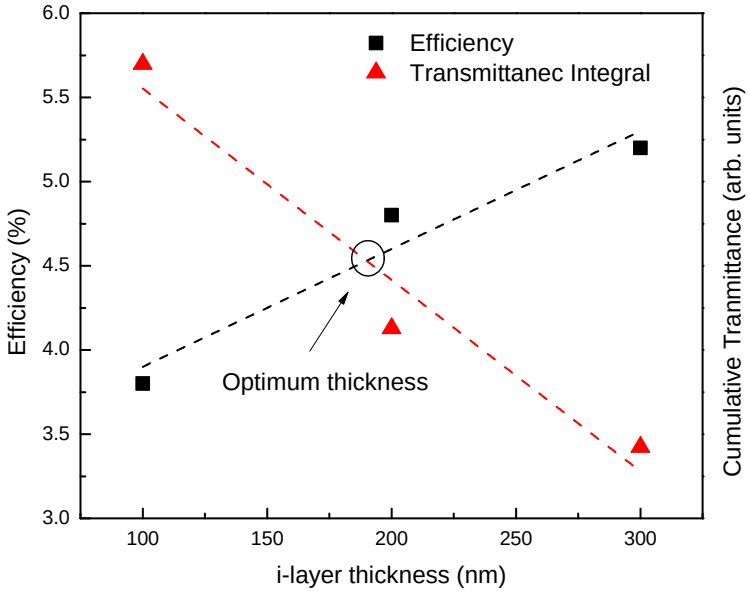

Figure 5.11: Conversion efficiencies and T-range cumulative transmittance of the semi-transparent cells with 100, 200, and 300 nm thick absorber layers.

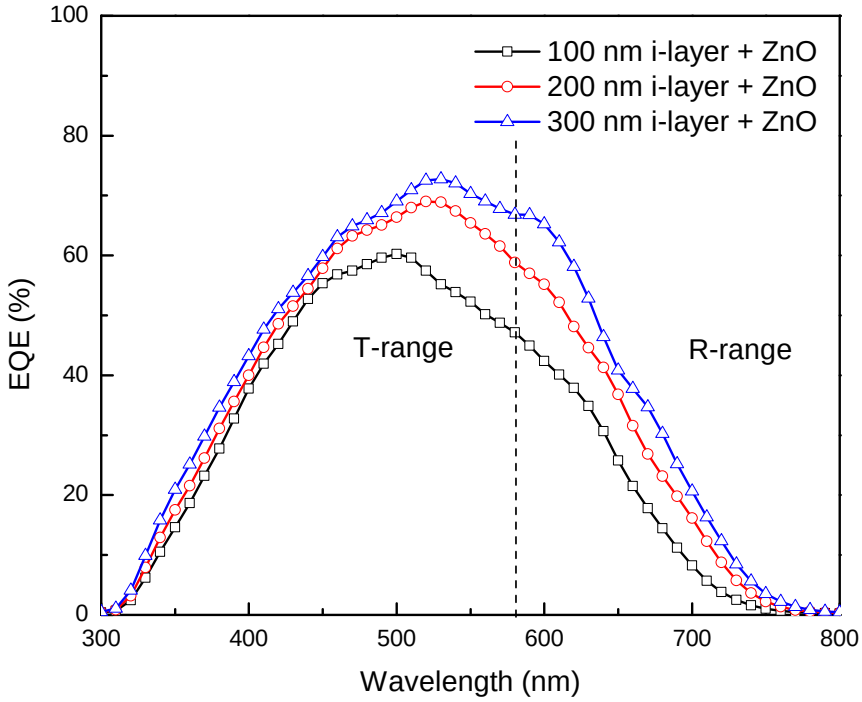

Figure 5.12: External quantum efficiency spectra of the semi-transparent cells with 100, 200, and 300 nm thick absorber layers.

5.3.2 Semi-transparent solar cells with DBR back structures

In this section, we propose using DBR back structures to improve the efficiency of semi-transparent solar cells. We observe that the lower efficiencies acquired for devices with thin i-layers are mostly due to the poor absorption of long-wavelength photons in these solar cells. DBR structures can be appropriately designed to selectively reflect these photons back into the absorber layer. The most important design criteria for these DBR structures are: the selective high reflection and the low T-range absorption. To begin with, we evaluate these criteria for the DBR structure introduced in the section 5.2. This four-period DBR structure with the high reflectance of 98% for the wavelength range of 600-800 nm satisfies the first condition. Regarding the second condition, Figure 5.13 demonstrates the T-range transmission spectra of the same DBR structures with two-, four-, and six-period a-Si/a-SiN film stacks measured from the film side of the samples. As this figure shows, the maximum average transmission in the T-range of the spectrum belongs to the two-period DBR structure

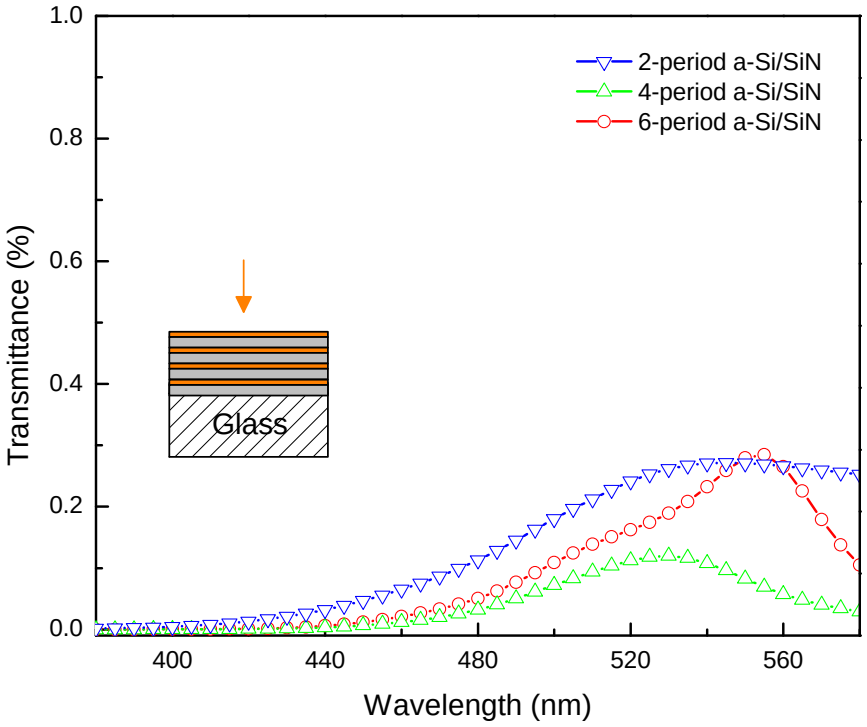

Figure 5.13: T-range transmittance spectra of two-, four-, and six-period a-Si/a-SiN DBR structures.

and it is nearly less than 20%. So, this DBR structure is not suitable as the back reflector in the semi-transparent solar cells because it blocks more than 80% of the incoming light which we would like it to pass trough the solar cell. In a-Si/a-SiN DBR structures, amorphous silicon nitride is a dielectric film with a band gap around 5.3 eV and it is totally transparent for the T-range wavelength range. Consequently, it is the amorphous silicon film in the DBR structure that is responsible for the T-range absorption of the incoming light. In order to increase the bandgap of the a-Si film, we propose adding atomic Nitrogen to this material. In this case, the DBR structure consists of a-SiN film stacks with alternating nitrogen content. Figure 5.14 shows the absorption coefficients of a-Si and a-SiN films with different nitrogen content for the wavelength range of 300-750 nm. Considering the DBR central wavelength of 700 nm, adding Amonia to the deposition process of a-Si, can significantly decreases the material absorption coefficient. While adding atomic nitrogen to the a-Si film

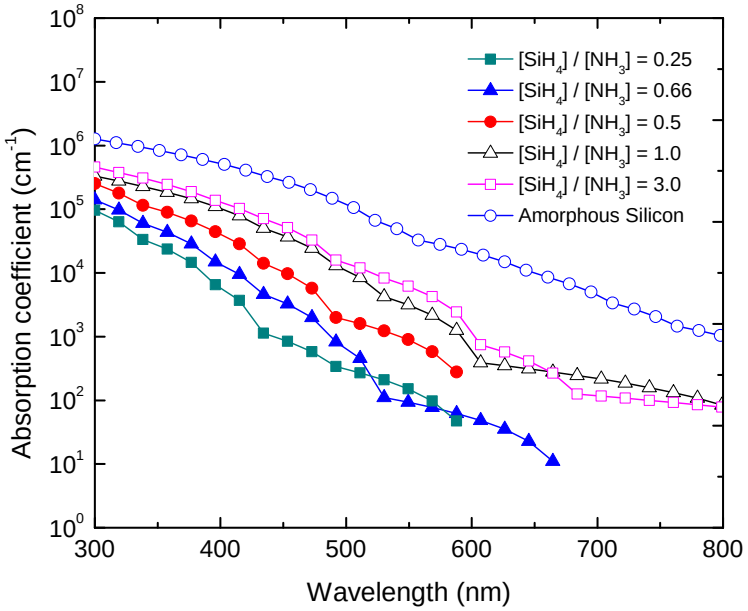

Figure 5.14: Absorption coefficients of a-Si and a-SiN films versus wavelength for different Silane-to-Amonia gas ratios.

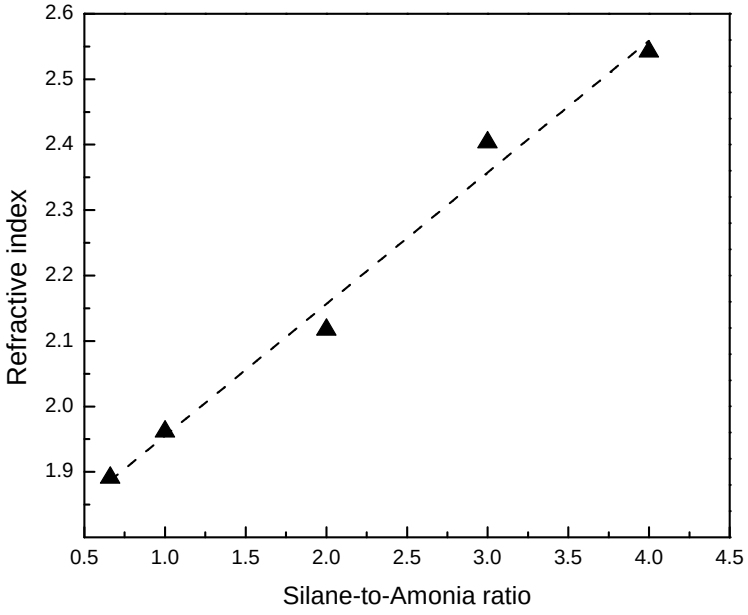

Figure 5.15: Refractive indices of a-SiN films at the wavelength of 700 nm for different Silane-to-Amonia gas ratios

enhances the transparency, it also affects the refractive index of the deposited films. Figure 5.15 shows the refractive indices of a-SiN films at the wavelength of 700 nm for different Silane-to-Amonia flow rate ratios. By varying the nitrogen content of a-SiN films, their refractive indices at this wavelength can be tuned in the range of 1.9-2.55. In DBR structures, in order to achieve a selective high reflection, the contrast between the refractive indices of the two base materials should be as high as possible. DBR reflectance simulations, assuming the low refractive index (n_L) of 1.7 (a-SiN with low nitrogen content) and high refractive indices (n_H) of 2, 2.5, and 3 (a-SiN with high nitrogen content) for a 4-period DBR structure are shown in Figure 5.16. As this figure shows, the contrast between the two base materials of the DBR structure strongly affects both the height and the width of the characteristic form of the reflectance spectra. These simulations suggest the minimum n_H of 2.5 in order to obtain $\geq$ 80% DBR reflectance for the wavelength range of 600-800 nm. Referring to the Figures 5.14 and 5.15, Silane-to-Amonia ratio of 4 with one order of magnitude lower absorption coefficient (at λ=700 nm) compared to the a-Si film can provide the optimum high refractive index material for our DBR structures.

Employing this optimum high refractive index material, a four-period DBR structure is deposited on a glass substrate and its transmission spectra is measured and compared to that of two-, four-, and six-period a-Si / a-SiN DBR structures. Figure 5.17 presents the results of these measurements in the T-range of the spectrum. The proposed four-period DBR structure improves the T-range transparency even compared to a two-period a-Si /a-SiN DBR structure by more than 45%. To examine the effect of using this optimum DBR structure on the output characteristics of semi-transparent devices, a single junction p-i-n solar cell with the proposed DBR back structure is fabricated on a glass substrate and its optical and electrical characteristics compared to those of a device with no back reflector. Figures 5.18 and 5.19 illustrate the transmission spectra and the EQE measurements of these two semi-transparent solar cells. While using DBR back structure decreases the T-range transparency by $\sim$45%, it improves the absorption efficiency of photons with the wavelengths above 600 nm by 5%.

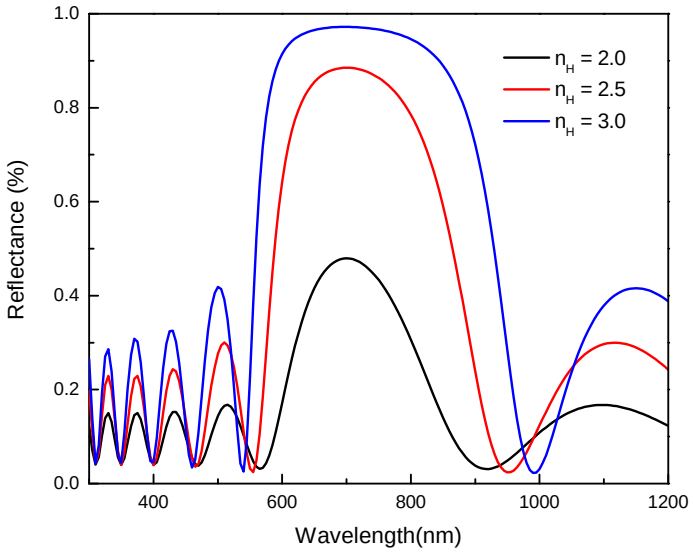

Figure 5.16: Simulation of reflectance spectra of 4-period DBR structures with the low refractive index of 1.7 and high refractive indices of 2, 2.5, and 3.

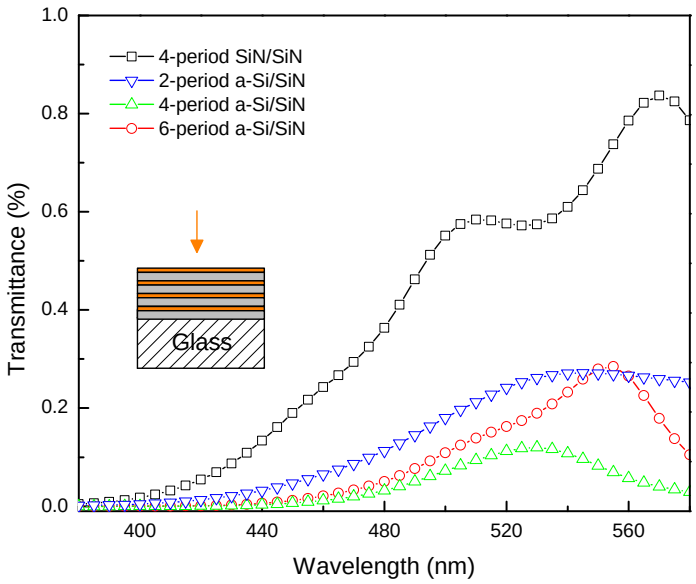

Figure 5.17: T-range transmittance spectra of a two-period a-SiN / a-SiN and two-, four-, and six-period a-Si / a-SiN DBR structures measured from the film side of the samples.

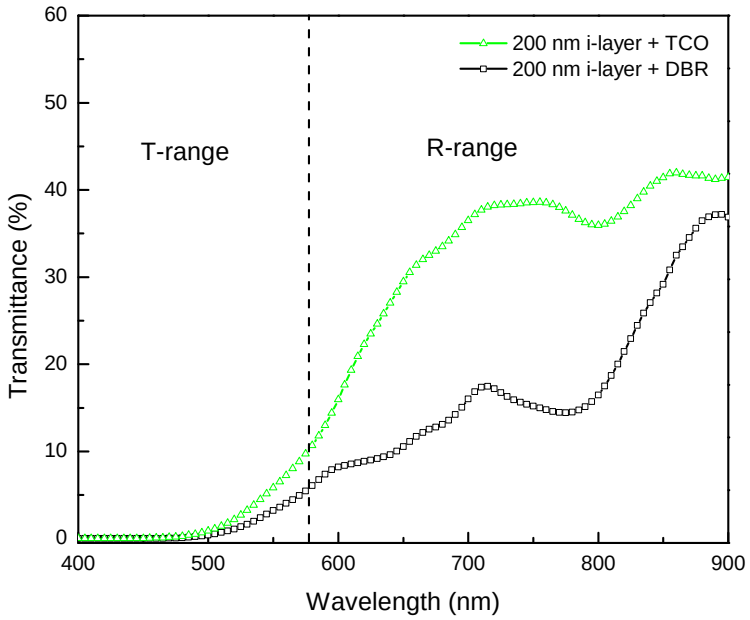

Figure 5.18: Transmittance spectra of the semi-transparent cells with 100, 200, and 300 nm thick absorber layers.

As a result of this EQE enhancement in the cell with DBR structure, the short-circuit current density increases by 5% from 10.5 mA/cm^2 to 11.02 mA/cm^2 compared to that with no back structure.

5.4 Summary

In this chapter we study using distributed Bragg reflectors as the highly reflective back structures in thin film amorphous silicon solar cells. Our measurements showed that replacing conventional Al back electrodes with DBR structures improves the short-circuit current density of the cells fabricated on Asahi ITO-coated glasses by 10%; resulting in the same improvement in the conversion efficiency. However, as evident in this case, texturing front TCO layer is essential to achieve multiple photon reflections in the red and near-IR part of the spectrum. In addition, we propose using DBR structures to enhance the efficiency of semi-transparent solar cells. In this part, a semi-transparent a-Si solar cell is optimized in terms of the conversion efficiency

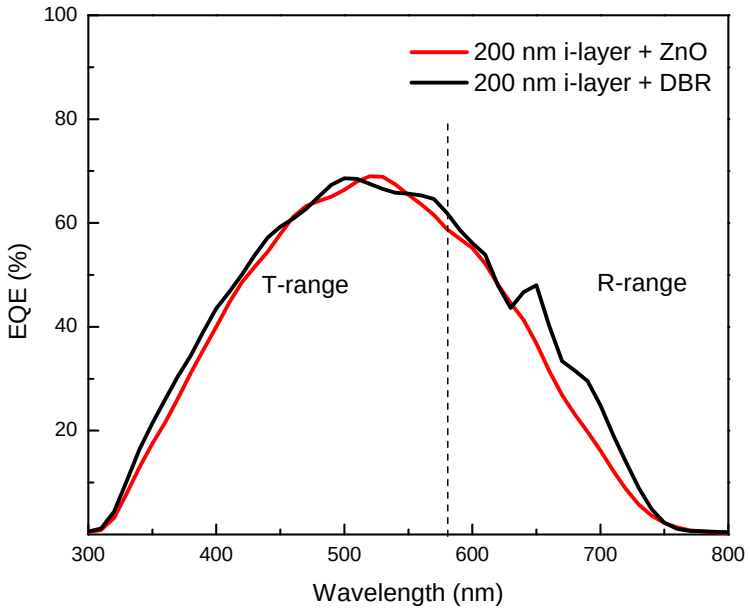

Figure 5.19: Transmittance spectra of the semi-transparent cells with 100, 200, and 300 nm thick absorber layers.

and optical transparency. The i-layer thickness and the efficiency of the optimum solar cell are 200 nm and 4.5%, respectively. To improve the efficiency of this solar cell, we have designed a specific DBR structure based on two different a-SiN films with low T-range absorption and high refractive index contrast. By Employing this DBR structure the efficiency of the semi-transparent solar cell is increased by 5% from 4.5% to 4.72%.

Chapter 6

Conclusion

The goal of this research is to develop high efficiency thin film silicon devices on transparent plastic substrates. In this research we assume two important constraints: all the film depositions should be compatible with low processing temperature of the plastic substrates, and we only consider amorphous silicon based solar cells in the p-i-n configuration. As a result, the accessible range of deposition temperature is between 135 and 180 °C which is not ideal for the deposition of high quality amorphous silicon materials. It is important to mention that there was not any previous experience available in the G2N lab regarding the fabrication and development of these thin film solar cells. In the following section, we summarize the major results and contributions provided by this research and show that, we have achieved efficiencies well within and in some cases above the range of the state-of-the-art devices with similar fabrication constraints.

6.1 Achievements of this research

Optimization of individual thin films:

- Low temperature, highly conductive ($\sim$ 0.07 S/cm) B-doped nanocrystalline silicon (nc-Si:H) thin films were grown on glass substrates by plasma-enhanced

chemical vapor deposition using trimethylboron (TMB) as a doping gas. The film crystallinity and conductivity were found to be tailored by controlling the TMB-to-SiH_4 flow ratio.

- The optical constants (refractive index and extinction coefficient) of doped and undoped nc-Si:H 20-50 nm thick films were determined and analyzed.

- The same nanocrystalline film growth on ZnO:Al-coated glass substrates was achieved by implementing a seed-layer.

- Low temperature, highly conductive ($\sim$ 0.5 S/cm) P-doped nanocrystalline silicon (nc-Si:H) thin films were grown on glass substrates by plasma-enhanced chemical vapor deposition using Phosphine (PH_3) as a doping gas. The film crystallinity and conductivity were found to be tailored by controlling the PH_3-to-SiH_4 flow ratio.

- Undoped protocrystalline silicon (pc-Si:H) films were grown and optimized on glass substrates by plasma-enhanced chemical vapor deposition. The optimized protocrystalline film has a photosensitivity ($\sigma_{ph}/\sigma_{dark}$) of 1.5×10^6.

Layer integration and device fabrication:

- Thin film amorphous silicon solar cells were fabricated and optimized on glass substrates by varying the hydrogen dilution ratio of the absorber layer. The optimum device was realized with an absorber layer right at the transition from amorphous to microcrystalline silicon. At this transition the open-circuit voltage of the device is experienced a sudden drop due to the band gap reduction of the absorber layer.

- To improve the performance of the fabricated solar cells, amorphous silicon carbide buffer layers were introduced between the nc-Si p-doped and the undoped pc-Si absorber layers.

- By employing the p+ nc-Si:H as a window layer combined with a p' a-SiC buffer layer and the optimum pc-Si:H i-layer, a-Si:H-based p-p'-i-n solar cells were fabricated and characterized both on glass and plastic substrates. Table 6.1 reports that output characteristics of these devices. Comparing these values with those presented in Table 1.2 reveals the superior characteristics of the fabricated devices.

  Table 6.1: AM1.5 output parameters of the optimum devices on glass and PEN substrate.

Substrate	V_{oc} (V)	I_{sc} (mA)	FF (%)	η(%)
Glass	0.8875	12.469	63.26	7.00
PEN	0.879	11.325	61.00	6.07

Implementation of light management:

- Distributed Bragg reflectors were proposed as the highly reflective back structures for a-Si based solar cells on glass and plastic substrates. We showed that by replacing the conventional Al back reflector with a DBR structure, short-circuit current density of the cells fabricated on Asahi U-type glasses improves by 10% ; resulting in the same improvement in the conversion efficiency. For the cells fabricated on PEN, the absorption enhancement was lower ($\sim$5%) as a result of the front ZnO smoothness.

- Semi-transparent solar cells with TCO/p-i-n/TCO structures were optimized in terms of the cell efficiency and transparency on glass substrates. The optimum i-layer thickness was achieved to be around 200 nm. The semi-transparent cell with this i-layer results in a conversion efficiency of 4.5%.

- To improve the efficiency of these semi-transparent devices, DBR structures were designed and optimized in terms of visible range transparency and selective

range reflectivity. Using these optimized DBR structures as the selective back reflectors, the efficiency of the semi-transparent solar cells was enhanced by 5%.

6.2 Recommendations for the Future Work

Although the optimization of different layers of low temperature a-Si based solar cells has been addressed in this research, there are opportunities for the further work.

In the p-doped layer optimization, we investigated the nanocrystalline structure of the deposited films on smooth Al-doped ZnO layers. As it explained before, the front ZnO layer is usually textured to scatter the incoming light. We suggest the same investigation for the p-layers deposited on the textured Al-doped ZnO layers. It is likely that the surface roughness can effect the nucleation process of the nanocrystalline p-doped layers.

While flexible substrates offer many opportunities, it brings some new issues too. One of the most important issues is the stability of the output characteristics of flexible devices under different mechanical and thermal stress conditions. To address this issue, the output characteristics of the fabricated devices on PEN substrates can be studied and modeled under different stress/strain conditions. This investigation becomes more important when we consider the Roll-to-Roll fabrication processes for the flexible solar cells. In this fabrication process, ultimately, the fabricated solar cells are stored in a big cassette roles. So, one should carefully consider mechanical properties of the deposited films to prevent the delamination of the deposited solar cell layers.

To better capture the incoming light in the absorber layer, this light is usually scattered at the rough interfaces of the thin film solar cells. In p-i-n configuration, it is the front TCO layer that introduces these rough interfaces into the solar cell. In the case of plastic solar cells, this roughness can be created by nano-texturing the substrate either by dry etching or hot embossing processes. This research is currently in progress.

Finally, it would be worthwhile to investigate the same optimization process for microcrystalline-based solar cells. The optical properties of this material are quite different from those of amorphous silicon and it can be used in tandem micromorph solar cells with improved efficiency properties. A micromorph solar cell consists of a stack of top a-Si cell and bottom μc-Si cell. This combination is shown to posses bandgaps that are very close to the optimum combination of bandgaps for the sun spectrum.

Bibliography

[1] J. Poortmans and V. Arkhipov. *Thin Film Solar Cells*. John Wiley & Sons, 2006. 1, 11, 15, 17, 19, 34, 35, 36, 38, 57, 58, 68, 78

[2] W.G.J.H.M. van Sark, G.W. Brandsen, M. Fleuster, and M.P. Hekkert. Analysis of the silicon market: Will thin films profit? *Energy Policy*, 35(6):3121–3125, June 2007. xi, 1, 2, 3

[3] P. Mints. PV – the story so far: How is the PV industry progressing in its bid to be considered mainstream? *Refocus*, 7(6):32, 34–36, December 2006. 1

[4] J. R. Sheats. Roll–to–Roll manufacturing of thin film electronics. *Proceedings of SPIE*, 4688:240–248, July 2002. 2

[5] V. Cannella et.al. Flexible stainless steel substrates for displays. http://people.ccmr.cornell.edu/∼cober/mse542/page2/files/Barriers.pdf, 2007. MSE 542 Lecture notes-Cornell University, Accessed in March 2008. x, 4, 5, 27

[6] J. Bailat, V. Terrazzoni-Daudrix, J. Guillet, F. Freitas, X. Niquille, A. Shah, C. Ballif, T. Scharf, R.Morf, A. Hansen, D. Fischer, Y. Ziegler, and A. Closset. Recent development of solar cells on low–cost plastic substrates. *Proceedings of the 20th EU Photovoltaic Solar Energy Conference*, pages 1529–1532, June 2005. 4, 18, 19

[7] http://www.uni solar.com/. Accessed in March 2008. 5, 6

[8] M. B. Schubert and J. H. Werner. Flexible solar cells for clothing. *Materials Today,*, 9(6):42–50, 2006. 5, 19, 20

[9] www.fujiele.co.jp/eng/index.html. Accessed in March 2008. 6

[10] www.flexcell.com. Accessed in March 2008. 6, 19, 36

[11] www.akzonobel.com. Accessed in March 2008. 6

[12] www.powerfilmsolar.com. Accessed in March 2008. 6

[13] www.sanyo.co.jp. Accessed in March 2008. 6

[14] J Muller. TCO and light trapping in silicon thin film solar cells. *Solar Energy*, 77(6):917–930, December 2004. 15

[15] H. Okaniwa, K. Nakatani, M. Yano, M. Asano, and K. Suzuki. Preparation and properties of a–Si:H solar cells on organic polymer film substrate. *Japanese Journal of Applied Physics*, 21(Supplement 21-2):239–244, 1982. 16, 18

[16] M. Yano, K. Suzuki, K. Nakatani, and H. Okaniwa. Roll–To–Roll preparation of a hydrogenated amorphous silicon solar cell on a polymer film substrate. *Thin Solid Films*, 146(1):75–81, January 1987. 17, 18

[17] H. Mase, M. Kondob, and A. Matsuda. Microcrystalline silicon solar cells fabricated on polymer substrate. *Solar Energy Materials & Solar Cells*, 74(1-4):547552, October 2002. 17, 18

[18] T. Takeda, M. Kondo, and A. Matsuda. Thin film silicon solar cells on liquid crystal polymer substrate. *Proceeding of the 3rd World Conference on Photovoltaic Energy Conversion*, pages 1580–1583, May 2003. 17, 18

[19] Y. Kishi, H. Inoue, K. Murata, S. Kouzuma, M. Morizane, H. Shibuya, H. Nishiwaki, and Y. Kuwano. A new type of ultralight flexible a–Si solar cell. *Japanese Journal of Applied Physics*, 31(1):12–17, January 1992. 18

[20] P. Pernet, R. Felder, M. Goetz, H. Keppner, D. Fischer, and A. Shah. Optimization of amorphous silicon solar cells on polymer film substrates. *Proceedings of the 14th EC Photovoltaic Solar Energy Conference*, pages 2339–2342, July 1997. 18

[21] P. Pernet. *Dveloppement de Cellules Solaires en Silicium Amorphe de Type "n–i–p" Sur Substrats Souples*. Phd thesis, Universit de Neuchtel, 2000. 18, 25

[22] A. Vijh, X. Yangb, W. Dub, and X. Dengb. Triple–junction amorphous silicon–based flexible solar minimodule with integrated interconnects. *Solar Energy Materials & Solar Cells*, 90(16):26572664, October 2006. 18, 19

[23] Y. Ishikawa and M. B. Schubert. Flexible protocrystalline silicon solar cells with amorphous buffer layer. *Japanese Journal of Applied Physics*, 45(9A):6812–6822, September 2006. 18, 19, 32, 58, 70

[24] A. Lambertz, C. Roβ, H. Siekmann, G. S., and F. Finger. Thin film silicon solar cells on transparent and flexible plastic films. *Proceeding of the 21st European Photovoltaic Solar Energy Conference*, pages 1771–1774, 2006. 18

[25] G. Dennlera, S. Bereznevb, D. Fichouc, K. Holld, D. Ilicd, R. Koeppea, M. Krebsd, A. Labourete, C. Lungenschmieda, A. Marchenkoc, D. Meissnera, E. Mellikovb, J. Mote, A. Meyerf, T. Meyerf, H. Neugebauera, A. pikb, N.S. Sariciftcia, S. Taillemitec, and T. Whrled. A self–rechargeable and flexible polymer solar battery. *Solar Energy*, 81(8):947–957, August 2007. 20

[26] K. R. Sarma, C.Chanley, S. Dodd, J. Roush, J. Schmidt, G. Srdanov, M. Stevenson, R. Wessel, J. Innocenzo, G. Yu, M. O'Regan, W. A. MacDonald, and R. Eveson. Active Matrix OLED using 150 °C a-Si TFT backplane built on flexible plastic substrate. *Proceedings of SPIE*, 5080(24):180–191, September 2003. 25

[27] P. D. Kondo et al. *Multilayer Optical Bodies*. US Patent, December 2002. US 6,498,683 B2. x, 27

[28] A.N. Banerjee, C.K. Ghosh, K.K. Chattopadhyay, H. Minoura, A. K. Sarkar, A. Akiba, A. Kamiya, and T. Endo. Low–temperature deposition of ZnO thin films on PET and glass substrates by dc-sputtering technique. *Thin Solid Films*, 496(1):112–116, February 2006. 29

[29] Menno N. van den Donker. *Plasma Deposition of Microcrystalline Silicon Solar Cells: Looking Beyond the Glass*. PhD thesis, Julich Research Center, 2006. xii, 30

[30] R.W. Collins and A.S. Ferlauto. Advances in plasma–enhanced chemical vapor deposition of silicon films at low temperatures. *Current Opinion in Solid State & Material Science*, 6(5):425–437, September 2002. xii, 31, 32

[31] J. Yang and S. Guha. Amorphous silicon alloy materials and solar cells near the threshold of microcrystallinity. *Proceedings of Material Research Symposium*, 557:239–250, 1999. 31

[32] M. Kondo and A. Matsuda. *Low–Temperature Fabrication of Nanocrystalline–Silicon Solar Cells*, chapter 8. Springer Series in Photonics. Springer Berlin Heidelberg, 2004. xii, 32, 33

[33] E.D. Palik. *Handbook of Optical Constants of Solids*. Academic Press, first edition, 1985. 34, 78

[34] L. Zeng, P. Bermel, Y. Yi, B. A. Alamariu, K. A. Broderick, J. Liu, C. Hong, X. Duan, J. Joannopoulos, and L. C. Kimerling. Demonstration of enhanced absorption in thin film Si solar cells with textured photonic crystal back reflector. *Applied Physics Letters*, 93(22), 2008. 34, 78

[35] Benjamin Curtin, Rana Biswas, and Vikram Dalal. Photonic crystal based back reflectors for light management and enhanced absorption in amorphous silicon solar cells. *Applied Physics Letters*, 95(23), 2009. 34, 78

[36] Paul G. O'Brien, Nazir P. Kherani, Alongkarn Chutinan, Geoffrey A. Ozin, Sajeev John, and Stefan Zukotynski. Silicon Photovoltaics Using Conducting Photonic Crystal Back-Reflectors. *Adv. Mater.*, 20(8):1577–1582, 2008. 34, 78

[37] J. Krc, M. Zeman, S. L. Luxembourg, and M. Topic. Modulated photonic-crystal structures as broadband back reflectors in thin-film solar cells. *Applied Physics Letters*, 94(15), 2009. 34, 78

[38] Vivian E. Ferry, Marc A. Verschuuren, Hongbo B. T. Li, Ruud E. I. Schropp, Harry A. Atwater, and Albert Polman. Improved red-response in thin film a-Si:H solar cells with soft-imprinted plasmonic back reflectors. *Applied Physics Letters*, 95(18), 2009. 34, 78

[39] J. P. M. Schmitt. Amorphous silicon deposition: Industrial and technical challenges. *Thin Solid Films*, 174:193–202, July 1989. 36

[40] H. Mashima, H. Yamakoshi, K. Kawamura, Y. Takeuchi, M. Noda, Y. Yonekura, H. Takatsuka, S. Uchino, and Y. Kawai. Large area VHF plasma production using a ladder–shaped electrode. *Thin Solid Films*, 506-507:512–516, May 2006. 36

[41] S. A. Campbell. *The Science and Engineering of Microelectronic Fabrication*. Oxford University Press, second edition, 2001. 38

[42] C. Droz. *Thin Film Microcrystalline Silicon Layers and Solar Cells: Microstructure and Electrical Performances*. PhD thesis, University of Neuchatel, November 2003. 40

[43] R Swanepoel. Determination of the thickness and optical constants of amorphous silicon. *Journal of Physics E: Scientific Instruments*, 16(12):1214–1222, December 1983. 40, 53

[44] E Birgin. Estimation of the Optical Constants and the Thickness of Thin Films Using Unconstrained Optimization. *Journal of Computational Physics*, 151(2):862–880, May 1999. 41, 80

[45] Mohammad R. Esmaeili Rad, Flora Li, Andrei Sazonov, and Arokia Nathan. Stability of nanocrystalline silicon bottom-gate thin film transistors with silicon nitride gate dielectric. *Journal of Applied Physics*, 102(6), 2007. 48

[46] R Saleh. Raman spectroscopy of B-doped microcrystalline silicon films. *Thin Solid Films*, 427(1-2):266–269, March 2003. 51

[47] P Kumar, M Kupich, D Grunsky, and B Schroeder. Microcrystalline B-doped window layers prepared near amorphous to microcrystalline transition by HWCVD and its application in amorphous silicon solar cells. *Thin Solid Films*, 501(1-2):260–263, April 2006. 51

[48] V. Golubev, L. Morozova, A. Pevtsov, and N. Feoktistov. Conductivity of thin nanocrystalline silicon films. *Semiconductors*, 33:66–68, 1999. 10.1134/1.1187635. 51

[49] A Gordijn, J Loffler, W Arnoldbik, F Tichelaar, J Rath, and R Schropp. Thickness determination of thin (20nm) microcrystalline silicon layers. *Solar Energy Materials and Solar Cells*, 87(1-4):445–455, May 2005. 53

[50] Z Hu, X Liao, H Diao, Y Cai, S Zhang, E Fortunato, and R Martins. Hydrogenated p-type nanocrystalline silicon in amorphous silicon solar cells. *Journal of Non-Crystalline Solids*, 352(9-20):1900–1903, June 2006. 53

[51] R T Phillips. A numerical method for determining the complex refractive index from reflectance and transmittance of supported thin films. *Journal of Physics D: Applied Physics*, 16(4), April 1983. 54

[52] S. Halindintwali, D. Knoesen, T. Muller, D. Adams, N. Tile, C. Theron, and R. Schropp. Optical characterisation of a-si:h and nc-si:h thin films using the transmission spectrum alone. *Journal of Materials Science: Materials in Electronics*, 18:225–229, 2007. 10.1007/s10854-007-9194-8. 54

[53] A. H. M. Smets, W. M. M. Kessels, and M. C. M. van de Sanden. Vacancies and voids in hydrogenated amorphous silicon. *Applied Physics Letters*, 82(10):1547–1549, 2003. 56

[54] J Mullerova, Sutta P, G Vanelzakker, M Zeman, and M Mikula. Microstructure of hydrogenated silicon thin films prepared from silane diluted with hydrogen. *Applied Surface Science*, 254(12):3690–3695, April 2008. 56

[55] J. Müllerová, L. Prušáková, M. Netrvalová, V. Vavruková, and P. Šutta. A study of optical absorption in amorphous hydrogenated silicon thin films of varied thickness. *Applied Surface Science*, 256(18):5667–5671, July 2010. 56

[56] Hyun Jung Lee. *Top-Gate Nanocrystalline Silicon Thin Film Transistors*. Phd thesis, University of Waterloo, 2008. 57

[57] S Hamma. Low-temperature growth of thick intrinsic and ultrathin phosphorous or boron-doped microcrystalline silicon films: Optimum crystalline fractions for solar cell applications. *Solar Energy Materials and Solar Cells*, 69(3):217–239, October 2001. 67

[58] T Toyama and H Okamoto. Structural and electrical studies of plasma-deposited polycrystalline silicon thin-films for photovoltaic application. *Solar Energy*, 80(6):658–666, June 2006. 68, 76

[59] O Vetterl. Preparation of microcrystalline silicon seed-layers with defined structural properties. *Thin Solid Films*, 427(1-2):46–50, March 2003. 72

[60] Y. Vygranenko, A. Sazonov, G. Heiler, T. Tredwell, M. Vieira, and A. Nathan. Blue-enhanced thin-film photodiode for dual-screen x-ray imaging. *Applied Physics Letters*, 95(26), 2009. 73

[61] J. K. Rath and R. E. I. Schropp. Incorporation of p-type microcrystalline silicon films in amorphous silicon based solar cells in a superstrate structure. *Solar Energy Materials and Solar Cells*, 53(1-2):189 – 203, 1998. 73

[62] N. Palit and P. Chatterjee. Computer analysis of a-Si:H p-i-n solar cells with a hydrogenated microcrystalline silicon p layer. *Journal of Applied Physics*, 86(12):6879–6889, 1999. 73

[63] S Guha. Thin film silicon solar cells grown near the edge of amorphous to microcrystalline transition. *Solar Energy*, 77(6):887–892, December 2004. 76

[64] M. Dubey F. Meillaud X. Niquille J. Guillet A. Shah A. Poruba L. Mullerova J. Springer J. Bailat, E. Vallat-Sauvain and M. Vanecek. Quality of i-layer investigated within the complete solar cells by absorption spectroscopy. *Proceedings of 19th EU Photovoltaic Solar Energy Conference*, (1541-1544), 2004. 76

[65] R. Paschotta. *Encyclopedia of Laser Physics and Technology*. WILEY-VCH, 2008. 79

[66] M Biancardo, K Taira, N Kogo, H Kikuchi, N Kumagai, N Kuratani, I Inagawa, S Imoto, and J Nakata. Characterization of microspherical semi-transparent solar cells and modules. *Solar Energy*, 81(6):711–716, June 2007. 79

[67] Xiaolan Zhang, Marc Saemann, Jian Hu, Augusto Kunrath, Agnes Berger, and Arun Madan. Semi-Transparent Solar Cells and Modules on Inexpensive Plastic Substrates. pages 1517–1520, Waikoloa, HI, May 2006. 79, 80, 89

[68] J. Huang, G. Li, and Y. Yang. A Semi-transparent Plastic Solar Cell Fabricated by a Lamination Process. *Adv. Mater.*, 20(3):415–419, 2008. 79

[69] http://cie.co.at/. Accessed in February 2011. 80, 88